Copyright
by
Artem Dudarev
2005

The Dissertation Committee for Artem Dudarev
certifies that this is the approved version of the following dissertation:

Dynamics of ultracold atoms in optical potentials

Committee:

Qian Niu, Supervisor

Mark G. Raizen, Supervisor

Manfred Fink

Greg O. Sitz

Dmitrii E. Makarov

Dynamics of ultracold atoms in optical potentials

by

Artem Dudarev, B.S.

DISSERTATION

Presented to the Faculty of the Graduate School of

The University of Texas at Austin

in Partial Fulfillment

of the Requirements

for the Degree of

DOCTOR OF PHILOSOPHY

THE UNIVERSITY OF TEXAS AT AUSTIN

May 2005

To my parents

Acknowledgments

First of all, I would like to thank my supervisors Prof. Mark Raizen and Prof. Qian Niu for their guidance and support. A large fraction of the research described in this dissertation is the result of a fruitful collaboration with Roberto Diener. The thesis of Ganesh Sundaram was indispensable to understand the effects of geometrical phase on wave packet dynamics. It was also a great pleasure to collaborate with Biao Wu, Iacopo Carusotto, Prof. Nathaniel Fisch, and Prof. Michael Marder. The codes written by Nadav Katz were very helpful to start learning about numerical simulation of quantum systems. I had a unique opportunity to learn about experimental physics working closely with talented experimentalists Martin Fischer, Valery Milner, Braulio Gutierrez-Medina and Kevin Henderson. Several ideas discussed in the last chapter were born in the discussions with another team of talented experimentalists: Florian Schreck, Todd Meyrath, Chih-sung Chuu, and Jay Hanssen.

I would like also to thank the following people for affecting my points of view on physics and life: Chuanwei Zhang, Hrishikesh Kelkar, Michael Goegler, Katrin Schmitt, Windell Oskay, Daniel Steck, Artur Widera, Robert Morgan, Kirk W. Madison, Patrick Bloom, Wes Campbell, Joshua Elliott, Gregory Henry, Julie Horn, Adrienne Lipoma, Samantha Moore, Ping Zhang, Junren

Shi, Di Xiao, Dimi Clucer.

Norma Kotz, Carol Noriega, Olga Vera, Rosamarie Tovar and Elena Simmons were very helpful with administrative issues in UT.

Finally, I would like to thank Todd Meyrath, Samantha Moore, Kevin Henderson, and Michael Marder for giving me many comments on style, languge and physics of the articles on which the dissertation is based. Todd Meyrath has also provided numerous comments about the dissertation.

Dynamics of ultracold atoms in optical potentials

Publication No. _____

Artem Dudarev, Ph.D.
The University of Texas at Austin, 2005

Supervisors: Qian Niu
Mark G. Raizen

In this dissertation, we discuss the manipulation of ultracold atoms with optical fields. We show how a one-way barrier for ground state atoms may be constructed. Its use for phase space compression is analyzed. Using several ideas from solid-state physics, we reveal a number of novel phenomena in quantum transport of ultracold atoms in two-dimensional optical lattices. These include Berry phase, self-rotation, spin-orbit coupling, and discrete solitons. Finally, we analyze in detail an approach to extract a small and deterministic number of atoms from a trapped Bose condensed gas by the introduction of an optical quantum dot. We show how small numbers of atoms in microtraps can be used for quantum state engineering.

Table of Contents

Acknowledgments **v**

Abstract **vii**

List of Tables **xi**

List of Figures **xii**

Chapter 1. Introduction **1**
1.1 Interaction of atoms with light 1
1.2 Bose-Einstein condensation 7
1.3 The study of condensed matter phenomena with ultracold atoms 9

Chapter 2. One-way wall **12**
2.1 Limitations of present cooling schemes 12
2.2 Model 13
2.3 Phase-space compression in stationary regime 17
2.4 Phase-space compression by moving wall 22
2.4.1 Model 24
2.4.2 Examples 28
2.4.3 Comparisons and limitations 30

Chapter 3. Quantum Tweezer **32**
3.1 BEC and a quantum dot 33
3.1.1 Number of atoms in BEC 33
3.1.2 Adiabatic energy levels 35
3.1.3 Depth of the dot and length scales of the problem . . . 38
3.1.4 Conditions for operation 42
3.2 Raising the dot in the middle 43

3.2.1 Dot potential in the center . . . 43
3.2.2 Adiabatic energy levels and extraction . . . 44
3.2.3 Variations and parameter fluctuations . . . 47
3.3 Nonlinear atom optics with a small number of atoms and multiparticle interferometry . . . 51
3.3.1 Quantum entanglement: previous experiments and suggestions . . . 52
3.3.2 Nonlinear atom optics processes with a small number of atoms . . . 53
3.3.3 The signature of multi-particle interferometry . . . 56
3.3.4 Model . . . 57
3.3.5 Discussion . . . 58
3.3.6 Experimental parameters . . . 64

Chapter 4. Optical Lattices **66**
4.1 Berry phase effects in asymmetric optical lattices . . . 66
4.1.1 Semiclassical equation of motion and Bloch theorem . . . 66
4.1.2 Berry curvature and self-rotation . . . 68
4.1.3 Tight-binding honeycomb lattice . . . 70
4.1.4 Continuous honeycomb lattice . . . 74
4.2 Discrete solitons . . . 81
4.2.1 Introduction . . . 81
4.2.2 Variational Approximation . . . 84
4.2.3 Effective Mass . . . 86
4.2.4 Delocalization . . . 89
4.2.5 Numerical Simulations . . . 92
4.3 Effective spin-orbit coupling . . . 101
4.3.1 Fictitious magnetic field . . . 103
4.3.2 Lattice configuration . . . 105
4.3.3 Effective Hamiltonian and Berry curvature . . . 106
4.3.4 Observation of anomalous and spin Hall effects . . . 109
4.3.5 Estimation of experimental parameters . . . 111

Appendices **121**

Appendix A. Expressions for compression and rate of compression **122**

A.1 Compression 122

A.2 Rate of Compression 123

Appendix B. Expressions for compression in a trap **125**

Appendix C. Polarization tensor for D_1 line **127**

Bibliography **130**

Vita **144**

List of Tables

3.1 Parameters of multi-particle interferometry scheme for ^{87}Rb and ^{23}Na. 65

C.1 Values of the Clebsch-Gordan coefficients 128

List of Figures

2.1 One-way barrier with a two-level atom. 14
2.2 Three-level atom model. 15
2.3 One-way barrier with alkali atoms. 16
2.4 Illustration of the phase space compression process 18
2.5 Analysis of Monte-Carlo simulation. 21
2.6 Diagram of moving one-way barrier approach. 24
2.7 Comparison between numerical simulation and the simple analytic expression for gravitational and harmonic traps. 28

3.1 Energies of the BEC-dot system when the dot is dragged from the BEC. 38
3.2 Energy of the bound state in the dot. Profile of the BEC wave function. 41
3.3 Potential and wave functions of the BEC and the dot. 45
3.4 Energies of the BEC-dot system when the dot is raised in the middle. 46
3.5 Probabilities to extract certain number of atoms 47
3.6 Effect of number of atoms fluctuation with linear and quadratic ramps in parabolic trap. 48
3.7 Effect of number of atoms fluctuation for exponential ramp in parabolic trap and for linear ramp in a box-shaped potential. . 49
3.8 Smaller frequency of transverse confinement and larger separation between dot beams 50
3.9 Wider beams of the dot. 51
3.10 Multiparticle-interferometry schematics 54
3.11 Adiabatic energy levels with repulsive interaction 57
3.12 Probability to find the system in the ground state for repulsive interaction. 60
3.13 Adiabatic energy levels for attractive interaction. 61

3.14 Probability to find systems in given states with attractive interaction 62
3.15 Beamsplitter operation. 63

4.1 Tight-binding model of the asymmetric honeycomb lattice. Brillouin zone. 71
4.2 Dispersion and Berry curvature of the tight-binding model . . 73
4.3 Distribution of the currents in the tight-binding model at K point 75
4.4 Continuous asymmetric honeycomb potential. Berry curvature. 76
4.5 Motion in real space when constant force is applied. Angular momentum along the trajectory. 78
4.6 Current at K point for the continuous potential. Illustration of non-adiabaticity. 79
4.7 Dispersion for the square lattice. Effective mass. Wave packet expansion. Comparison with analytic model. 115
4.8 Soliton dispersion. Spatial profile of the soliton. Collapse of the wave packet. 116
4.9 Dispersion and effective mass for honeycomb potential. Expansion of the wave packet and comparison with analytic model. . 117
4.10 Collapse of the wave packet on the honeycomb lattice. 118
4.11 Scalar and vector parts of the potential with fictitious magnetic field present. 119
4.12 Dispersion and Berry curvature. 120
4.13 Trajectory and analog of spin Hall effect. 120

Chapter 1

Introduction

1.1 Interaction of atoms with light

In this section, we briefly discuss how the interaction between light and matter appear and how it can be used to cool and trap atoms. This topic is discussed in great detail in many references, see for example [1–5]. Here we closely follow the reference [4] where dipole optical traps are reviewed.

An insight into atom-photon interaction can be obtained from the classcal Lorentz model where an atom is modeled by classical damped oscillator [6]. If the electric field $\mathbf{E}$ changes in time harmonically with frequency ω, it induces a dipole moment, p, in the classical oscillator that has the resonant frequency ω_0 and damping rate Γ_ω. Since the electrons are much lighter than nuclei the mass of the oscillator is electron mass, m_e. This induced dipole moment is proportional to the electric field and coefficient of proportionality is called polarizability α

$$p = \alpha E. \tag{1.1}$$

Note that we use standard convention when amplitudes p and E are complex and the measurable quantities are given by the sum of two complex conjugate expressions, for instance, time varying electric field is $\mathbf{E}(\mathbf{r}, t) =$

$\hat{\mathbf{e}}E(\mathbf{r})\exp(-i\omega r) + c.c.$. This induced dipole moment interacts with the electric field which results in the dipole potential quadratic in the field, that is proportional to the intensity

$$U_{\text{dip}} = \frac{1}{2}\langle \mathbf{pE} \rangle = -\frac{1}{2\epsilon_0 c}\text{Re}(\alpha)I \tag{1.2}$$

The factor of 1/2 is because the dipole is not permanent, but rather induced. Intensity is $I = 2\epsilon_0 c\,|E|^2$.

The classical equation of the damped harmonic oscillator is

$$m_e\left[\ddot{x} + \Gamma_\omega \dot{x} + \omega_0^2 x\right] = -eE(t). \tag{1.3}$$

Substituting harmonically a varying field and position, we find complex polarizability of

$$\alpha = \frac{e^2}{m_e}\frac{1}{\omega_0^2 - \omega^2 - i\omega\Gamma_\omega} = 6\pi\varepsilon_0 c^3 \frac{\Gamma/\omega_0^2}{\omega_0^2 - \omega^2 - i\frac{\omega^3}{\omega_0^3}\Gamma}. \tag{1.4}$$

For the classical model, damping rate results from the dipole radiation of the accelerated charge which is given by Larmor's formula [6]

$$\Gamma_\omega = \frac{e^2\omega^2}{6\pi\epsilon_0 m_e c^3}. \tag{1.5}$$

In the last expression in Eq. (1.4) we have introduced on-resonant damping rate $\Gamma = (\omega_0/\omega)^2\Gamma_\omega$. We should note that the induced dipoles are of quantum nature and, in general, damping rate is inversed Einstein coefficient A associated with the transition which is determined by the dipole matrix element between ground and excited state [2]

$$\Gamma = \frac{\omega_0^3 e^2}{3\pi\varepsilon_0\hbar c^3}\left|\langle r\rangle\right|^2. \tag{1.6}$$

For many atoms with a strong dipole transition the classical formula (1.5) provides very good approximation. For most of alkali atoms when detuning is much larger than the splitting between the two D lines (fine splitting), which combined oscillator strength is close to unity, the two formulas agree within a few per cent.

As we saw above, the real part of the polarizability results in the dipole potential. This potential is conservative and can be used for trapping of atoms. Imaginary part of the polarizability corresponds to absorption of energy. Absorbed photons are emmited spontaneously in all directions with equal probability. Hence a dissipative force can arise when absorption happens from one direction. This has been used to achieve laser cooling (for the review see [3]). Withing the classical model scattering rate can be expressed as

$$\Gamma_{sc} = \frac{P_{\text{abs}}}{\hbar\omega} = \frac{\langle \dot{\mathbf{p}}\mathbf{E} \rangle}{\hbar\omega} = \frac{1}{\hbar\varepsilon_0 c}\text{Im}(\alpha) I(\mathbf{r}). \tag{1.7}$$

The methods of laser cooling that rely on repeated absorption and emittion of photons (such as Doppler cooling and polarization gradient cooling) are limited to the temperature that corresponds to the velocity gained by an atom emitting a single photon, recoil velocity. For alkali atoms the recoil velocity is order of centimeters per second, and the limiting temperatures are order of 1μK. To reach such temperatures from room temperature (hundreds meters per second) many scattering events have to occur. This requires a cycling transition in the spectrum, that is, a transition for which spontaneous decay returns the atoms to the original state. This requirement is quite restrictive

since only for small fraction of atoms, let along molecules, such transitions exist in the easily accessible region of spectrum.

Based on the expression for complex polarizability given above the following expressions can be derived for the dipole potential and the scattering rate in case of large detunings, $\Delta = \omega - \omega_0$ and negligible saturation

$$U_{\rm dip}(\mathbf{r}) = -\frac{3\pi c^2}{2\omega_0^2}\left(\frac{\Gamma}{\omega_0-\omega}+\frac{\Gamma}{\omega_0+\omega}\right) I(\mathbf{r}) \approx \frac{3\pi c^2}{2\omega_0^2}\frac{\Gamma}{\Delta} I(\mathbf{r}), \quad (1.8)$$

$$\Gamma_{sc}(\mathbf{r}) = \frac{3\pi c^2}{2\hbar\omega_0^3}\left(\frac{\omega}{\omega_0}\right)^3\left(\frac{\Gamma}{\omega_0-\omega}+\frac{\Gamma}{\omega_0+\omega}\right)^2 I(\mathbf{r}) \approx \frac{3\pi c^2}{2\hbar\omega_0^3}\left(\frac{\Gamma}{\Delta}\right)^2 I(\mathbf{r}). \quad (1.9)$$

The approximate expressions are for the most commonly relevant case when detuning is much smaller than the resonant frequency $\Delta \ll \omega_0$ (this is so called rotating-wave approximation). Notice that in this regime

$$\hbar\Gamma_{sc} = \frac{\Gamma}{\Delta} U_{\rm dip}. \quad (1.10)$$

This expression shows that substantial dipole potential can be achieved with small number of spontaneous scattering events when detuning large and large enough intensity is chosen. Also the last expressions show that for red-detuned traps, when the laser is detuned below the resonance, $\Delta < 0$, the atoms are trapped in regions with larger intensity. In contrast blue-detuned beams, when $\Delta > 0$ produce a repulsive dipole potential.

In Chapter 2, we suggest how using the concepts discussed above to produce a one-way barrier. Atoms in ground state will pass through it in one direction but will be reflected in opposite. Such a barrier may consist of two beams: one blue detuned from the resonance producing repulsive potential

for the atoms in the ground state, another that excites atoms to the excited state for which the dipole potential produced by the other beam is attractive. Using such a barrier, one can collect atoms or molecules in a volume much smaller than original, thus increasing the phase space volume. In contrast to the methods mentioned above, this approach requires only a single scattering event.

In the discussion above quantum multiplicity of the states was ignored. In general, polarizability depends on the sub-level. Second-order time-independent perturbation theory can be applied for degenerate sub-levels to using the dressed state view for the system of atom and photon field [1, 7]. This matrix element between the ground state sublevels α and β can be written as

$$H_{\alpha\beta} = \sum_{\alpha\beta\gamma} \frac{\left(\mathbf{E}^*(\mathbf{r}) \cdot \mathbf{D}^*_{\gamma\alpha}\right) \left(\mathbf{E}(\mathbf{r}) \cdot \mathbf{D}_{\gamma\beta}\right)}{\hbar(\omega - \omega_\gamma)}. \tag{1.11}$$

Here, the interaction $\mathbf{E} \cdot \mathbf{D}$ between electric field and dipole is considered as perturbation, index γ labels excited state sublevels, ω is the frequency of the light, and ω_γ is the frequencies of the atomic resonanes. Note that applying this formula to a two-level atom gives an energy shift and expressing the dipole element $\mathbf{D}_{\alpha\gamma}$ in terms of natural linewidth Γ with Eq. (1.6) we find the energy shift

$$\Delta E = \pm \frac{3\pi c^2}{2\omega_0^3} \frac{\Gamma}{\Delta} I, \tag{1.12}$$

with plus sign for the ground state of the atom and minus sign for the excited state. Notice that this expression is the same as Eq. (1.8) obtained with the classical model. An additional insight is that the excited state also is shifted

but in the opposite direction of the ground state, that is blue detuned beam produces attractive potential for atoms in the excited state and red detuned beam produces repulsive potential for them. We use this fact when the specific model for one-way barrier is suggested.

As an illustration, we discuss state-dependent optical energy shifts using alkalii atoms which is also important for some future discussion. The strongest dipole transitions in alkalii atoms are D_1 ($^2S_{1/2} \rightarrow^2 P_{1/2}$) and D_2 ($^2S_{1/2} \rightarrow^2 P_{3/2}$). The splitting between the lines is due to spin-orbit coupling which is much larger than hyperfine splitting between ground and excited sublevels. When detuning is much larger than the hyper-fine splitting the optical shift that depends on projection of total angular momentum m_F is [4]

$$U_{\rm dip}(\mathbf{r}) = \frac{\pi c^2 \Gamma}{2\omega_0^3} \left(\frac{2 + P g_F m_F}{\Delta_{2,F}} + \frac{1 - P g_F m_F}{\Delta_{1,F}} \right) I(\mathbf{r}), \tag{1.13}$$

here g_F are Lande factors, $P = 0, \pm 1$ for linear and circular $\sigma^{\pm}$ polarizations of light correspondingly, the detunings $\Delta_{1,F}$ and $\Delta_{2,F}$ are with respect to frequencies correspoinding to transitions from the centers of the ground $^2S_{1/2}, F$ states to $^2P_{1/2}$ and $^2P_{3/2}$. When the detuning becomes much larger than fine-splitting $\Delta_{\rm FS}$ between two D lines the previous equation becomes

$$U_{\rm dip}(\mathbf{r}) = \frac{\pi c^2 \Gamma}{2\omega_0^3 \Delta} \left(1 + \frac{1}{3} P g_F m_F \frac{\Delta_{FS}}{\Delta} \right) I(\mathbf{r}). \tag{1.14}$$

Note that when the detuning is much larger than fine-splitting the shifts for all sublevels are just like for two-level atom.

1.2 Bose-Einstein condensation

In the typical laser cooling schemes such as Doppler cooling, ultracold gases are obtained. Their temperatures can be around 10μK and the density around 10^{12} cm^{-3}. The thermal de Broglie wavelength of the atoms for a given temperature T is conventionally defined as

$$\lambda_T = \left(\frac{2\pi\hbar^2}{mk_BT} \right)^{1/2}. \tag{1.15}$$

When the temperature decreases and the density n stays constant at some point it becomes comparable to the separation between atoms $n^{-1/3}$. Then the quantum nature of the atoms becomes important. For bosons a transition to a Bose-Einstein condensate (BEC) occurs, where a macroscopic number of atoms are described by a single wave function.

Laser cooling does not achieve BEC because for densities around 10^{12}-10^{13} cm^{-3} temperatures around 100 nK are required. Typically, the ultracold atoms are trapped in potentials created by magnetic fields or optical dipole traps that can be approximated by harmonic wells. Even though lowering the frequency of confinement decreases the temperature, it does not bring the atoms closer to condenstation since the density will decrease and as a result the transition temperature also decreases. It is important to increase phase space density which cannot be achieved in conservative traps due to Liouville's theorem of mechanics. The condensation of the ultracold dilute gases was succesfully achieved with evaporative cooling [8–10]. During evaporative cooling, the gas is kept in a trap and the most energetic particles are removed

selectively. The particles that remain equilibrate to a higher temperature, and as a result to lower phase space densities since the trap does not change.

After the evaporative cooling, a very small fraction (tenth of a percent or less) of initial atoms in the trap remains. Also the scheme requires equilibration on a time scale much shorter than the duration of the evaporation. In Chapter 2, we suggest the use of a moving one-way barrier to trap atoms at the appex of their trajectory in the trap. We analyse the problem in a regime complimentary to evaporative cooling, when no equilibration of less energetic atoms occurs. We show that a decrease in phase space density can be achieved this way.

In the other chapters, we deal with the dynamics of the BEC in potentials created by light. The Gross-Pitaevskii (GP) equation describes the dynamics of BEC of dilute gases very well [11]

$$i\hbar\frac{\partial}{\partial t}\psi(\mathbf{r},t) = \hat{H}\psi(\mathbf{r},t) = \left(-\frac{\hbar^2}{2m}\nabla^2 + V(\mathbf{r}) + U_0\left|\psi(\mathbf{r},t)\right|^2\right)\psi(\mathbf{r},t), \quad (1.16)$$

here ψ is the wave function, the coupling constant U_0 depends on the s-wave scattering length a and number of atoms in the condensate N: $U_0 = \frac{4\pi\hbar^2 a}{m}N$.

In several places, we consider the situations where the BEC is strongly confined in one or two dimensions, so that the dynamics in those direction is "frozen out" [12]. Such a regime has been succesfully implemented experimentally [13]. The condensate can be considered effectively two-dimensional when the third direction is confined by a trap with harmonic oscillator splittings in that direction $\hbar\omega_z$ is much larger than the three-dimensional chemical

potential of the BEC μ

$$\mu \ll \hbar\omega_z. \tag{1.17}$$

In this case, the dynamics in the strongly confined direction "freezes" into the ground state of a harmonic oscillator $\phi(z)$, the total wave function then may be written as $\psi(\mathbf{r}) = \phi(z)\psi(x, y)$ and Eq.(1.16) may be written for two-dimensional $\mathbf{r}$ with

$$U_{0,1\mathrm{D}} = \left(\frac{8\pi\omega_z\hbar^3}{m}\right)^{1/2} aN. \tag{1.18}$$

In case when two directions are strongly confined

$$\mu \ll \hbar\omega_{y,z} \tag{1.19}$$

the GP equation becomes one-dimensional with coupling constant

$$U_{0,2\mathrm{D}} = 2\hbar\omega_{y,z}aN. \tag{1.20}$$

1.3 The study of condensed matter phenomena with ultracold atoms

In the last decade, many experiments have studied the quantum motion of ultracold atoms in periodic potentials created by standing waves of light [14]. Phenomena, such as Bloch oscillations and Wannier-Stark ladders, impossible to observe for electrons in metals due to short relaxation times, have been observed. An electric field results in constant force for electrons. This is mimicked with neutral atoms by accelerating the lattice with constant acceleration. In the reference frame where the lattice is stationary the atoms

experience constant inertial force. Similarly, a magnetic field can be reproduced by rotating the lattice.

In this dissertation in Chapter 4, we study wave packet dynamics of ultracold atoms in 2D optical lattices, revealing a number of novel phenomena involving Berry phase, self-rotation, spin-orbit coupling, and discrete solitons. The simplest system where the Berry phase and self-rotation manifest themselves is a 2D lattice with broken inversion symmetry. They result in transverse drift during Bloch oscillations and non-zero angular momentum. In spin-dependent lattices effective coupling between atomic spin and its momentum can be produced in similar form to Rashba spin-orbit coupling for 2D electrons in semiconductors. As a result, effects similar to the anomalous and spin Hall effects can be observed directly. For interacting atoms in the parts of the Brillouin zone where the effective mass is negative, sufficiently strong repulsive interaction may cause a wave packet to collapse into discrete solitons.

In Chapter 3, we consider a system which is reminiscent of a Coulomb blockade of electrons in quantum well. In our case, a quantum dot well, created by a tightly focused laser beam, is placed in the center of a BEC confined in a quasi-one-dimensional configuration [15]. We show that for certain parameters it is possible to extract a single atom from a BEC by raising the depth of the well at a given rate. This is possible due to rapid decoupling of the quantum dot and BEC reservoir when the state with a single atom in the dot is just below a chemical potential of the BEC. The analysis is done for

realistic experimental parameters for a ^{87}Rb condensate where the density is limited by three-body collisions. The realization of atomic number states should enable many applications in quantum state engineering [16].

Chapter 2

One-way wall

2.1 Limitations of present cooling schemes

The successful approach to reach quantum degenerate regime for gases of ultracold atoms was to use laser cooling [3] followed by evaporative cooling [17–19]. Both of these methods have some shortcomings. In this chapter we discuss an alternative way to compress phase space volume which relies on a one-way barrier for atoms that transmits atoms in some state in one direction and reflects atoms in that state when they are incident on it from another side [20, 21]. Phase space compression can be achieved in regimes, which is in many respects complimentary to those of laser cooling and evaporative cooling.

Laser cooling of atoms relies on multiple scattering of the photons. Due to the Doppler shift, the scattering of the photons is preferential for atoms moving towards the beam. The major limitation of the laser cooling is the requirement of a cycling transition. This limits, the applicability of the method to a small set of atoms in the periodic table. Further cooling below the single photon recoil limit was made possible by creating dark states in momentum space using quantum interference [22] or stimulated Raman transitions [23]. Dark states in position space have been based on creating selective regions

where laser cooling turns off due to optical pumping to a dark state [24, 25]. More recently collective-emission-induced cooling was demonstrated using an optical cavity [26]. These methods, however, could not demonstrate compression in phase-space density to reach quantum degeneracy in the dilute gases.

Evaporative cooling was originally suggested as a means to achieve Bose-Einstein condensation in atomic hydrogen [17–19]. Its application to magnetically trapped alkali atoms [9, 27] culminated in the first observation of Bose-Einstein condensation in atomic vapors [8–10]. Since then it has been an essential process by which to obtain degenerate quantum gases. Nevertheless it has shortcomings. The main two are: (i) Almost all atoms originally trapped to produce the condensate are lost during the evaporation process. (ii) The time scale for collisions leading to thermal equilibrium must be short compared to the time employed to form the condensate. The latter shortcoming is especially severe for fermionic atoms, since for two fermions in the same state, s-wave scattering is forbidden by the Pauli exclusion principle. Currently, degenerate fermionic gases can only be obtained by a combination of evaporative and sympathetic cooling [28] in the presence of bosonic atoms or different states of the fermionic atoms [29].

2.2 Model

We first describe a simple two-level model illustrating the mechanism for one-way barrier. Consider a two-level atom with ground state $|1\rangle$ and an excited state $|2\rangle$ that decays spontaneously back to the ground state with a

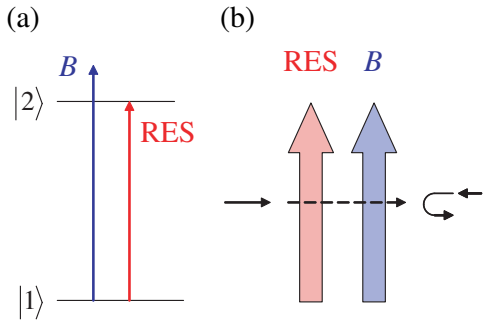

Figure 2.1: The first scheme for uni-directional wall. Beam B blue detuned from the resonance creates repulsive potential for atoms in state $|1\rangle$. Beam RES is tuned to atomic resonance.

lifetime τ. One laser beam, denoted B is tuned to the blue of the atomic transition, while another beam, denoted RES, is tuned exactly on resonance, as shown in Fig. 2.1(a). We construct a barrier as shown in Fig. 2.1(b); On the left side is a focused RES sheet, and to the right of that a focused B sheet. An atom impinging from the right will encounter the B sheet which is a repulsive barrier and it will be reflected back. In contrast, an atom impinging on the barrier from the left will first be promoted to the excited state $|2\rangle$ with some probability. It then encounters the barrier which is attractive for that state, so it goes through. We must assume that the spontaneous lifetime is longer than the transit time of the atom through the barrier, and that the atom decays to the ground state after crossing the barrier. Clearly, this wall reflects atoms from the right and transmits them from the left.

In the work independent of ours [30] the authors suggested to use stim-

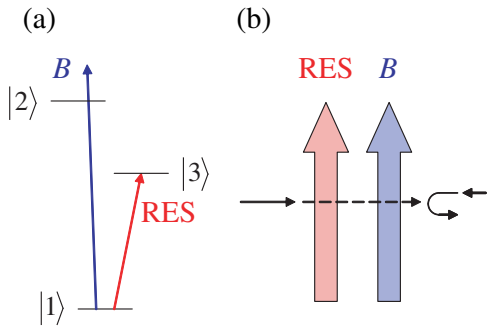

Figure 2.2: Extension of the scheme in Fig. 2.1 to a three level atom. Transition $|1\rangle \rightarrow |2\rangle$ is a strong dipole transition to create a substantial repulsive wall for state $|1\rangle$. Level $|3\rangle$ is metastable with lifetime comparable to transit time through beams.

ulated Raman adiabatic passage (STIRAP) to optimize the excitation stage. In that configuration, two Raman beams replace the RES beam and achieve almost full excitation independent of velocity of incoming atoms.

As a physical realization of the two-level, model we consider a three-level model as illustrated in Fig. 2.2(a). The ground state $|1\rangle$ has one allowed dipole transition to state $|2\rangle$, and another weak transition to state $|3\rangle$. Such configuration makes it possible to produce a strong repulsive wall with an allowed dipole transition and a relatively long-lived state for which this wall is nearly transparent. A uni-directional barrier can be constructed in this case in the same way as for the two level model, except that the repulsive barrier should be a beam tuned to the blue of the $|1\rangle \rightarrow |2\rangle$ transition, while the resonant beam is tuned to the $|1\rangle \rightarrow |3\rangle$ transition. The barrier is illustrated

in Fig. 2.2(b). An atom coming from the right in the ground state is reflected from the repulsive barrier. An atom coming from the left first encounters the resonant beam and is excited to the long-lived state $|3\rangle$. Assuming that the blue-detuned beam is close to the $|1\rangle \rightarrow |2\rangle$ transition, it will generally be completely non-resonant when the atom is in state $|3\rangle$ and the atom can pass through the barrier.

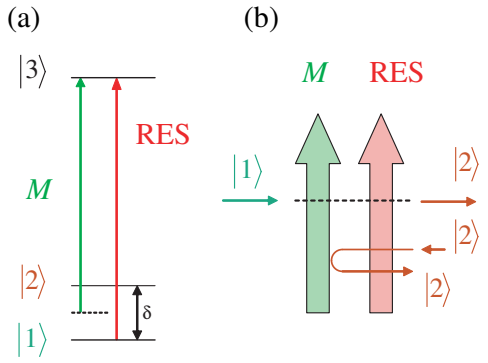

Figure 2.3: Scheme that may be used to create a uni-directional wall for the case of alkali atoms. Beam M is attractive for state $|1\rangle$ and repulsive for $|2\rangle$. Beam RES transfers atoms from $|1\rangle$ to $|2\rangle$ in a few scattering events.

This scheme can be realized in alkaline earth atoms. For example, calcium has a ground state $|g\rangle$ and a transition to one excited state $|e1\rangle$ with a wavelength of 423 nm and lifetime of 5 ns, and a transition to another excited state $|e2\rangle$ with a wavelength of 657 nm and lifetime of 330 μs. In this case, the B sheet would be tuned to the blue of the 423 nm transition (far enough to minimize spontaneous scattering) while the RES sheet would be tuned to the 657 nm transition. The resonant beam must be spectrally broadened in

an experimental realization so that Doppler shifts are not important.

For alkali atoms, one-way barrier may be constructed as shown in Fig. 2.3. For atoms in state $|1\rangle$ the beam M is attractive, since it is detuned to the red side of the transition. The state of the atoms is changed to $|2\rangle$ by the beam RES in a few scattering events. This state is not affected by the beam RES and the beam M is a repulsive wall for it. For example, in Cesium, which has a ground hyperfine state splitting of 9.2 GHz the beam M would be tuned 4.6 GHz to the red of the ${}^2S_{1/2},\ F = 3 \rightarrow {}^2P_{3/2},\ F = 4$ transition at 852 nm, the RES beam would be tuned to the transition.

One limitation of these methods is that typical dipole trap depths are only a few mK. This requires therefore that atoms or molecules be pre-cooled using other methods which are not laser-based. In recent years there has been enormous progress in this direction and several methods have already been demonstrated experimentally. These include buffer-gas cooling [31, 32], Stark deceleration [33], and rotating supersonic nozzle [34].

2.3 Phase-space compression in stationary regime

How can such a one-way barrier be used to compress phase space? Consider a 1D box of length L with a spatially uniform distribution of atoms. Now suppose we turn on a uni-directional barrier somewhere in the box, as shown in Fig. 2.4 (a). After some time, all of the atoms will be trapped in one region, as illustrated in Fig. 2.4 (b).

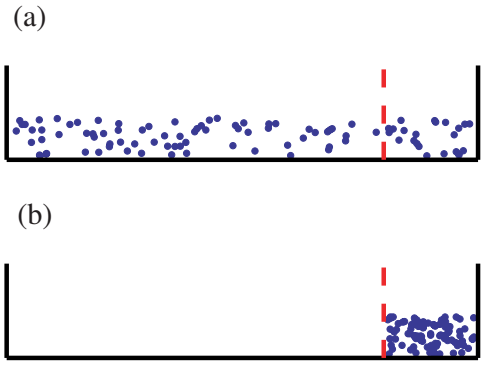

Figure 2.4: Illustration of the cooling process. As the uni-directional wall is placed inside of a billiard, atoms are accumulated in the smaller part, thus increasing the density. Kinetic energy increase is due to photon recoil as atoms decay to ground state.

To study this simple model further, we have performed a Monte-Carlo simulation and compared with a simple analytic model. We start with atoms uniformly distributed in a 1D billiard and with a Maxwell distribution in velocity with standard deviation σ_v. A semi-penetrable wall with width $2d$ separates the billiard into two parts with widths $l_1 > l_2$, so that the resonant part of the wall with width d borders with longer side and the blue detuned part of the same width borders the shorter side. We assume that external walls of the billiard are repulsive for both states. As soon as an atom enters the resonant beam, it gets transferred to state $|2\rangle$ for which the second half of the wall is attractive. We simulated exponential decay of the atom with decay time τ. As the atom decays it gains one recoil velocity v_r in a random direction. The equilibration time is much longer than accumulation time. Three different cases are considered in the simulation: (i) Decay occurs in the small region.

In this case, the particle is trapped. (ii) Decay occurs in the large region or in the resonant beam. In this case, the particle is not trapped, but gets another chance and eventually will be trapped. (iii) Decay occurs in the repulsive wall. In that case, the particle is considered lost from the distribution, since it would acquire a large kinetic energy as it exits the barrier.

The model has six parameters: d, v_r, τ, l_1, l_2, σ_v. The unit of length, L_u, is taken to be d, and the unit of velocity, v_u, is taken to be v_r. The unit of time is then $t_u = L_u/v_u = d/v_r$. We observe how a change of parameters (τ, l_1, l_2, and σ_v) affects the performance, which we characterize by two figures of merit. The first one is compression in phase space

$$C = e\frac{(l_1 + l_2 + 2d) \cdot \sigma_v}{l_2 \cdot \sigma_{v,\text{final}}}, \tag{2.1}$$

where e is the ratio of number of trapped atoms to number of initial atoms. The second figure of merit is the average rate of phase space change C/T_f, where T_f is the time it takes to capture a fraction f of the atoms. For the discussions below we use the time when ninety percent of trappable atoms are captured, $T_{0.90}$.

Figure 2.5(a) shows the velocity distribution for 50000 atoms before and after the process for the following parameters: $\tau = 10$, $l_1 = 100$, $l_2 = 10$, $\sigma_v = 5$. In the plots (c)-(f) in Fig. 2.5 variations of the parameters are performed with respect to this set. Figure 2.5(b) displays the distribution of capturing times. For this particular set of parameters we find a compression factor, $C = 9.2$.

As the length of bigger part of the billiard, l_1, increases (Fig. 2.5(c)) the compression factor increases, the average time of the operation increases as well and as a result the rate of compression saturates. For a particular initial velocity distribution and wall width there is an optimal decay time for which the compression is the largest (Fig. 2.5(e)). Average rate of compression in this case decreases monotonically (Fig. 2.5(f)).

Naturally, the operation of the scheme is optimal when the decay rate is much larger than the time most of the particles spend in the gap and much smaller than the time it takes one particle to cross the smaller region: $t_{\rm gap} \ll \tau \ll t_{\rm travel}$. Also the size of the wall should be much smaller than the size of the both regions: $d \ll l_1, l_2$. In these limits, we can obtain simple analytic expressions for phase space compression and compression rate (see Appendix A).

When we define the fraction of originally trapped particles $f_0 = l_2/(l_1 + l_2)$ the compression in phase space density is given by

$$C = f_0 \frac{\sigma_v}{\sqrt{f_0 \sigma_v^2 + (1 - f_0)(\sigma_v^2 + v_r^2)}}. \tag{2.2}$$

In two following limits it becomes

$$l_1 \gg l_2, \sigma_v \gg v_r, \qquad C = \frac{l_1}{l_2}, \tag{2.3}$$

$$l_1 \gg l_2, \sigma_r \ll v_r, \qquad C = \frac{l_1}{l_2}\frac{\sigma_v}{v_r}, \tag{2.4}$$

hence the scheme is only efficient in the first limit when the initial velocity spread is much larger than the recoil velocity. In this limit it is also applicable

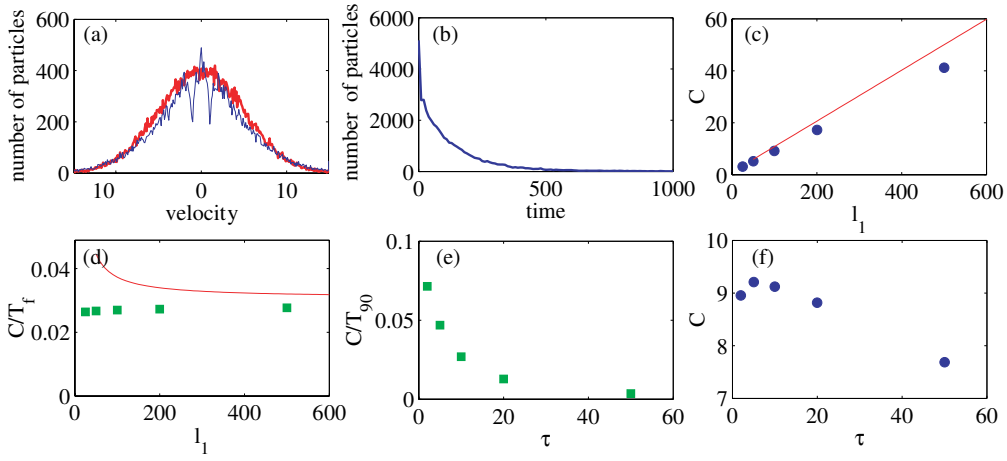

Figure 2.5: (a) Initial and final velocity distributions for parameters $\tau = 10$, $l_1 = 100$, $l_2 = 10$, $\sigma_v = 5$. Total initial number of particles is 50000. (b) Distribution of times after which particles end up in the smaller region. (c) Change of compression in phase space, solid line is for analytic expression given by analytic formula (2.2), limiting case (2.3) is not distinguishable from it in this regime. (d) Average compression rate as size of the larger region l_1 is varied, with $f = 0.90$, the lines show the average compression rate estimated from (2.6) with $f = 0.95$. The numerical solution of (2.5) give indistinguishable result in this regime as well. (e) and (f) the same when decay time, τ, is varied.

in two and three dimensions hence the recoil that might be accumulated in the transverse dimension will not be significant. In Fig. 2.5(c) we show that for appropriate decay times the agreement between this simple analytic formula and the results of Monte-Carlo simulations is very good.

To estimate the time T_f it takes to capture a fraction f of particles one has to solve the following nonlinear equation (see Appendix A)

$$f_0 + (1 - f_0)\left[\frac{1}{\tilde{v}_0}\sqrt{\frac{2}{\pi}}\left(1 - e^{-\frac{\tilde{v}_0^2}{2}}\right) + \mathrm{erfc}\left(\frac{\tilde{v}_0}{\sqrt{2}}\right)\right] - f = 0, \qquad (2.5)$$

here $\tilde{v}_0 = 2l_1/\sigma_v t$ is velocity, in units of σ_v, above which all particles are captured in the smaller region. In the limit $l_1 \gg l_2$, $\sigma_v \gg v_r$ and when $\tilde{v}_0 \ll 1$, i.e. $(1-f) \ll 1$ the equation can be linearized (see Appendix A) and the average rate is given by

$$\frac{C}{T_f} = \frac{1-f}{1-f_0}\frac{\sigma_v}{l_2}\sqrt{\frac{\pi}{2}} \tag{2.6}$$

which is independent of l_1. Such dependence is seen in Fig. 2.5(d). This simple formula captures the behavior and the result is in reasonable agreement with the simulation, however does not take into account loss of the particles.

2.4 Phase-space compression by moving wall

Evaporative cooling relies on removing atoms above certain energy while remaining particles equilibrate to larger phase space densities. In a non-uniform trap there is relationship between energy of the particles and position: the removal of the energetic particles happens at some particular position. During the evaporative cooling this position is swept towards the minimum of the potential, atoms with smaller and smaller energies are removed, until the remaining atoms equilibrate to significant phase space densities.

Here we demonstrate that by slowly sweeping a one–way wall through a general trapping potential, the particles naturally compress into a state of very low energy: energetic particles are not removed but rather re-captured with smaller energy. The basic idea is illustrated in Figure 2.6. At any given time, all particles remaining in region A to the right of the potential have energy

less than $V(x_b)$. When the wall moves slightly to the right, the particles that reach it are at their turning point, and have very small kinetic energy. As the one-way barrier continues to move to the right, for a convex potential, as the particles bounce off the moving wall, they lose more energy in the collision than they gain otherwise. In this way, a slow sweep of the semi–permeable barrier through the convex well reduces particle energies to very low values set by the speed of the sweep.

The conditions needed for this optical compressor to work are quite different from those required for the effectiveness of evaporative cooling. The optical compressor relies upon the existence of a non-equilibrium distribution of particles to the right of the wall. In particular, the velocities of particles that reach the semi–permeable barrier from the right are all very low, rather than being given by the Maxwell–Boltzmann distribution that would describe them in equilibrium. Thus the process of compression must be fast compared to the thermal equilibration time of the particles. On the other hand, the sweep of the wall cannot occur too quickly, because the kinetic energy of particles after they traverse the wall is given by a positive power of the wall velocity.

Thus, the optical compressor provides a process completely complementary to evaporative cooling: (i) No atoms are lost during the compression process. (ii) The time scale for collisions leading to thermal equilibrium must be long compared to the time spent sweeping the semi–permeable barrier. We note that as the equilibration time becomes comparable to the time of the sweep, phase space compression will occur due to combination of evaporative

t

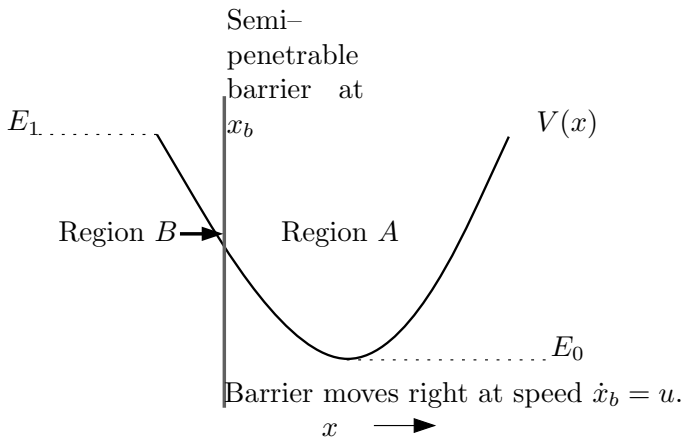

Figure 2.6: Functional diagram of the optical phase–space compressor in a trap. Particles begin in region A with characteristic energies $k_B T$. Particles arriving at the semi–permeable barrier from the right travel through it, while those in region B arriving from the left are reflected. The semi–permeable barrier moves to the right at speed $u = \dot{x}_b$, transferring particles from region A to region B, where their maximum kinetic energy is much less.

cooling in region A and the process discussed here.

2.4.1 Model

We consider an ideal collisionless gas trapped in a one-dimensional potential $V(x)$; two other dimensions are either untrapped or confined in a box-shaped potential. The gas is originally in thermal equilibrium at temperature $T = 1/k_B\beta$. An ideal infinitely thin semi–permeable barrier is located at position x_b, which is originally far to the left of any particles. The barrier moves to the right with velocity $u = \dot{x}_b$, its intersection point with the well moving from E_1 to E_0 and eventually passing through the whole well and out the right

hand side.

In the limit of slow wall velocities it is possible to obtain analytical results. We first focus on the distribution of velocities with which particles cross the barrier, and then consider the question of how their velocities change after they have crossed the barrier.

Particles with energy E are not affected by the wall until the wall reaches the point where $V(x_b) = E$. Let the period of oscillation of a particle of energy E in region A be $\mathcal{T}(E)$. We assume that there are

$$n(E)dE \propto D(E)e^{-\beta E}dE \tag{2.7}$$

particles near energy E, and that their positions in the trap are random. Here $D(E)$ is the energy density of states in the trap. Therefore, from the time the first particle of this energy passes through the barrier, until the last one leaves, there passes a time $\mathcal{T}(E)$. The last particle to be captured is one that had just passed the turning point and was headed to the right as the barrier reached energy E. Particles of energy E will pass at a uniform rate through the barrier during the time interval $\mathcal{T}(E)$. The first particle to pass the barrier will have no kinetic energy, while the last one through will have kinetic energy

$$K = -\frac{\partial V}{\partial x_b} u\mathcal{T}(E) \equiv \dot{E}\mathcal{T}. \tag{2.8}$$

Here $\dot{E}$ gives the rate at which the intersection point of the barrier with the potential well decreases in energy per time. We emphasize that we are using here the assumption that compression is fast compared to the thermal equili-

bration time, or else the kinetic energies of particles escaping the trap would be described by a Maxwell–Boltzmann distribution with temperature T.

Once particles have passed the semi–permeable barrier, they collide repeatedly with the barrier as it moves to the right and reflect from it. They lose energy to the barrier in this process. The final energy of each particle can be determined by observing that the process is adiabatic in the sense of mechanics, so that the action $I = \oint pdq$ is conserved [35]. Consider a particle that has kinetic energy K and total energy E as it passes through the barrier. If the kinetic energy K is not too large, the potential in region B can be treated as linear, and one computes that the particle has action

$$I = \frac{2}{3}\frac{(2mK)^{3/2}}{mF}, \tag{2.9}$$

where m is the particle mass, and $F = \left|V'(E)|_{x:V(x)=E}\right|$ is the slope of the potential. As the wall continues to move to the right, this action is preserved, allowing one to determine the final energy e of the particle once the barrier has swept all the way through the trap. We define in particular the function

$$K(e, E). \tag{2.10}$$

which gives the initial kinetic energy of the particle in terms of its total final energy e, and its initial energy E when it crossed the barrier.

Thus we have the following expression for the distribution of particle energies $f(e)$ in region B at the end of the compression process:

$$f(e) \propto \int_{E_0}^{E_1} dE \frac{dK}{de} \frac{\theta(K(e,E))\theta(\dot{E}\mathcal{T} - K(e,E))D(E)e^{-\beta E}}{\dot{E}\mathcal{T}}, \tag{2.11}$$

Here θ is the Heaviside step function. This expression follows by noting that the $n(E)dE$ particles with potential energy E cross the barrier with kinetic energies K evenly distributed between 0 and $\dot{E}\mathcal{T}$. The energies E_0 and E_1 are the minimum and maximum intersection points of the semi–permeable barrier with the potential well, as indicated in Figure 2.6.

The distribution $f(e)$ in Eq. (2.11) does not describe a case of thermal equilibrium. Once the compression process has terminated, we expect that the gas will be maintained for times long compared with the thermal equilibration time. The total energy of particles in the trap will be conserved in this process. Thus the end result will be a thermal distribution of particles with average energy $\bar{e}_f = E/N$ and temperature T_f that may be found from the system of three equations with three unknowns (entropy S, free energy F, and temperature T) [36]:

$$\begin{gathered} F = -NT \ln \tfrac{e}{N} \int e^{-\frac{1}{k_B T} \left[\frac{p^2}{2m} + V(x)\right]} \frac{dxdp}{2\pi\hbar}, \\ S = -\tfrac{\partial F}{\partial T}, \\ E = F + TS. \end{gathered} \tag{2.12}$$

We characterize this final equilibrium distribution by the efficiency γ, defined to be the ratio of phase space density before and after compression [37]:

$$\gamma = \frac{\Gamma_f}{\Gamma_i} = \exp\left(\frac{S_i - S_f}{k_B N}\right). \tag{2.13}$$

Note that for a power–law potential $V(x) = Ax^n$, moving from initial average energy $\bar{e}_i$ to final average energy $\bar{e}_f$ the solution of the system (2.12) above gives the compression (see Appendix B)

$$\gamma = \frac{\Gamma_f}{\Gamma_i} = \left(\frac{\bar{e}_i}{\bar{e}_f}\right)^{\frac{1}{2}+\frac{1}{n}}. \tag{2.14}$$

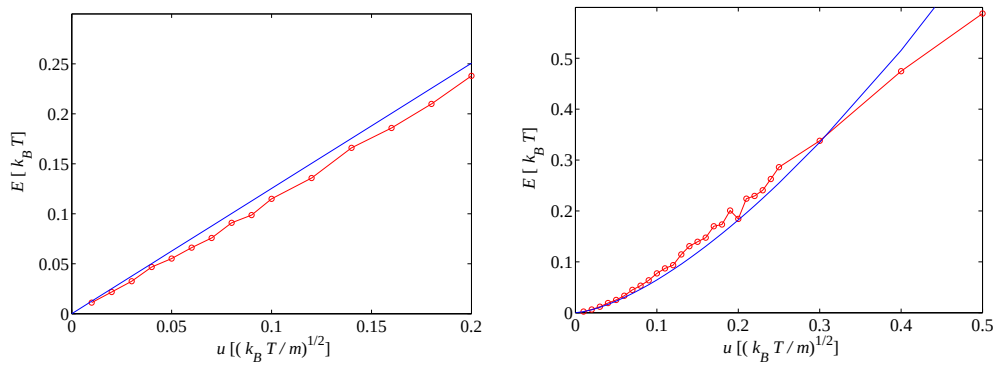

(a) (b)

Figure 2.7: (a) - Gravitational trap. Final energy. Straight line is the analytic result discussed in the text. Connected dots is numeric simulation. The wall is initially placed at $E = 10k_BT$. Each point is average of $N = 1000$ particles. (b) - Parabolic trap. Final energy. Straight line is the analytic result discussed in the text. Connected dots is numeric simulation. The wall is initially placed at $E = 3k_BT$. Each point is average of $N = 1000$ particles.

2.4.2 Examples

We now provide examples of two different trapping potentials, and calculate their effectiveness in cooling dilute gases.

First, consider the *gravitational trap*, defined by

$$V(x) = \begin{cases} -Ax & \text{for } x < 0 \\ \infty & \text{else.} \end{cases} \tag{2.15}$$

Density of states for the trap is $D(E) \propto \sqrt{E}$. As the semi–permeable barrier moves through this potential, the shape of region B does not change, and therefore the kinetic energy of a particle when it passes the barrier precisely equals its final total energy; that is, $K(e, E) = e$. Carrying out a computation

involving the period of motion in such a potential, we find

$$f(e) = B_1 \exp(-e^2/e_0^2), \tag{2.16}$$

$$\text{where } e_0 = 2\sqrt{2}u\sqrt{mk_BT}. \tag{2.17}$$

Here erfc(x) is the complementary error function and B_1 is a normalization coefficient. From this distribution we obtain the average energy after compression,

$$\bar{e}_f = \sqrt{\pi/2}u\sqrt{mk_BT}. \tag{2.18}$$

and the efficiency

$$\gamma = \left(\frac{\bar{e}_i}{\bar{e}_f}\right)^{3/2} = \left(\frac{9}{2\pi}\frac{k_BT}{m}\right)^{3/4}\frac{1}{u^{3/2}}. \tag{2.19}$$

The average energy vanishes as velocity of the wall goes to zero.

As a second example, consider a parabolic potential

$$V(x) = \frac{1}{2}Ax^2. \tag{2.20}$$

In this case density of states $D(E)$ does not depend on energy. Employing Eq. (2.9)

$$K(e,E) = \left[\frac{3\pi}{2}\sqrt{E}e\right]^{2/3} \tag{2.21}$$

In this case the energy distribution is given by

$$f(e) = B_2\left(\frac{e_0}{e}\right)^{1/3}\Gamma\left[\frac{5}{6}, \left(\frac{e}{e_0}\right)^4\right], \tag{2.22}$$

$$\tag{2.23}$$

$$\text{where } \; e_0 = \epsilon_0\left(u\sqrt{\frac{m}{k_BT}}\right)^{3/2}k_BT, \tag{2.24}$$

and $\Gamma[a,x] = \int_x^\infty dt e^{-t} t^{a-1}$ is incomplete Gamma function [38], B_2 is another normalization constant and $\epsilon_0 = 2 \cdot 2^{3/4}(2\pi)^{3/2}/3\pi$. The average energy after the process is

$$\bar{e}_f = C m^{3/4} u^{3/2} (k_B T)^{1/4} \tag{2.25}$$

where $C = \epsilon_0 \frac{2}{5}\Gamma[\frac{5}{4}] \approx 2.038$. The efficiency in this case has the same scaling in dependence on parameters only different numerical prefactor

$$\gamma = \frac{\bar{e}_i}{\bar{e}_f} = \frac{1}{C}\left(\frac{k_B T}{m}\right)^{3/4} \frac{1}{u^{3/2}}. \tag{2.26}$$

We performed numerical simulations of the process by randomly generating a particle with a certain energy in the gravitation and harmonic potentials. We solved the equation of motions until the wall reached the lowest point of the the gravitation potential or the symmetric point in the trap in the case of the harmonic potential. The procedure was repeated for N particles with average energy corresponding to the temperature. The results of the simulation are shown in Fig. 2.7(a) and Fig. 2.7(b). They are in quite good agreement with the analytic formulas for small velocities.

2.4.3 Comparisons and limitations

Because the one-way wall for an atomic barrier relies upon different internal states, it truly diminishes the system entropy as a Maxwell demon would, except for the unavoidable heating due to recoil of a photon motion. This can be captured as the cooling effect as described here. By comparison, in a plasma, where analogous one-way walls were proposed in the radio frequency

regime [39], there is no opportunity to change internal states of the plasma ions. Instead, the one-way ponderomotive-effect wall operates through Hamiltonian forces only, thereby conserving phase space. Thus, no matter how the wall is moved, no real cooling can take place. In the end, if the plasma ions occupy the same volume in space, they would of necessity occupy the same volume in velocity space – and hence not achieve a cooling effect. Note, however, that while the one-way radio-frequency wall does not cool plasma, it can force ions or electrons to move in one direction only. Thus, plasma current can be driven by plasma waves, which can be useful for a variety of plasma applications [40].

The limitation of the semi-permeable wall is that it results in heating of atoms to a single photon recoil $mv_r = \hbar k_L$. As the wall velocity reduces, the process becomes inefficient. If the temperature of the gas is originally n_r recoils; i.e. $k_B T = n_r^2 E_r$ where $E_r = \hbar^2 k_L^2/2/m$, then assuming that the final energy is E_r we find the slowest velocity with which it is still advantageous to move the wall in case of the parabolic trap is

$$u \approx \frac{0.15}{n_r^{1/3}} v_r. \tag{2.27}$$

In particular, if we start with a temperature of 10 recoils, the minimum wall velocity comes out to be $u = 0.05 v_r$. If velocity relaxation happens on time scale τ, the size of the trap can then be $u\tau$. For alkalies, τ can be as long as tens of seconds; hence in this case the size of the cloud is on the order of centimeters.

Chapter 3

Quantum Tweezer

It has been suggested in [15] to use a tightly focused laser beam (quantum dot) to extract a small number of atoms from a BEC. It has been shown that the fluctuation of number of extracted atoms may be negligible — a number Fock state is created in the dot. Motivated by the current experiments in progress [41, 42] ,we analyze the original suggestion where the quantum tweezer is dragged out of the BEC and a modified version where the coupling between the BEC and the dot is reduced by raising the potential at a fixed position in the center of the BEC.

A major advantage of the method in comparison to just trapping an atom from a background vapor [43] is that the atoms are in the ground state of the potential created by the focused beam and no additional cooling is required. A small number of neutral atoms in the ground state of tight potentials have attracted a lot of attention recently as systems to create entanglement between atoms. In the last section of this chapter, we give a brief overview of the previous work and discuss how interactions between small numbers of atoms in quantum tweezers can produce entangled states. We illustrate how these states may be, for instance, used for multiparticle interferometry [16].

3.1 BEC and a quantum dot

In this section, we outline the ideas that were originally suggested in [15] and described in detail in [44]. In particular, we provide the results of the calculations based on the model described in [15, 44] relevant for implementation with ^{87}Rb atoms, currently being pursued [41, 42, 45]. First, based on the parameters of a trap, we estimate the maximum number of atoms possible in the long-lived BEC. For the operation to be effective, the depth of the dot needs to be chosen so that conditions on length scales are fulfilled. These include relationship between the width of the BEC boundary, the location of the avoided crossings and spacing between them. After obtaining the parameters, we briefly illustrate the idea behind the tweezer in the dragging regime.

3.1.1 Number of atoms in BEC

The maximum number of atoms in a BEC is limited by three-body losses. When the density is above critical the BEC is short-lived because of that. We estimate the maximum number of atoms as

$$N < \frac{\rho_{\text{crit}}}{\rho_x \rho_y \rho_z}, \tag{3.1}$$

where ρ_{crit} is the largest density we may allow, and $\rho_{x,y,z}$ is the linear density of the single atom wave function.

For a BEC to be in quasi-1D regime frequencies of transverse confinement have to be much larger than the chemical potential and the wave function in the directions of tight confinement can be written as the ground state of a

harmonic oscillator

$$\psi_{y,z} = \left(\frac{m\omega_\perp}{\pi\hbar}\right)^{1/4} e^{-\frac{\sqrt{\frac{m\omega_\perp}{\pi\hbar}}x^2}{2}}. \tag{3.2}$$

In order to make a conservative estimate, we take the largest value of the wave function to obtain linear densities

$$\rho_{y,z} = \sqrt{\frac{m\omega_{y,z}}{\pi\hbar}}. \tag{3.3}$$

At the same time, confinement in the third direction is very weak, so that wave function in that direction is given by the Thomas-Fermi approximation

$$\rho_x = \frac{1}{g_{1\mathrm{D}}N}(\mu - V(x)), \tag{3.4}$$

and the maximum linear density in that direction is estimated as

$$\rho_x = \frac{\mu}{g_{1\mathrm{D}}N} \tag{3.5}$$

here $g_{1\mathrm{D}} = 2a_s\hbar\omega_\perp$ is the effective nonlinear coefficient in 1D Gross-Pitaevskii (GP) equation [12].

The chemical potential, μ, is related to number of atoms, N, and the trap frequency of weak confinement. From the condition for the Thomas-Fermi size of the BEC $\mu - V(x) = 0$ we find that its half length is

$$R = \sqrt{\frac{2\mu}{m\omega^2}}. \tag{3.6}$$

On the other hand, the wave function must be normalized to unity

$$\frac{1}{g_{1\mathrm{D}}N}\int_{-R}^{R}\left(\mu - \frac{m\omega^2x^2}{2}\right)dx = 1. \tag{3.7}$$

Combining last two expressions we eliminate the half length and obtain an expression for the chemical potential in terms of the weak trapping frequency, ω, number of atoms, N, and nonlinear coefficient in 1D GP equation, $g_{1\mathrm{D}}$. This is given by

$$\mu = \left(\frac{9}{32} m\omega^2 g_{1\mathrm{D}}^2 N^2\right)^{1/3}. \tag{3.8}$$

Ultimately, we obtain an expression for the maximum number of atoms in the cloud in terms of the parameters of the problem, given by

$$N < \frac{8}{3}\pi^{3/2} \frac{\rho_{\mathrm{crit}}^{3/2} a_s^{1/2} \hbar^2}{m^2 \omega \omega_\perp}. \tag{3.9}$$

The typical critical density for alkali atoms when the life-time becomes smaller than a second is of order $\rho_{\mathrm{crit}} = 10^{14}$ cm^{-3}. Taking for estimation $a_s = 100a_0$, a_0 is the Bohr radius, and frequencies $\omega = 3\ 2\pi \cdot \mathrm{Hz}$, $\omega_\perp = 50\ 2\pi \cdot \mathrm{kHz}$, we obtain the result which indicates that the number of atoms in the trap cannot be larger than order of 100. Both frequencies that we took are pushing the practical limits which may be obtained with dipole optical traps [41, 42].

3.1.2 Adiabatic energy levels

In this chapter, we use units such that $\hbar = 1$, $M_{\mathrm{atom}} = 1$ and unit of length is $L_u = 1\mu m$. The energy and time units are therefore given by

$$\begin{gathered} E_u = 118.3\ h \cdot \mathrm{Hz} = 5.68\ k_B \cdot\ \mathrm{nK}, \\ t_u = 1.346\ \mathrm{ms}. \end{gathered} \tag{3.10}$$

We consider a two mode system: an atom may be described either by the BEC wave function ψ_B or by the wave function in the dot ψ_d that are

given by equations

$$\left[-\frac{1}{2}\nabla^2 + V_t(x)\right]\psi_B(x) + g_{1\mathrm{D}}\left|\psi_B(x)\right|^2\psi_B(x) = \mu\psi_B(x), \tag{3.11}$$

and

$$\left[-\frac{1}{2}\nabla^2 + V_d(x)\right]\psi_d(x) = \epsilon_d\psi_d(x). \tag{3.12}$$

The total potential is $V(x) = V_t(x) + V_d(x)$. For this approximation to be valid the size of the dot potential has to be much smaller than the size of the BEC and the metastable ground state in the dot is almost decoupled from the smoothly varying trap potential. We also require that only this state is relevant, that is, the dot is tightly focused so that separation between the levels inside of it is larger than the thermal energy k_BT.

The many-body state may be approximated by the expansion in terms of linear combinations of these two wave functions. As a result, the position-dependent destruction operator is

$$\hat{\Psi}(x) = \phi_B(x)\hat{a}_B + \psi_d(x)\hat{a}_d \tag{3.13}$$

where $\hat{a}_d^\dagger$ creates a particle in the dot and $\hat{a}_B^\dagger$ creates a particle in the modified condensate wave function orthogonal to $\psi_d(x)$ defined as

$$\begin{array}{l}\phi_B(x) = \frac{\psi_B(x) - \alpha\psi_d(x)}{\sqrt{1-\alpha^2}}, \\ \alpha = \int dx\psi_d(x)\psi_B(x).\end{array} \tag{3.14}$$

Notice that without loss of generality, we consider the wave functions to be real valued. The Hamiltonian of the system may be written in the basis of Fock states inside of the dot $|n\rangle$. In this case there are $N - n$ atoms in the BEC.

We consider the situation with $N \gg n$. The non-vanishing matrix elements of the system Hamiltonian when interaction energy in the dot is comparable to the binding energy are (for details see [44])

$$\begin{array}{c} \langle n| H |n\rangle = nE_1 + \frac{n(n-1)}{2}\nu, \\ \langle n+1| H |n\rangle = \langle n| H |n+1\rangle = \sqrt{n+1}\Delta(n), \\ \langle n+2| H |n\rangle = \langle n| H |n+2\rangle = \sqrt{(n+1)(n+2)}A, \end{array} \tag{3.15}$$

here ν is the interaction energy of two atoms inside of the dot, and ϵ_d is the depth of the ground state in the dot. The coefficients E, ν, Δ, and A are given by the following expressions

$$\begin{array}{c} E_1 \approx \epsilon_d - \mu + V(r_d) + 2g_{1\mathrm{D}}NJ_2, \\ \nu = g_{1\mathrm{D}}(J_0 - 4J_2 + J_4) \approx g_{1\mathrm{D}}J_4, \\ \Delta(n) = \Delta_0 + n\Gamma, \\ \Delta_0 = \sqrt{N^3}g_{1\mathrm{D}}J_1, \\ \Gamma = g_{1\mathrm{D}}\sqrt{N}J_3, \\ A = \frac{1}{2}g_{1\mathrm{D}}NJ_2, \end{array} \tag{3.16}$$

with overlap integrals J_n defined as

$$J_n = \int dr[\phi_B(r)]^{4-n}[\psi_d(r)]^n. \tag{3.17}$$

Below, the BEC and the dot wave functions are calculated with imaginary time method [46].

The adiabatic energy levels, *i.e.* levels for a fixed position of the dot are shown in Fig.3.1(b). The energy levels for large separation between the dot and the BEC correspond to Fock states inside of the dot since there is no overlap between the BEC and the dot wave functions, hence the Fock states in the dot is the good basis. The avoided level crossing are due to overlap between the BEC and the dot wave functions, the smaller the overlap the smaller the

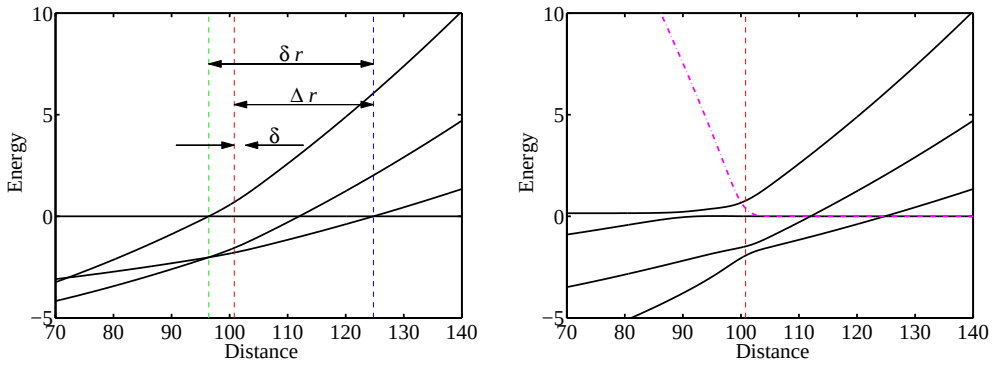

Figure 3.1: (a) Diagonal terms of the Hamiltonian (no coupling). Verticals dashed lines show (from left to right): $1 \rightarrow 2$ atoms level crossing, BEC boundary, and $0 \rightarrow 1$ atoms level crossing. Characteristic lengths are shown to scale. (b) Energy levels of the two mode system (with the coupling present). Dashed-dotted line shows profile of the BEC in arbitrary units.

gap. The idea of the quantum tweezer operation relies on the fact that for a certain extraction rate all the avoided crossings are passed adiabatically except the last one, which is passed non-adiabatically, so that the system stays in the level that corresponds to a single atom inside of the dot for large separations. Depth of the dot cannot be chosen arbitrary, since it is important that only the last level crossing happens outside of the BEC — this is controlled by the depth of the dot potential as we discuss below.

3.1.3 Depth of the dot and length scales of the problem

Effective operation of the tweezer in the dragging regime relies on correct relationship between three length scales. These are δ, width of the surface structure of the BEC; δr, separation of the last two level crossings; and Δr,

distance from the edge of the BEC to the last level crossing (see Fig. 3.1(a)). These lengths scales are approximately given by

$$\begin{aligned} \delta &= \left(\frac{1}{2\omega^2 R}\right)^{1/3}, \\ \delta r &= \frac{\nu}{V'(x)|_{x=R}} = \frac{\nu}{\omega^2 R}, \\ \Delta r &= \frac{|\varepsilon_d|}{V'(x)|_{x=R}} = \frac{|\varepsilon_d|}{\omega^2 R}, \end{aligned} \tag{3.18}$$

here ν is interaction energy of two atoms inside of the dot, and ϵ_d is the depth of the ground state in the dot. For effective operation of the tweezer applied to single atom extraction, the width of the surface of the BEC must be smaller than separation between the last two level crossings, and the second to last crossing must be inside of the BEC to allow strong coupling between the BEC and the dot wave functions, while the last level crossing must happen outside of the BEC. Hence the conditions

$$\begin{aligned} \delta &< \delta r, \\ \Delta r &< \delta r. \end{aligned} \tag{3.19}$$

From the second inequality we get the condition on the depth of the dot potential

$$|\epsilon_d| < \nu. \tag{3.20}$$

In case of the Gaussian dot well for large depths, the potential may be approximated by a harmonic oscillator as in

$$V(x) = -V_0 \exp\left(-\frac{x^2}{2\sigma^2}\right) \approx -V_0 + \frac{V_0 x^2}{2\sigma^2} = -V_0 + \frac{\omega_{\text{eff}}^2}{2} x^2 \tag{3.21}$$

with effective trapping frequency

$$\omega_{\text{eff}} = \sqrt{\frac{V_0}{\sigma^2}}. \tag{3.22}$$

The depth of the energy level is given by

$$\varepsilon_d = -V_0 + \frac{1}{2}\omega_{\text{eff}} = -V_0 + \frac{1}{2}\sqrt{\frac{V_0}{\sigma^2}}. \tag{3.23}$$

Interaction of the two atoms in the dot could be estimated from the harmonic oscillator wave function

$$\nu \approx g_{1\text{D}} \int |\psi_d|^4 \, dx = \frac{g_{1D}}{\sqrt{2\pi}} \left(\frac{V_0}{\sigma^2}\right)^{1/4}, \tag{3.24}$$

The maximum allowed depth of the dot potential may be estimated either from a numerical solution of the nonlinear equation

$$\varepsilon_d = \nu, \tag{3.25}$$

or conservatively as

$$\begin{aligned} V_0 &= \tfrac{g_{1D}}{\sqrt{2\pi}} \left(\tfrac{V_0}{\sigma^2}\right)^{1/4} \\ V_{0,c} &= \left(\tfrac{g^4}{4\pi^2\sigma^2}\right)^{1/3}. \end{aligned} \tag{3.26}$$

In the Fig. 3.2(a), we show energy of the ground state of the potential, and interaction energy, calculated numerically for the Gaussian potential, and analytically from the harmonic well approximation.

We see that for $V_0 < 3$ the conditions of Eq. (3.19) are satisfied. We choose the following parameters for the calculation

$$V_0 = 2.5, \quad g_{1\text{D}} = 4.55, \quad N = 100, \quad \omega = 0.0258, \tag{3.27}$$

here the nonlinear coefficient, $g_{1\text{D}}$, and number of atoms, N, are obtained from the parameters in previous section. The frequency ω is for 3 $2\pi \cdot$ Hz is also as

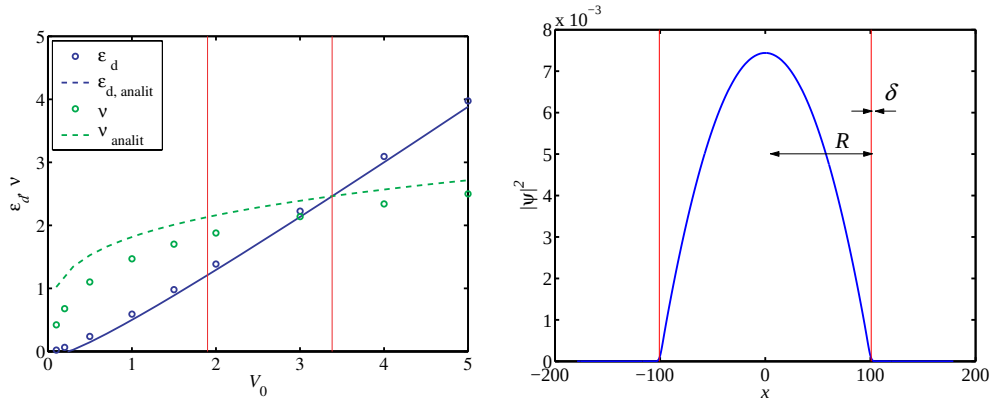

(a) (b)

Figure 3.2: (a) The depth of the bound state in the dot and interaction energy of two atoms in the dot. Dashed line – ν, energy of two atom interaction in the dot, solid line - ε_d, depth of the lowest energy level in the dot. Circles are for the values calculated numerically for the Gaussian potential with $\sigma = 1$, the lines are for estimated with harmonic well approximation. Vertical lines show estimation for the maximum depths of the dots for effective 1 atom tweezing - conservative and from solving nonlinear equation. From numerical values it is clear that for $V_0 < 3$ the condition in Eq. 3.19 should be fulfilled. (b) The BEC wave function calculated numerically for the parameters mentioned in the text. Half length, R, and width of the surface, δ, are shown to scale.

in previous section. From this parameters we numerically calculate the depth of the ground state in the dot and the length scales.

$$\begin{aligned} \varepsilon_d &= -1.8, \quad R = 100.8 \\ \delta &= \left(\tfrac{1}{2\omega^2 R}\right)^{1/3} = 1.95, \\ \delta r &= \tfrac{\nu}{\omega^2 R} = 30.1, \\ \Delta r &= \tfrac{|\varepsilon_d|}{\omega^2 R} = 26.8. \end{aligned} \tag{3.28}$$

As we see in Fig. 3.1 this length scales are in good agreement with numerical simulations. The BEC wave function is calculated with imaginary time evolution [46]. For parameters mentioned above it is shown in Fig. 3.2(b). Chemical

potential and half-length of the cloud agree very well with analytic formulas in Thomas-Fermi regime

$$\begin{aligned} \mu &= \left(\tfrac{9}{32}\omega^2 g^2 N^2\right)^{1/3} = 1.95, \\ R &= \sqrt{\tfrac{2\mu}{\omega^2}} = 100.8. \end{aligned} \tag{3.29}$$

The width of the surface depending on the fit region is $\delta \sim 1$ to 2. The level structure for two mode system is shown in the Fig. 3.1.

3.1.4 Conditions for operation

The probability of tunneling between two quantum states at an avoided crossing depending on a parameter (r in this case) is given by the Landau-Zener formula [47, 48]

$$P_{LZ} = \exp\left(-\frac{\delta^2}{2\left(\frac{d\Delta E}{dr}\right)v}\right), \tag{3.30}$$

where δ is the smallest energy spacing, $\frac{d\Delta E}{dr}$ is relative slope of the energy levels with respect to parameter r, and v is the rate of change of the parameter. This gives the critical rate v_{ad} of change below which the system will stay in the first level

$$v_{ad} = \frac{\delta_{ge}^2}{9.1\frac{d\Delta E_{ge}}{dx}} = 0.34. \tag{3.31}$$

The time to for the dot to travel the half length is

$$t_R = \frac{R}{v_{ad}} = 294 = 395 \text{ ms}. \tag{3.32}$$

This seems to be very reasonable if the lifetime of the BEC is order of a second. The last level crossing is much smaller than the previous ones. Here we cannot

get the level separation at the level crossing with numerical precision, but it is at least two orders of magnitude smaller, so that there must be very wide plateau in rate of change for the operation.

3.2 Raising the dot in the middle

In a further study of the quantum tweezer problem, we have considered raising the dot in the center of the BEC. Such a dot can be created with two blue detuned beams separated by a small distance, producing a M-shaped potential. In this regime one may consider adiabatic levels of the system in dependence of the height of the potential. We have found that even for smaller frequencies of transverse confinement this regime would be more advantageous than when the dot is dragged out from the BEC: the extraction times are much smaller and the developed gaps are larger allowing for larger initial temperature of the system. In this section, we describe this approach briefly,since the main conceptual difference is that instead of changing the position of the dot its depth is changed. We also study the sensitivity of the procedure on fluctuation of various parameters.

3.2.1 Dot potential in the center

As in the another approach, we consider the situation in which the confinement in the transverse direction is much larger than chemical potential of the BEC. In contrast to the previous approach, the dot potential is given by two repulsive regions that may be produced by two blue-detuned tightly

focused beams (see Fig. 3.3(a))

$$V(x) = V_0 \left(e^{-\left(x-\frac{d}{2}\right)^2/2\sigma^2} + e^{-\left(x+\frac{d}{2}\right)^2/2\sigma^2} \right) \approx V_{\text{off}} + \frac{\omega_{\text{eff}}^2 x^2}{2}, \tag{3.33}$$

where d is the separation between the centers of the beams, and $\sigma = w/2$ is half of the Gaussian beam waist at e^{-2} level. The frequency of the confinement in the dot is at a maximum for fixed V_0 when $d = 2\sqrt{3}\sigma$. In this case, the offset of the bottom of the potential, V_{off}, and the effective frequency of the confinement, ω_{eff}, are approximately given by

$$\begin{aligned} \omega_{\text{eff}} &= \tfrac{2}{e^{3/4}\sigma} V_0^{1/2}, \\ V_{\text{off}} &= 2V_0 e^{-3/2}. \end{aligned} \tag{3.34}$$

The position of the dot is stationary in the bulk of the BEC. The extraction of a small number of atoms occurs when the depth V_0 of the well is increased at some rate.

3.2.2 Adiabatic energy levels and extraction

We calculated the adiabatic energy levels with dependence on V_0 based on an approach similar to that which is described in Section 3.1.2. We used a two mode many-body system. The BEC and the dot wave functions are calculated separately (see Fig. 3.3(b)). For the dot, we replace the metastable M-shaped potential with V-shaped potential representing the middle part. As the depth of the dot increases this becomes an increasingly better approximation. The BEC wavefunction is calculated for the full potential that includes both slowly varying trap and repulsive potentials. At the small depths, the

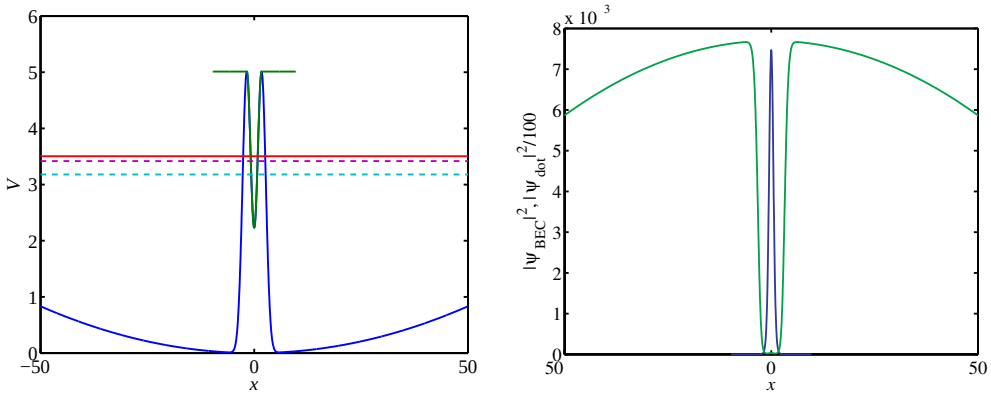

(a) (b)

Figure 3.3: (a) Potentials used in the calculation: M-shaped – BEC potential, V-shaped – dot potential. The solid horizontal line shows the chemical potential, the two dashed lines show one and two particles in the dot energy levels. The height of the dot potential is $V_0 = 5$. (b) The BEC and the dot wave functions, the dot wave function is decreased by two orders of magnitude. For this value of V_0, the overlap nearly vanishes.

tunneling couples the two systems and the state of the system does not correspond to a definite number of atoms in the dot. For infinitely large dot potential the state with n atoms in the dot and $N - n$ atoms in the BEC is the eigenstate of the system.

For this configuration, we have found that even for smaller frequencies of transverse confinement the operation is more robust. Smaller values of transverse confinement frequencies allow for a larger number of atoms in the BEC, this makes the mean-field approximation better. In Fig. 3.4 we show adiabatic levels of the system in dependence of parameter V_0 with frequency of transverse confinement $\omega_\perp = 30\ 2\pi \cdot \mathrm{kHz}$ and a weak confinement of frequency

$\omega = 3\ 2\pi \cdot \mathrm{Hz}$. In this case, performing a similar estimate on maximum number of atoms as in Section 3.1.1, we find that this can be as large as $N = 200$. We proceed with these numbers in the simulation. Notice that in Fig. 3.4, the levels are separated by a larger amount than in the dragging approach in Fig. 3.1.

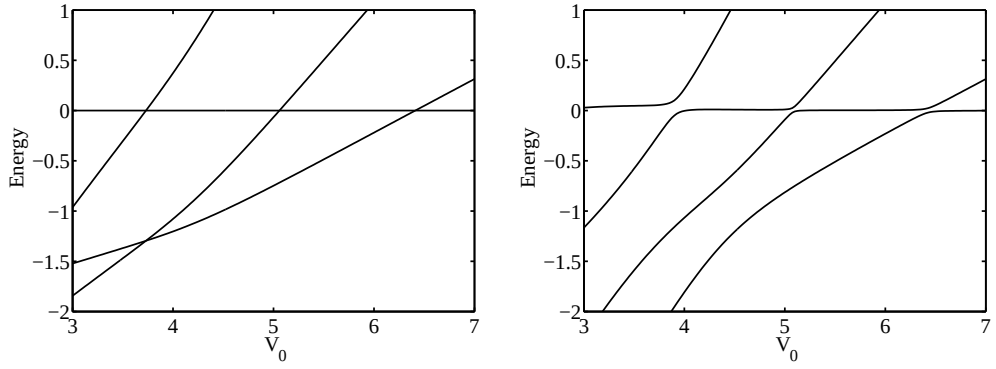

(a) (b)

Figure 3.4: (a) Diagonal terms of the Hamiltonian (no coupling). (b) Energy levels of the two mode system (including coupling).

In Fig. 3.5, we show the results of the solving the dynamical Schrödinger equation described by the two-mode Hamiltonian. We start with such a value for the dot potential such that the BEC wave function overlaps with the dot wave function substantially. Initially we take the system to be in the lowest level. The depth is increased linearly in time until the two system decouple completely. For a range of rates with which the potential is raised all of the levels are crossed adiabatically except the last one and the system ends up in the first excited level with a large probability, which for large depths of

the dot correspond to exactly one particle in the dot and $N-1$ particles in the BEC. The gaps between avoided level crossings are larger than in the dragging approach. This allows shorter duration of the process: order of tens of milliseconds.

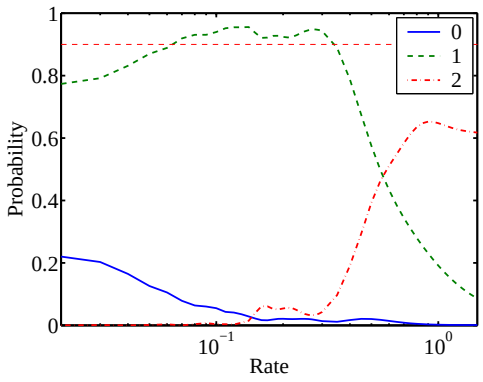

Figure 3.5: Probabilities to extract certain number of atoms when the depth of the dot is changed from $V_0 = 3$ to $V_0 = 7$. Initially the system is in the ground state.

3.2.3 Variations and parameter fluctuations

In the experiments, the number of atoms in the BEC fluctuates from shot to shot [41, 42]. We have investigated how this fluctuation will affect the efficiency of the operation. We have considered a few variations to the procedure described above. We have taken (1) linear ramp of the dot's depth, and also (2) quadratic and (3) exponential ramps. (4) Since in the experimental realization the potential for the BEC may be close to the flat box with infinite walls [41, 42], we have considered that case as well with linear ramp of the dot's depths. In these four cases we have observed how the efficiency of the

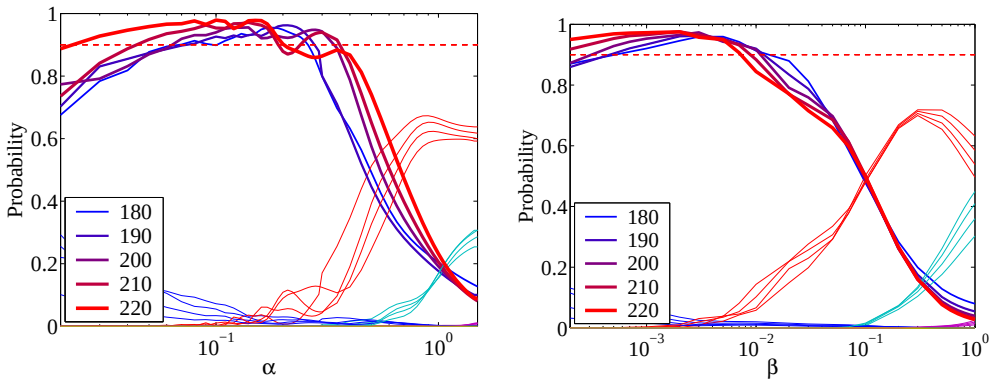

(a) (b)

Figure 3.6: (a) Parabolic trap. Linear ramp. Probability to find a single atom in the trap is shown by thick lines. Thin lines are for extraction of different numbers of atoms. Legend shows number of atoms in the BEC in each case. As number of atoms increases the operation region shifts to slower rates. (b) Same as (a) for quadratic ramp.

operation changes when the number of atoms in the BEC fluctuates around $N = 200$. We also have considered the effect of a small variation of other parameters: (5) a decrease of transverse confinement frequency, (6) a change of the distance between the beams from optimal, and (7) an increase in σ, the width of the beams creating the dot.

For a linear ramp of the potential depth given by $V_0 = V_{\text{init}} + \alpha t$ and the same parameters as mentioned above, we observe that as number of atoms increases a region of operation increases and shifts to slower rates (see Fig. 3.6(a)). We define region of operation as the region of rate parameter α when extraction of a single atom is above 90 percent. As a result if from shot to shot the number of atoms fluctuates by 20 the region would shrink

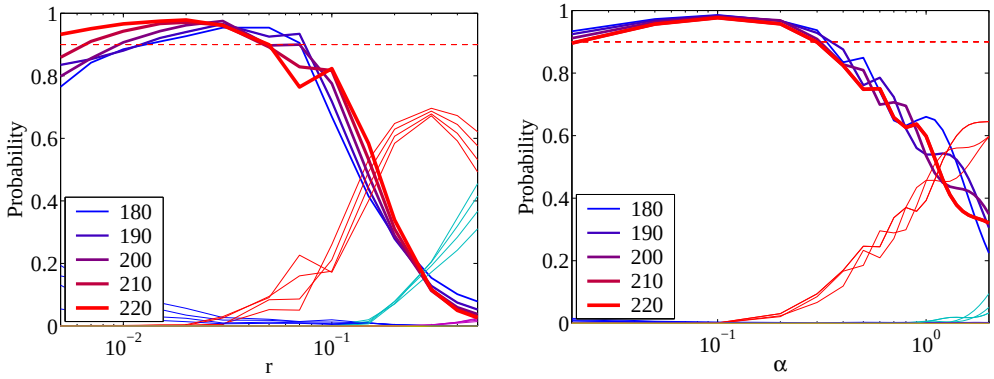

(a) (b)

Figure 3.7: (a) Parabolic trap. Exponential ramp. Probability to find a single atom in the trap is shown by thick lines. Thin lines are for extraction of different numbers of atoms. Legend shows number of atoms in the BEC in each case. As number of atoms increases the operation region shifts to slower rates. (b) Box trap. Linear ramp. Thick lines show probability to extract a single atom from BECs with different number of atoms. As number of atoms increases the operation region shrinks.

from a decade to an octave.

As a possible improvement one may take a quadratic ramp instead of linear one, so that the last level crossing is crossed with larger rate than previous ones. We take the following form for the ramp: $V_0 = V_{\text{init}} + \beta t^2$. In terms of region of operation (in logarithmic scale) for parameter β in comparison to α the improvement is noticeable but not dramatic: the operation region is increased to more than a decade (see Fig. 3.6(b)). Similar trends as in the first case are present: as the number of atoms increases, the region shifts to slower rates and becomes larger.

Finally, we take yet another form of the ramp: $V_0 = V_{\text{init}} e^{rt}$. The

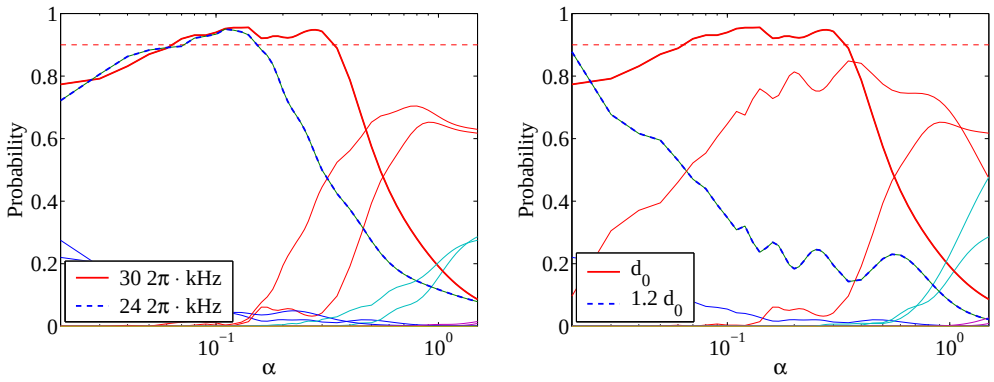

(a) (b)

Figure 3.8: (a) Parabolic trap. Smaller frequency of transverse confinement. Thick lines show probability of extraction of a single atom. Frequency of the transverse confinement is shown in the legend. (b) Parabolic trap. Size of the dot is increased by 20 percent from the optimum. The effectiveness of the operation is reduced a lot. The operation region is shifted to slower rates by more than a decade.

results of the simulation with this ramp are shown in Fig. 3.7(a). The region of operation also increases in comparison to linear ramp.

When the frequency of the transverse confinement decreases the effective interaction strength between the atoms decreases. And since the operation of the quantum tweezer relies on a large interaction between the atoms it would become less effective. This is illustrated in Fig. 3.8(a). As the frequency of the transverse confinement decreases from 30 $2\pi \cdot$kHz to 24 $2\pi \cdot$kHz the operation region shrinks substantially.

It is also important to keep the dot potential optimal, so that the frequency of the confinement is maximal. As d, the separation between the

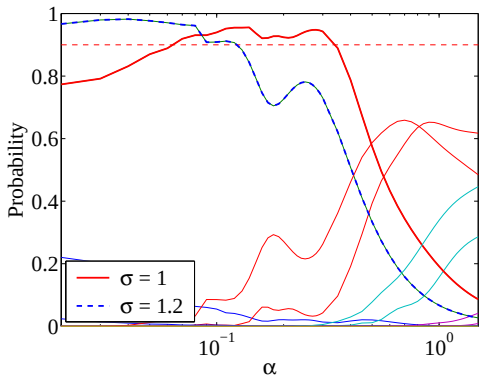

Figure 3.9: Parabolic trap. Width of the beams creating the dot, σ, is increased by 20 percent. Distance between them is optimal in terms of new width. The operation region is shift to slower rates. There are rates when the operation is more efficient.

beams forming the dot, increases by 20 percent the region of operation shifts by more than a decade (see Fig. 3.8(b)).

Finally, in Fig. 3.9, we show the effect of larger σ, spot size of the beams creating the dot. The size of the spot is increased by 20 percent. The operation becomes more efficient, but the operation region shifts to slower rates. The effects of the excited states in the dot, which were ignored in the model, may become more relevant for wider dots.

3.3 Nonlinear atom optics with a small number of atoms and multiparticle interferometry

As one of the possible application of a small number of atoms extracted from a BEC in this section, we consider various nonlinear processes with a

small number of atoms that may combined into multi-particle interferometry scheme, when interferometric effects observed only when observation of all the particles participating in the process is made [16]. In the scheme, we suggest that it is crucial for an atom to be in the ground state of a tightly focused optical trap – this condition would be automatically satisfied for an atom extracted from a BEC with the quantum tweezer.

3.3.1 Quantum entanglement: previous experiments and suggestions

Entanglement is at the root of Bell's theorem, which exposes the differences between quantum theory and a local classical theory based on elements of reality [49]. The predictions of quantum mechanics have been experimentally observed with entangled Einstein-Podolsky-Rosen (EPR) pairs [50–52] as well as Greenberger-Horne-Zeilinger (GHZ) triples [53]. A related consequence of entanglement is the possibility of multiparticle interferometry. Given a maximally entangled system of N-particles (a "Schrödinger cat" state), a measurement of interference between different parts of the wave function corresponding to a single particle yields random results. It is only when performing a coincidence measurement on all N particles that an interference pattern is revealed [54]. Experimental confirmation of this result has been obtained using photonic EPR pairs [52, 55] and internal states of four ions in the same trap [56] but no experiments have been performed using a larger number of particles. The latest generation of experiments with photons rely on parametric down-conversion, which has the technical disadvantage of an exponentially

decreasing number of useful counts as N increases. Although multiparticle entanglement has also been demonstrated using liquid state NMR [57] and trapped ions [56], these systems couple to the environment quite strongly and they decohere on a fast timescale. Given that entanglement is the key ingredient in all quantum computation and quantum communication schemes, clean experimental studies of its consequences have become an active topic of research in the last decade.

In recent years several papers [58–60] have suggested the generation of entanglement between neutral atoms confined in traps by using their interaction in controlled atomic collisions. The atoms are guided in their motion and their evolution yields the required entanglement of internal states. Other schemes to achieve this sort of entanglement starting from BECs have been suggested [61–63].

3.3.2 Nonlinear atom optics processes with a small number of atoms

Here we present two general N-atom nonlinear processes. The first one is used to convert a Mott-insulator-like (MI) state [58] into a state with all particles in the (many-body) ground state of a single trap (BEC-like state); its reverse process converts the BEC state into a MI state. The second process is used to generate a Schrödinger cat state starting from a BEC state by controlling the splitting of the well. As an application of the processes we discuss a scheme for multiparticle interferometry with spatially separated paths.

In the first process, which is also stage I of the interferometry setup, we

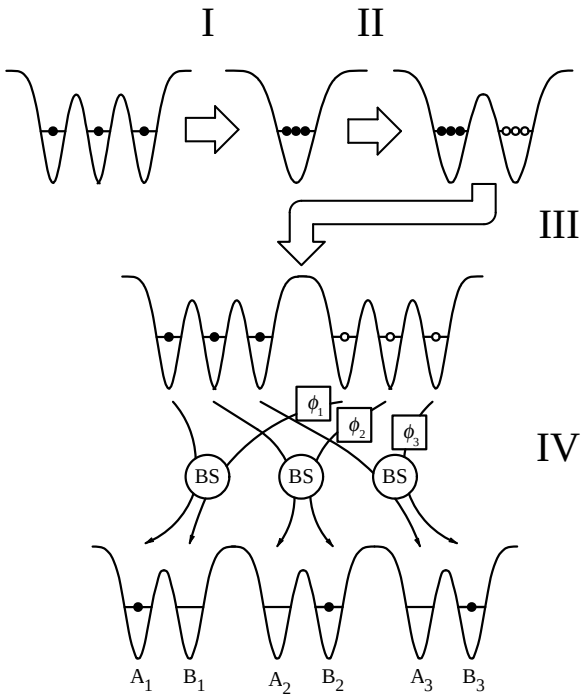

Figure 3.10: Schematics of the multiparticle interferometry procedure. Stage I - creation of N atoms in the ground state of the trap starting with N individual atoms in N traps. Stage II - creation of "Schrödinger cat" state. Stage III - spatial separation of the atoms. Stage IV - applying phases, combining on the beamsplitters and measurement.

start with a collection of N atoms in the ground states of N independent traps (MI state). These separate atoms can be extracted from a reservoir using a quantum tweezer as discussed above. Alternatively, single atoms stored and detected in micro-optical traps (which have been experimentally reported [43, 64] but are in excited states of the trap) can be Raman cooled individually to the ground state. Given that the storage and detection of a small number of atoms in optical dipole traps has been recently reported [43, 64], one could

alternatively Raman cool individually trapped atoms to the ground state.

The BEC state (stage I, Fig. 3.10) is achieved by bringing together the N wells adiabatically if the interaction between atoms is repulsive, as will be shown in detail below. This is a consequence of the quantum adiabatic theorem, since the MI state is the ground state when the wells are far apart. The evolution is then represented by

$$|w_1\, w_2\, \ldots\, w_N\rangle \rightarrow |\Psi_I\rangle = |w\, w\, \ldots\, w\rangle, \tag{3.35}$$

where the states are properly symmetrized bosonic states.

In the second process (stage II of multiparticle interferometry) the interaction is attractive. Switching of the interaction sign in the interferometry process can be done by using a Feshbach resonance [65–67]. Starting from the BEC state, we slowly split the well into two approximately equal microtraps, which we label as L and R. The lowest energy states are then the ones having all atoms in the left or in the right well. Since initially the system is in the ground state, by separating the traps at some slow rate v, when the wells are far apart there exist a linear combination of these two nearly degenerate states, *i.e.* the system is in the Schrödinger cat state

$$|\Psi_I\rangle \rightarrow |\Psi_{II}\rangle = \alpha|LL\ldots L\rangle + \beta e^{i\theta}|RR\ldots R\rangle, \tag{3.36}$$

with α, β, and θ real. For perfectly symmetric traps, $\alpha = \beta$ and $\theta = 0$, but any asymmetry makes these parameters rate dependent, as will be discussed in detail below.

Additional processes are needed to realize multiparticle interferometry. During stage III, the interaction is switched back to repulsive and each of the two traps is separated to N. This stage can be seen as the inverse of stage I applied to the wells L and R. Again, if the separation is done adiabatically the system remains in the ground state which in this case corresponds to a single atom in each one of the wells. The state is now

$$|\Psi_{II}\rangle \rightarrow |\Psi_{III}\rangle = \alpha\,|L_1 L_2 \ldots L_N\rangle + \beta e^{i\theta}\,|R_1 R_2 \ldots R_N\rangle\,. \tag{3.37}$$

Subsequently, the atoms in wells derived from the original R well are subjected to additional phase shifts $\phi_1, \phi_2 \ldots \phi_N$, which can be applied, for example, by adjusting the depth of the wells adiabatically.

In the final stage IV of the scheme, we combine states L_i and R_i in a 50-50 beamsplitter [68]. Notice that in the experiment, only one of these two is occupied, so the interatomic interaction plays no role in this stage.

3.3.3 The signature of multi-particle interferometry

We denote the outputs of each beamsplitter by A_i and B_i and assign a value of $+1$ to the measurement of an atom in channel A_i, and -1 to the measurement of atom in channel B_i. The probability, $P(+1)$, that the product of all measurements gives $+1$ (for instance $A_1 B_2 B_3$ in the case of three atoms) is $\left(1 - \alpha\beta\cos\left(\Delta + \theta\right)\right)/2$, where $\Delta = \sum_{i=1}^{N} \phi_i$. The probability for the product to be -1 is $P(-1) = 1 - P(+1)$, hence the expectation value over a large number of measurements is $-\alpha\beta\cos\left(\Delta + \theta\right)$. We would like to stress that a

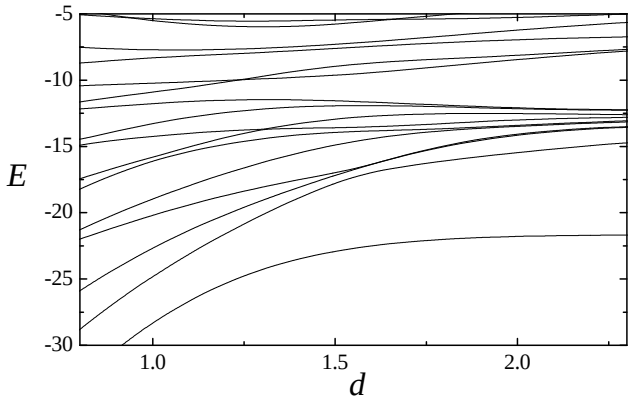

Figure 3.11: Stage I: adiabatic energy levels for three atoms in three wells with repulsive interaction as a function of d. The other parameters of the potential are $V_0 = 10$, $\sigma = 0.5$, $U_0 = 10$, $q_3 = -q_1 = 10^{-4}$, $q_2 = 0$.

correlated measurement of less that N atoms does not show any dependence on phase and appears random.

3.3.4 Model

A number of experimental techniques under development, such as magnetic microtraps [69, 70], hollow optical fiber atom guides [71–73], and optical microtraps [74], allow the kind of atom manipulations discussed here. Feshbach resonances in ultracold atomic collisions [65–67] or the fact that the scattering length for alkali atoms depends on the internal state may be used to modify the effective interaction between atoms, even to convert it from repulsive to attractive.

In order to obtain the relevant parameters for the operation of the interferometer, we study the evolution of an N particle system using optical

microtraps. As an example, we numerically solve the Schrödinger equation in the case of three atoms in a quasi-1D configuration. As for the quantum tweezer this is achieved by strongly trapping the atoms in the perpendicular dimensions, effectively freezing these degrees of freedom. We scale the equations choosing units of length $L_u = 2\ \mu$m, of energy $E_u = \hbar^2/(2M_u L_u^2)$ and of time $t_u = \hbar/E_u$ in this section. The particle interaction is represented by a delta-function potential

$$U(x_1, x_2) = U_0 \delta(x_1 - x_2). \tag{3.38}$$

The atoms are also subject to external potentials due to the optical traps, which in each stage are

$$\begin{aligned} V_{\mathrm{I,III}}(x, d) &= \sum_{i=1}^{3} (1 + q_i) V(x, (i-2)d), \\ V_{\mathrm{II}}(x, d) &= \sum_{i=1}^{2} (1 + q_i) V(x, (i-3/2)d), \end{aligned} \tag{3.39}$$

with

$$V(x, d) = -V_0 \exp\left(-\frac{(x+d)^2}{2\sigma^2} \right). \tag{3.40}$$

The q_i parametrize the asymmetry between the intensities of the beams defining the different wells; we assume that these are 10^{-4}.

3.3.5 Discussion

Let us consider first the evolution during the first and the third stages of the operation. There are four different energy scales in the problem. The first one is the energy difference between the energy levels localized in different

wells, which we can estimate as $E_{\rm asym} \approx qV_0$. The second is the energy required to move one of the atoms to an already occupied well, estimated to be $E_{\rm int} \approx U_0/\sigma_0$ where $\sigma_0 = (V_0/\sigma^2)^{1/4}$ is the width of the wave function in a well. The third scale is the energy $E_{\rm exc} \approx \sigma_0^{-2}$ required to put one of the atoms in an excited state of one of the traps. The last energy scale ($E_D \approx (\pi/ND)^2$) is the energy required to excite the atoms out of the ground state when the distance between the wells is $D \approx 2\sigma$, at which time the trap can be approximated by a square well of width ND. We consider operation in the regime in which

$$E_{\rm asym} \ll E_{\rm int},\, E_{\rm exc},\, E_D. \tag{3.41}$$

Fig. 3.11 shows the dependence of the adiabatic levels on the separation d during this stage. The presence of the small asymmetry in this stage does not affect the nature of the ground state, which is non-degenerate. Joining or separating the wells at a slow speed keeps the system in the ground state, *i.e.* the lowest curve in the figure. We can estimate the rate at which the adiabaticity is lost by applying the Landau-Zener formula [47, 48], $v_{\rm ad} \approx (\Delta E_{\rm gap})^2/(dE/dx)$. The slope can be estimated as $\sqrt{NV_0}/\sigma^2$. The size of the gap depends on which of the three large energy scales in (3.41) is the smallest. In the example that we are presenting, all three are roughly the same order of magnitude. The probabilities $|a_i|^2 = |\langle\psi_i|\psi\rangle|^2$ to find the system in the states $|\psi_i\rangle$ at the end of the evolution is plotted in Fig. 3.12 as a function of the speed v. In our example, the critical rate is $v_{cI,2} = 0.35$; the probability to find the system in other states is less than 0.01. For multiparticle interferometry, it is critical not to accumulate an additional phase during the third process due to the

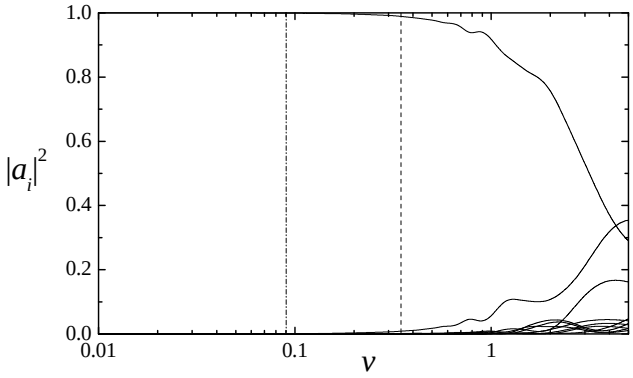

Figure 3.12: Stage III: probabilities to find the system in the adiabatic states after a single well with three atoms is split into three wells with an atom per well ($d_{\text{final}} = 3.0$) as a function of the speed v. The energy levels are the ones shown in Fig. 3.11. For velocities smaller than denoted with dashed line probability to state in the ground state is larger then 0.99, for velocities larger than denoted with dashed-dotted line dephasing is less then 0.1. For stage I the dynamics are very similar except there is no limit on how slow the process could be done.

asymmetry between the right and left set of wells. This gives rise to a lower bound for the allowed velocity, as explained below. For the parameters chosen in the figure this is $v_{cI,1} = 0.09$.

Between these stages and stage I, we need to change the sign of the effective interaction between the particles. For the cases which we are considering, the particles remain in the ground state with very high probability (of the order of 99%) even if this change is performed suddenly.

During stage II, the adiabatic energy levels as a function of d are shown in Fig. 3.13. Once again, we have four energy scales, which can be approximated by $E_{\text{asym}} \approx NqV_0$, $E_{\text{int}} \approx (N-1)|U_0|/\sigma_0$, $E_{\text{exc}} \approx \sigma_0^{-2}$, and

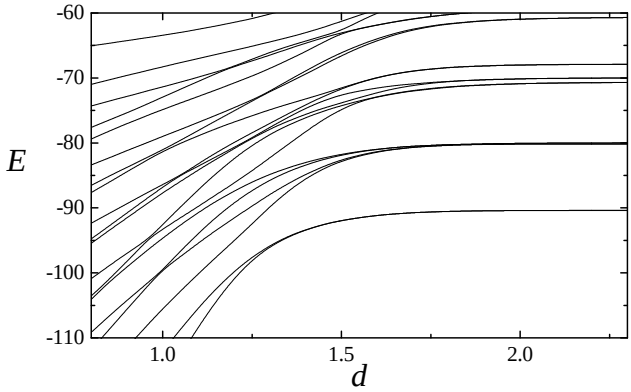

Figure 3.13: Stage II: adiabatic levels of three atoms in two wells in the case of attractive interaction for different values of the separation d . The other parameters of the potential are $V_0 = 30$, $\sigma = 0.5$, $U_0 = -4$, $q_1 = 0$, $q_2 = 10^{-4}$.

$E_D \approx (\pi/2D)^2$. We work in the regime in which (3.41) is valid. Separating the wells adiabatically maintains the system in the ground state, which corresponds to all N atoms being in the lowest of the two wells, which is not the desired state. In order to mix the lowest two energy states we need to evolve the system non-adiabatically with respect to the lowest gap but at a slow enough speed to remain adiabatic with respect to the larger gap. Below $v_{cII,2} = 0.27$ the probability to tunnel to these excited states is less then 0.01 and entanglement is obtained with $\alpha\beta = 0.99$ or larger. On the other hand, the asymmetry yields a dephasing between the two parts of the wave function $\theta = E_{\rm asym} t_{\rm sep}$, where the separation time is inversely proportional to the velocity v. Allowing a maximum dephasing $\phi_{\rm max}$, we must go faster than $v_{cI,1} \approx q V_{0,III} N/\phi_{\rm max}$. This calculation assumes, however, that the asymmetry is constant. In a practical situation, q is driven by fluctuations in the laser

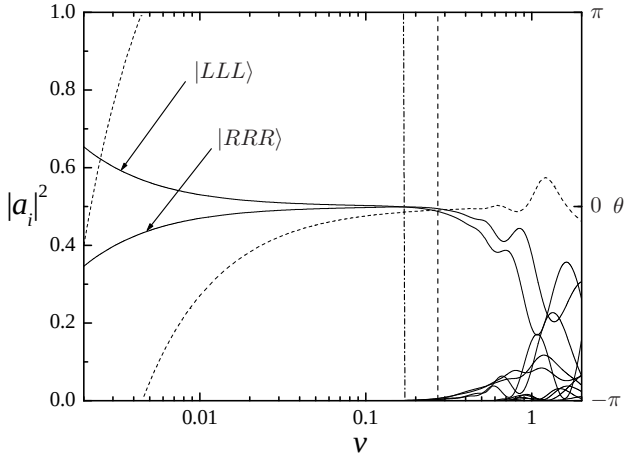

Figure 3.14: Stage II: full lines are probabilities to find the system in the adiabatic states after the separation of one well with three atoms to two ($d_{\text{final}} = 3.0$) as a function of the speed v. The dashed line is θ. The interaction is attractive and the parameters are the ones used in Fig. 3.13. For velocities in the interval between vertical lines the desired state is prepared with probability of 0.99 and dephasing smaller than 0.1.

power, and consequently the phase θ grows diffusively, as the square root of t_{sep} instead of linearly, making the condition less restrictive.

The only two conditions for the applicability of the method are related to the asymmetry of the potential. As long as condition (3.41) is met and as long as $v_{c,2}$ is larger than $v_{c,1}$, there is a range of velocities for which the operation is possible. The critical velocities have a different dependence on N, so for fixed values of the parameters defining the potential and the interaction, there is a maximum number of atoms for which this happens. However, by choosing a different set of parameters this condition can be relaxed. In particular, the strong N^{-2} dependence of the preparation of the MI state can be overcome

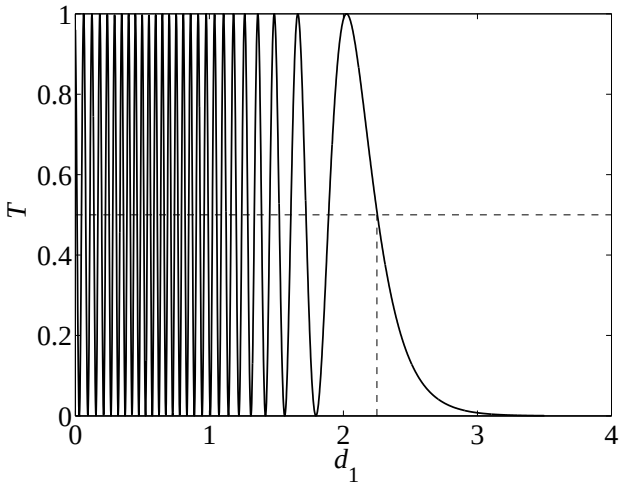

Figure 3.15: Tunneling probabilities for a beamsplitter described by Eq. 3.42 ($\tau = 10$, $V_0 = -15$, $d_2 = 5$). It is advantageous to work at largest distance, providing a wavepacket splitting distance $d_{\text{opt}} = 2.25$.

by separating the atoms in series instead of doing it parallel (for $N = 2^n$, we can think of n steps in which each well is split into two).

The sign of the interaction is changed when all the particles are in the same well. As long as equation (3.41) holds, the system remains in the ground state with very high probability (around 99% in our example) even if the change is done suddenly . A single particle 50-50 beamsplitter does not rely on atom-atom interaction and may be implemented by bringing two wells to some finite distance for a given time [68]. Transmission probabilities for a beamsplitter in which the parameter d changes in the form

$$d(t) = d_2 - \frac{d_2 - d_1}{\cosh(t/\tau)} \tag{3.42}$$

are shown on the Fig. 3.15.

3.3.6 Experimental parameters

Finally, numerical values for realistic experimental parameters are given. In the model described above, the effective interaction between atoms is determined by the scattering length a and the strength of the confinement in the transverse direction. The frequency $\omega_\perp$ of the confinement in the case in which the system stays in the ground state of transverse motion may be expressed in terms of the dimensionless interaction parameter U_0 used above [58] as

$$\omega_\perp = \frac{U_0 \hbar}{4\,|a|\,M_u L_u}. \tag{3.43}$$

Hence it is desirable to use atoms with the largest product of mass and scattering length possible. In Table 3.1 we present the rescaled values used in the calculation for two workhorses of cold atom experiments, sodium and rubidium. The magnetic fields needed to observe Feshbach resonances in alkali atoms are typically hundreds of gauss [65–67]. In the proposed scheme for multiparticle interferometry one should work on the side of the resonance where the scattering length changes sign to avoid the losses associated with crossing the resonance.

Table 3.1: Parameters of the numerical estimates in dimensional units. For the estimates we take scattering lengths of ^{23}Na $a_t = 65a_0$ and ^{87}Rb $a_t = 106a_0$ in triplet states with no magnetic field with a_0 being the Bohr radius [75]; we assume that near a Feshbach resonance the values will be of the same order of magnitude.

Parameter	Na	Rb	Units
$\omega_\perp$	79.9	13.0	2π kHz
$v_{cI,1}$	62.2	16.5	μm/s
$v_{cI,2}$	242	64.0	μm/s
$v_{cII,1}$	117	31.1	μm/s
$v_{cII,2}$	186	49.4	μm/s
$V_{0,II}$	2.47	0.665	$h\times$kHz
d_{opt}	5.16	5.16	μm

Chapter 4

Optical Lattices

4.1 Berry phase effects in asymmetric optical lattices

4.1.1 Semiclassical equation of motion and Bloch theorem

The semiclassical equations of motion are a cornerstone in the theory of charge transport in metals and semiconductors [76]. They relate the group velocity of the electrons to the local band curvature and the change in the lattice momentum to external forces. The standard form of the equations found in textbooks until recently is

$$\dot{\mathbf{r}}_c = \frac{1}{\hbar}\frac{\partial E(\mathbf{k}_c)}{\partial \mathbf{k}_c}, \tag{4.1}$$

$$\hbar\dot{\mathbf{k}}_c = \mathbf{F} + \mathbf{2m\dot{r}_c} \times \omega(\mathbf{r_c}). \tag{4.2}$$

As we have discussed earlier, the Coriolis force term in the second equation that arises in a rotating reference frame is equivalent to a magnetic field $B_{\text{eff}} = 2m\omega/e$ for electrons.

For semiclassical equations of motion to be correct, a particle wave packet must have a size much larger than a unit cell of the lattice. In this case it is localized in the momentum space to a size much smaller than the Brillouin zone (BZ) . The wave packet can be represented as a superposition

$$|\Psi\rangle = \int_{BZ} d\mathbf{k}\, f(\mathbf{k})\, |\Psi_{\mathbf{k}}\rangle \tag{4.3}$$

of the eigenstates of the Hamiltonian in the absence of external force $\mathbf{F}$:

$$\hat{H}_0 \left|\Psi_{\mathbf{k}}\right\rangle = E_{\mathbf{k}} \left|\Psi_{\mathbf{k}}\right\rangle . \tag{4.4}$$

The envelope function is centered around $\mathbf{k}_c$ and the center of the wave packet in space is

$$\mathbf{x}_c = \left\langle\Psi\right| \mathbf{x} \left|\Psi\right\rangle . \tag{4.5}$$

Stationary eigenstates of the Schrödinger equation in a periodic potential satisfy Bloch theorem: they are plane waves $e^{\mathbf{kr}}$ modulated by a function $u_{\mathbf{k}}(\mathbf{r})$ called a Bloch state that has a periodicity of the potential. This may be written as

$$\left|\Psi_{n,\mathbf{k}}\right\rangle = e^{\mathbf{kr}} \left|u_{n,\mathbf{k}}(\mathbf{r})\right\rangle . \tag{4.6}$$

In the last expression, for generality, we leave the band index n, even though in the future discussions we will be mostly concerned with dynamics within a single band and omit the index. An important condition for the semiclassical approach to be correct is that force must be small so that tunneling between bands does not happen and the dynamics is restricted to a single band. We will discuss this criteria quantitatively in the following sections. By substituting the last expression into the Schrödinger equation we can obtain the eigenvalue equation for the Bloch states:

$$H_0 \left|u_{\mathbf{k}}\right\rangle = \left[\frac{1}{2m}(\mathbf{p} + \hbar\mathbf{k})^2 + V_{\text{latt}}(\mathbf{r})\right] \left|u_{\mathbf{k}}\right\rangle = E_{\mathbf{k}} \left|u_{\mathbf{k}}\right\rangle . \tag{4.7}$$

4.1.2 Berry curvature and self-rotation

Very recently, it has been shown that the semiclassical equations of motion need to be modified to include corrections due to geometrical (Berry) phase [77–79]. The equations become

$$\dot{\mathbf{r}}_c = \frac{1}{\hbar}\frac{\partial E_S(\mathbf{k}_c)}{\partial \mathbf{k}_c} - \dot{\mathbf{k}}_c \times \mathbf{\Omega}(\mathbf{k}_c), \tag{4.8}$$

$$\hbar\dot{\mathbf{k}}_c = \mathbf{F} + 2m\dot{\mathbf{r}}_c \times \omega(\mathbf{r}_c). \tag{4.9}$$

The first major difference is the presence of the Berry curvature $\mathbf{\Omega}$. It is a symmetric analog of angular velocity ω (or magnetic field in case of electrons) if we exchange the $\mathbf{r}_c$ and $\mathbf{k}_c$ variables. The second correction is to the band energy, which must contain a term proportional to the self-induced angular momentum (self-magnetization) $\mathbf{S}$. This term is proportional to the angular momentum of the wave packet with respect to its center

$$E_S(\mathbf{k}_c) = E(\mathbf{k}_c) + \mathbf{S}(\mathbf{k}_c) \cdot \omega(\mathbf{r}_c) \tag{4.10}$$

$$\mathbf{S} = \int d\mathbf{r}\,(\mathbf{r} - \mathbf{r}_c) \times \mathbf{J}(\mathbf{r}), \tag{4.11}$$

where $\mathbf{J}(\mathbf{r})$ is the current density [77] given by

$$\mathbf{J}(\mathbf{r}) = \frac{i\hbar}{2m}\left(\psi\nabla\psi^* - \psi^*\nabla\psi\right). \tag{4.12}$$

Both the Berry curvature and the self-induced angular momentum depend on a position of the wave packet in the momentum space $\mathbf{k}_c$ and are readily calculatable from the Bloch states of the stationary problem

$$\mathbf{\Omega}\left(\mathbf{k}_c\right) = i\left\langle \frac{\partial u}{\partial \mathbf{k}_c}\right| \times \left|\frac{\partial u}{\partial \mathbf{k}_c}\right\rangle, \tag{4.13}$$

$$\mathbf{S}\left(\mathbf{k}_c\right) = i\frac{m}{\hbar}\left\langle \frac{\partial u}{\partial \mathbf{k}_c}\right| \times \left(H_0\left(\mathbf{k}_c\right) - E\left(\mathbf{k}_c\right)\right)\left|\frac{\partial u}{\partial \mathbf{k}_c}\right\rangle. \tag{4.14}$$

The Berry curvature can be nonzero only for complex $u(\mathbf{r})$. As long as the semiclassical approximation holds, this result is independent of the distribution $f(\mathbf{k})$ used, and hence of the width of the wave packet in real space. In particular it is independent of time for a fixed value of $\mathbf{k}_c$, that is, the wave packet maintains a constant angular momentum as it spreads on the lattice.

In many circumstances these corrections to the semiclassical equations of motion do not need to be taken into consideration because of constraints imposed on them by the symmetry of the Hamiltonian. If the system possesses time-reversal symmetry, then both vectors $\mathbf{\Omega}$ and $\mathbf{S}$ are odd functions of $\mathbf{k}_c$. On the other hand, if it possesses inversion symmetry then they are even functions of $\mathbf{k}_c$. This implies that in systems with both symmetries they vanish throughout the Brillouin zone.

The semiclassical equations of motion in (4.8), (4.9) have been successfully applied to the quantum Hall effect in magnetic sub-bands [77, 78] and to the anomalous Hall effect in ferromagnets [80–82]. Sundaram [79] has considered a tight-binding model of two-dimensional asymmetric honeycomb lattice. It has clearly illustrated some physical consequences of the corrections to semiclassical equations. This model can be used as a starting point for first-principle calculations similar to [82] applied to thin films of semiconductors such as InSb that are grown on GaAs (100) surfaces [83] or allotropic forms of BC_2N [84]. We discuss how this model can be realized almost ideally with ultracold atoms in optical lattices below. In what follows, we first present some analytical results from the tight-binding model and then discuss the results of

the numerical calculations in continuous potentials.

4.1.3 Tight-binding honeycomb lattice

For a periodic potential it is possible to define a basis of Wannier function [85]. These are orthogonal functions centered at each lattice site (position $\mathbf{R}$) and associated with a band n. They may be written as

$$|w_n(\mathbf{R})\rangle = \frac{1}{\sqrt{N}} \sum_{\mathbf{k}} e^{-i\mathbf{k}\mathbf{R}} |\Psi_{n,\mathbf{k}}\rangle . \tag{4.15}$$

Since the Wannier function from different bands are orthogonal, they provide convenient basis for expansion of the Hamiltonian especially when the potential is sufficiently deep so that the Wannier functions decay exponentially. Quite often the dynamics may be limited to a single band and the Hamiltonian can be written as

$$\hat{H} = \sum_{\mathbf{R}\mathbf{R}'} |w(\mathbf{R}')\rangle \langle w(\mathbf{R}')| \hat{H} |w(\mathbf{R})\rangle \langle w(\mathbf{R})| . \tag{4.16}$$

As the depth of the lattice increases, neighboring Wannier functions overlap less and only nearest between neighboring coupling may be assumed. This is so called tight-binding approximation [85].

Because the Berry curvature effects arise only in spatially asymmetric potentials, we consider here a simplest two-dimensional asymmetric tight-binding model — the honey-comb lattice with two sites per unit cell each with different depth. The sites are called A and B as in Fig. 4.1. The lattice is defined by the lattice vectors $\mathbf{a}_1 = \sqrt{3}a\hat{e}_y$ and $\mathbf{a_2} = 3/2\ a\hat{e}_x + \sqrt{3}/2\ a\hat{e}_y$, where

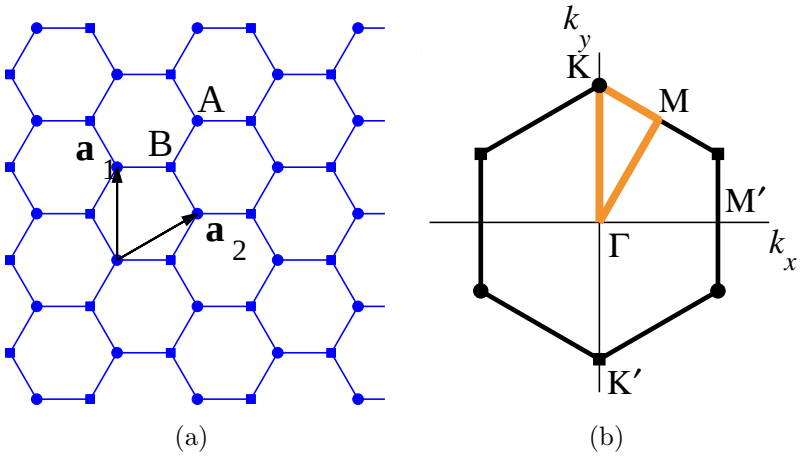

Figure 4.1: (a) Asymmetric honeycomb lattice for the tight-binding model. Sites A and B have different depth. Tunneling occurs only between sites connected by the lines. Lattice vectors $\mathbf{a}_1$ and $\mathbf{a}_2$ define the unit cell. The corresponding Brillouin zone in reciprocal space is shown in (b); due to symmetry all points marked by a circle correspond to the same K point.

a is the lattice constant. Here we consider only tunneling between neighboring sites, that is, tunneling only between sites of different type. The tight-binding Hamiltonian in this case may be written as

$$\hat{H}_{TB} = \sum_{\mathbf{R}s} \varepsilon_s \left|w(\mathbf{R}_s)\right\rangle \left\langle w(\mathbf{R}_s)\right| - h \sum_{\mathbf{R}\mathbf{R}'s} \left(\left|w(\mathbf{R}_A)\right\rangle \left\langle w(\mathbf{R}'_B)\right| + h.c.\right). \tag{4.17}$$

Here, summation is over cite type s and vectors $\mathbf{R}_s = m\mathbf{a}_1 + n\mathbf{a}_2 + \mathbf{R}_{s,0}$ that are associated with each site. Summation in the second term is only over nearest neighbors. On-site energies ϵ_A and ϵ_B and hopping element h are given by

$$\varepsilon_s = \left\langle w\left(\mathbf{R}_s\right)\right| \hat{H} \left|w\left(\mathbf{R}_s\right)\right\rangle, \tag{4.18}$$

$$h = \left\langle w\left(\mathbf{R}_A\right)\right| \hat{H} \left|w\left(\mathbf{R}_B\right)\right\rangle. \tag{4.19}$$

The analytic solutions for the Hamiltonian (4.17) can be found by switching to the basis of the Bloch states

$$|\phi^s(\mathbf{k})\rangle = \frac{1}{\sqrt{N}} \sum_{\mathbf{R}_s} e^{i\mathbf{k}\mathbf{R}_s} |w(\mathbf{R}_s)\rangle \,. \tag{4.20}$$

In the basis of $\left|\phi^A(\mathbf{k})\right\rangle$ and $\left|\phi^B(\mathbf{k})\right\rangle$, the Hamiltonian then becomes

$$H(\mathbf{k}) = \begin{pmatrix} \epsilon_A & V(\mathbf{k}) \\ V(\mathbf{k})^* & \epsilon_B \end{pmatrix}. \tag{4.21}$$

The off-diagonal term is given by

$$V(\mathbf{k}) = -h(1 + e^{i\mathbf{k}\cdot\mathbf{a}_1} + e^{i\mathbf{k}\cdot\mathbf{a}_2}). \tag{4.22}$$

Diagonalizing the matrix we find band energies

$$\varepsilon_\pm(\mathbf{k}) = \pm\sqrt{\left(\frac{\epsilon_g}{2}\right)^2 + |V(\mathbf{k})|^2}, \tag{4.23}$$

where we have chosen the reference level for energy in the middle of the gap between two bands defined by $\epsilon_g = \epsilon_A - \epsilon_B$. The band structure along high symmetry path is depicted in Fig. 4.2 (a). The lowest point of the Γ point. For non-equal depths of the sites the gap between the bands appear. The two bands come closest at point K, where $\mathbf{k}_0 = 4\pi/(3\sqrt{3}a)\,\mathbf{e}_y$ and $V(\mathbf{k}_0) = 0$. At that point, the separation between the bands is smallest and equal to ϵ_g.

In two-dimensional systems, the Berry curvature and the angular momentum are directed along the perpendicular (z) direction. Their values for the tight-binding model described above are

$$\Omega(\mathbf{k}) = \frac{\sqrt{3}\epsilon_g h^2 a^2}{16\mathcal{E}_+^3}[\sin(\sqrt{3}k_y a) - 2\sin(\sqrt{3}k_y a/2)\cos(3k_x a/2)], \tag{4.24}$$

$$S(\mathbf{k}) = \frac{M}{\hbar}(2\mathcal{E}_+)\Omega(\mathbf{k}). \tag{4.25}$$

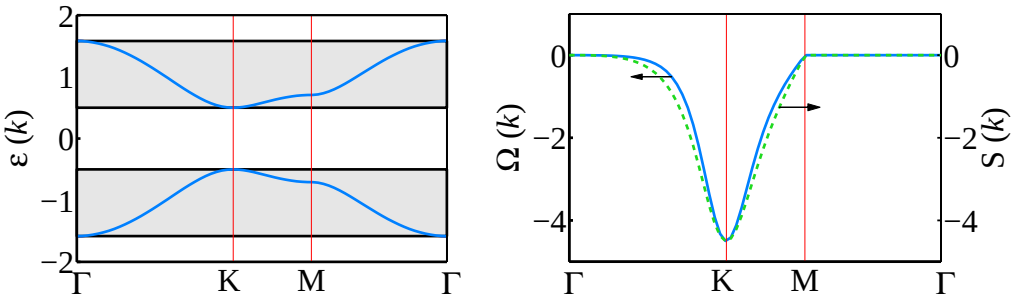

(a) (b)

Figure 4.2: (a) Dispersion for a tight binding model with $\epsilon_g = h = 1$. (b) Berry curvature Ω (left axis) and angular momentum S (right axis) in this case.

An intriguing relation at the K point, where S and Ω are minimum, is

$$S(\mathbf{k}_0) = \hbar \frac{M}{M^*}, \tag{4.26}$$

where M^* is the effective mass given by $M^* = -2\epsilon_g \hbar^2/(9h^2a^2)$.

The angular momentum S and Berry curvature Ω are plotted in reciprocal space in Fig. 4.2. Both of these quantities attain their maximum absolute value at $\mathbf{k}_0$ and all symmetrically located points. The value attained diverges as the gap size ϵ_g goes to zero. The angular momentum is not quantized.

The angular momentum arises because of current distributions within the wave packet. With the tight-binding model, this can be illustrated analytically [79, 86]. In Eq. (4.3) we take a Gaussian envelope of the Bloch states

$$f(\mathbf{k}) = \frac{1}{\sqrt{\pi}\sigma_k} e^{-\frac{(\mathbf{k}-\mathbf{k}_0)^2}{2\sigma_k^2}}, \tag{4.27}$$

with the spread σ_k much smaller than the size of the Brillouin zone. Envelopes

$f^A(\mathbf{R})$ and $f^B(\mathbf{R})$ of the wave packet in space defined as

$$|\Psi\rangle = \sum_{\mathbf{R}} f^A(\mathbf{R}) \left|w^A(\mathbf{R})\right\rangle + \sum_{\mathbf{R}} f^B(\mathbf{R}) \left|w^B(\mathbf{R})\right\rangle \tag{4.28}$$

to the first order in σ_k are

$$f^B(\mathbf{R}) \approx 2\sqrt{\pi}\sigma_k e^{\mathbf{k}_0\mathbf{R}} e^{-\frac{\mathbf{R}^2\sigma_k^2}{2}}, \tag{4.29}$$

$$f^A(\mathbf{R}) \approx \frac{ha\sigma_k^2}{\varepsilon_g} e^{i\frac{2\pi}{3}} \mathbf{R}\left(\hat{e}_x + i\hat{e}_y\right) f^B(\mathbf{R}). \tag{4.30}$$

The population of B sites is described by a Gaussian multiplied by a phase factor. In contrast, population in A sites vanishes at the center of the wave packet and reaches maximum at the distance $R \approx 1/\sigma_k$. The tight-binding equivalent of the current density in Eq. (4.12) is the bond current $I_{\mathbf{RR}'}$ along the bond between two neighboring sites A and B located in the cells associated with $\mathbf{R}$ and $\mathbf{R}'$. This is given by

$$I_{\mathbf{RR}'} = -\frac{i}{\hbar} h\left(f^{A*}(\mathbf{R}) f^B(\mathbf{R}') - f^A(\mathbf{R}) f^{B*}(\mathbf{R}')\right). \tag{4.31}$$

The bond current is therefore zero in the center, reaches a maximum absolute value at the distance $R \sim 1/\sigma_k$ and vanishes at infinity. This is illustrated in Fig. 4.3. The phase of the envelope changes by π as one goes around the circle but the momentum does not quantize. The continuous wave function has circulation in each unit cell.

4.1.4 Continuous honeycomb lattice

We confirm and extend the understanding obtained from the tight-binding model to a continuous potential. Since we are motivated by potential

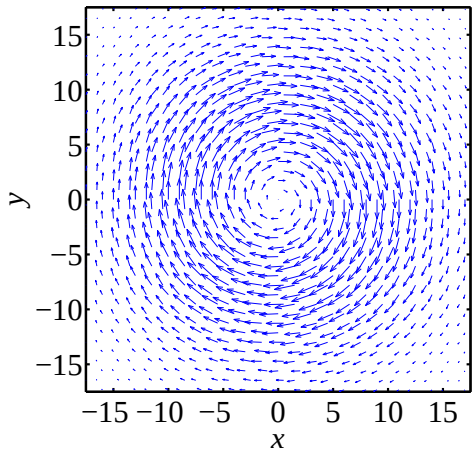

Figure 4.3: Distribution of the bond currents in the tight-binding limit for a wave packet centered at K point.

observation of the effects with ultracold atoms, we consider the following potential

$$V_{\text{lat}}(\mathbf{r}) = \sum_{i=1}^{6} A_i \cos(\mathbf{k}_i \cdot \mathbf{r} + \phi_i), \tag{4.32}$$

with the following parameters

$$\begin{gathered} A_1 = A_2 = A_3 = V_0 = -4.664, \\ A_4 = A_5 = A_6 = V_1 = -4, \\ \phi_1 = -\phi_2 = \phi_3 = 1.1, \\ \phi_4 = \phi_5 = \phi_6 = 0. \end{gathered} \tag{4.33}$$

In case of ultracold atoms this potential can be implemented by interference of six beams or by holographic techniques. The beam wave vectors are given by

$$\begin{gathered} \mathbf{k}_1 = -2\pi/3a\ \hat{e}_x + 2\pi/\sqrt{3}a\ \hat{e}_y, \quad \mathbf{k}_2 = 4\pi/3a\ \hat{e}_x, \\ \mathbf{k}_3 = \mathbf{k}_1 + \mathbf{k}_2, \quad \mathbf{k}_4 = \mathbf{k}_1 - \mathbf{k}_2, \\ \mathbf{k}_5 = 2\mathbf{k}_1 + \mathbf{k}_2, \quad \mathbf{k}_6 = \mathbf{k}_1 + 2\mathbf{k}_2. \end{gathered} \tag{4.34}$$

In this section, we use a system of units such that $\hbar = M = a = 1$. The ratio between the two amplitudes V_1 and V_0 control the width of the potential

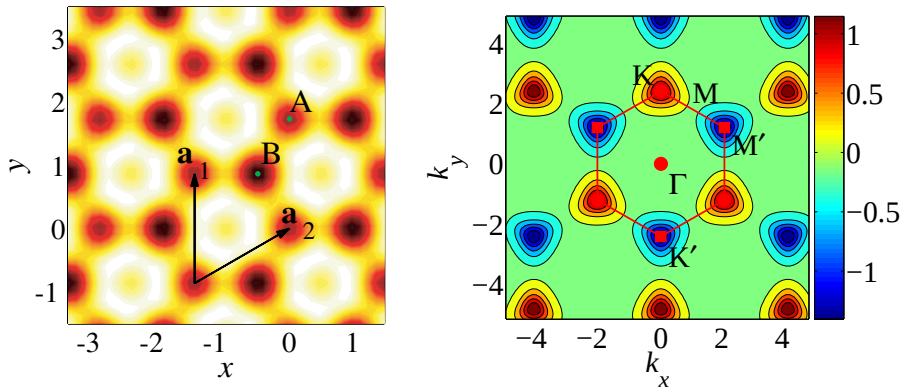

(a) (b)

Figure 4.4: (a) A continuous potential seen by the atoms; the dark regions correspond to the lowest values. (b) Berry curvature in the reciprocal space. It is peaked at the points where the bands come close one to another.

wells, the phase ϕ controls the ratio between the depths. For the symmetric potential $\alpha = \pi/3$. Here we use $\alpha = 1.1$. In Fig. 4.4 (a), we show the continuous potential. It is equivalent to the tight-binding model for infinitely large potential depths when the atoms become tightly localized in the wells.

The quantum dynamics of a wave packet is simulated numerically. For the simulations of the continuous time-dependent Schrödinger equation we use the split-operator fast Fourier transform approach, details of which, for example, are described in [87]. The steps of the simulations closely follow a possible experimental implementation. First, we start with a Gaussian wave function with the size much larger than the spacing between the sites. This may be a ground state of an atom in a harmonic potential. For the moment, we do not consider effects of interaction between particles and will return to this

discussion later. The lattice potential is introduced adiabatically. After which a uniform gradient in the potential $V(x, y) = fy$ is added. This gradient may be implemented experimentally either with a constant force f or by chirping the frequency of the beams that results in lattice acceleration a and effective inertial force $f = M/a$. The wave packet starts moving in reciprocal space along the direction of the acceleration and performs Bloch oscillations in real space.

Berry curvature and lattice-induced angular momentum for deep optical continuous potential are very similar to the tight-binding case. In Fig. 4.4 (b) we show Berry curvature calculated for the continuous potential of Eq. (4.32) for $V_1 = -4$, $V_0 = -4.664$. Similar to the tight-binding model, it has peaks at the points where two bands come close to each other. The lattice-induced angular momentum is also very similar. After the force is applied to the wave packet it drifts in reciprocal space at a constant rate and experiences different Berry curvatures at different times. Due to the transverse force that arises because of the Berry curvature in the first semiclassical Eq. (4.8) the wave packet drifts in the perpendicular direction. The displacement in the perpendicular direction is proportional to the integral of the Berry curvature along the path

$$\Delta \mathbf{r}_c = -\int_{\mathbf{0}}^{\mathbf{k}} d\mathbf{k}' \times \mathbf{\Omega}(\mathbf{k}'). \tag{4.35}$$

The motion of the wave packet center obtained with the continuous simulation of the wave packet dynamics is shown in Fig. 4.5 (a). When the force is small enough and tunneling between bands is neglected, the center of the wave packet

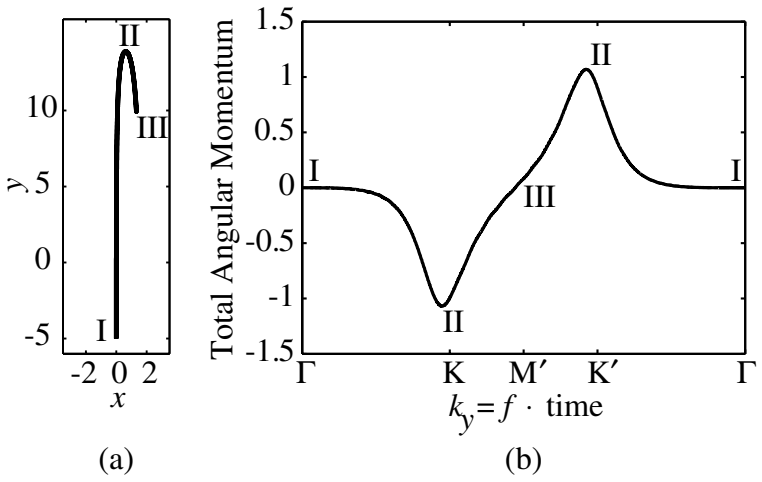

Figure 4.5: (a) Motion in real space of the center of the wave packet. (b) Angular momentum as a function of the position in reciprocal space, calculated for an acceleration $f = 0.05$ applied along the y-direction.

undergoes Bloch oscillation in real space from point I to point III and then back to point I. This is in contrast with a symmetric optical lattice where the oscillation occurs only along the direction of the drive here because of the Berry curvature it is also oscillating in the transverse direction. Such oscillations may be measured by a direct observation.

Another observable effect is associated with the lattice induced angular momentum. Here we do not rotate the lattice and it does not enter the second semiclassical equation of motion Eq. (4.9). As the wave packet moves in the reciprocal space angular momentum does reveal itself as the distribution of currents around the center of the wave packet. In Fig. 4.5 (b) we show average angular momentum with respect to the center along the trajectory. At the

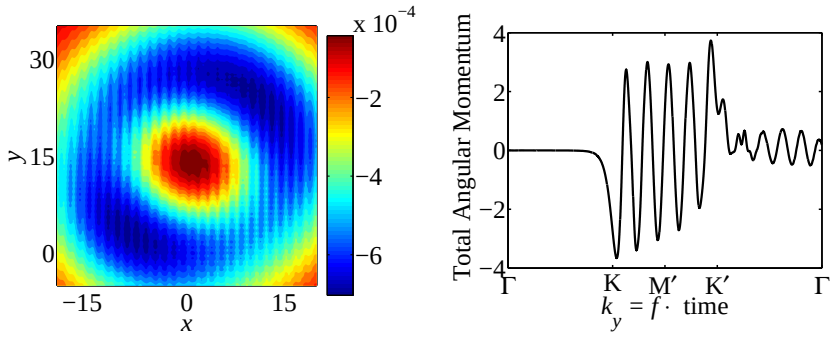

Figure 4.6: (a) Averaged angular momentum distribution calculated for the continuous potential when the wave packet reaches $\mathbf{k}_0$. The averaging assumes an experimental precision in position measurement of $\sigma_{\text{inst}} = a$. (b) Effect of non-adiabaticity. The beating frequency corresponds to the gap between the two lowest bands.

point II the induced angular momentum is the largest. Its directions are on two halves of the trajectory – from point I to point III and in opposite direction. Fig. 4.6 (a) shows averaged angular momentum of the atoms in the continuous case at the corner of the Brillouin zone at point K. It is very similar to the one obtained with the tight-binding model in Fig. 4.3. The density current varies from positive to negative values withing the unit cell, averaging assumes finite spatial resolution. The velocity distribution of the atoms can be measured by Doppler-sensitive Raman transitions [23]. In this way, atoms with a selected velocity are driven into a dark state, and one can remove the remaining atoms by shining resonant light. By imaging the remaining atoms, one may obtain the real space distribution of atoms with the given velocity. By changing the detuning, different sets of atoms are observed.

Adiabaticity is crucial during the process. An adiabatic criterion can be estimated based on the Landau-Zener formalism for tunneling between two levels with an avoided crossing. In this case the probability to tunnel is given by [47, 48]

$$P = \exp\left(-\frac{\pi\delta^2}{2\alpha}\right), \tag{4.36}$$

where δ is the gap between the states and α is the relative slope . This criteria, when a lattice potential with amplitude V_0 is introduced in time t_V, becomes

$$\frac{\delta^2 t_V}{V_0} \gg 1, \tag{4.37}$$

where δ is the gap between the first and the second bands at $k = 0$, since originally the width of the wave packet in the momentum space is much smaller than the size of the Brillouin zone (note that units with $\hbar = 1$, are used). The maximum "force" of the drive may be similarly estimated as

$$\frac{\epsilon_g}{\frac{\partial\epsilon}{\partial k}F} \gg 1. \tag{4.38}$$

Here ϵ_g is the smallest gap between the first and the second bands, and $\frac{\partial\epsilon}{\partial k}$ is the largest slope of the dispersion. An alternative expression may be derived based on the WKB approximation [85]

$$\frac{\epsilon_g^{3/2} m_{\text{eff}}^{1/2}}{F} \gg 1 \tag{4.39}$$

where the effective mass, m_{eff}, can be estimated from the dispersion as well. In the simulations we made sure that the adiabaticity criteria are fulfilled. We checked it numerically by increasing the driving force and observing the break

down of the adiabaticity. In Fig. 4.6 (b) the value of the angular momentum of the wave packet along the trajectory for the case when the driving force is just above the critical value. The observed beating frequency is given by the gap between the bands.

4.2 Discrete solitons

4.2.1 Introduction

Periodic lattices with substantial nonlinearities appear in various systems such as biological molecules [88], nonlinear optical wave guides [89], solid-state materials [90, 91], and Bose-Einstein condensates (BECs) [92]. In these systems, interplay between linear coupling effects among adjacent sites and nonlinearity can result in a self-localized state — lattice or 'discrete' soliton [88–92]. Until recently direct observation of discrete solitons has been performed only in one-dimensional optical wave guides [89, 93, 94]. Yet in systems with dimensionality more than one a number of fundamental phenomena, such as vortex lattice solitons, bright lattice solitons that carry angular momentum, are expected [95]. Recently a novel experimental technique to produce photonic crystal by optical induction allowed the authors of Ref. [96] to directly observe two-dimensional discrete solitons.

As was discussed in the introduction, similar to dynamics of the optical pulses in nonlinear photonic crystals, the evolution of a BEC in an optical lattice is governed by a nonlinear Schrödinger equation (NLSE) with periodic potential, hence many predictions observed with respect to photonics

are expected with a BEC. In the case of BEC, the nonlinear coefficient can be either positive or negative for repulsive or attractive atomic interaction respectively, with most of the experiment being done with repulsive atoms. One-dimensional solitons in the absence of periodic potential were observed in attractive BEC [97, 98]. One-dimensional matter-wave discrete solitons in optical lattices were studied extensively theoretically both for attractive and repulsive interactions [99–101]. Decoherence of the repulsive BEC during Bloch oscillation in a 1D optical lattices observed in experiments [102–104] was related theoretically to generation of discrete soliton [92, 105] (similar decoherence phenomena in two- and three-dimensional (3D) optical lattices have been reported [106, 107]). The observation of the matter-wave discrete soliton was reported in 1D [108].

In contrast to free space, stable localized modes are possible in periodic potentials in any dimension both for attractive and repulsive interaction. In the case of a *self-repulsive* BEC generation of multidimensional matter-wave discrete solitons due to a modulational instability has been predicted theoretically [109], and the existence and stability of 2D discrete soliton have been studied [110]. Using a variational approximation and direct numerical simulation the authors of Ref. [111] demonstrated that in the case of *attractive* interaction above the threshold number of atoms, the initial BEC wave packet placed in an optical lattice collapses into multidimensional discrete solitons.

The effect of the lattice for quantum wave packets much larger than the unit cell of the periodic potential, may be replaced by the effective mass. In

which case, even for *repulsive* interaction, the wave function envelope dynamics may be governed by the NLSE with negative (self-focusing) nonlinearity [112, 113]. As we discussed in the previous section, the center of the quantum wave packet in momentum space can be easily shifted in a controlled manner by accelerating the lattice (for instance by chirping the relative detuning of the beams creating the lattice) as was demonstrated in early experiments with cold atoms [14] and later with BEC [114]. Recently, the effects of negative effective mass have been studied with ^{87}Rb condensates in one dimensional optical lattices [115].

In 2D above critical value of the self-focusing nonlinearity wave packet collapses. The nonlinearity in case of a BEC is determined by the number of atoms, scattering length, effective mass in the lattice and frequency of transverse confinement. When wave packet size becomes comparable to the size of a unit cell, the effective mass approximation breaks down. If the nonlinearity is close to that one for which a discrete soliton is supported by the band gap, part of the wave function is transferred to discrete soliton and part decays into linear waves. This is a general phenomenon for NLSE when a state is prepared sufficiently close to the localized state [116].

We first obtain a criteria for critical value of interaction using variational approximation for the wave packet envelope dynamics [117, 118] and effective mass approximation [112, 113]. We also show that this critical nonlinearity is associated with the smallest nonlinearity for which the lattice supports discrete solitons [119–121]. This value is equal to the only nonlinearity with

which a stationary solution is possible for the free space 2D NLSE with the corresponding effective mass. In what follows, we illustrate discrete soliton generation with a self-repulsive BEC using two numerical examples: square optical lattice for the parameters considered in [110] and asymmetric honeycomb lattice. The latter was originally considered in the previous section as a system to study effects of Berry curvature in periodic potentials [86]. For both systems, we simulate all the stages of the possible experiments: adiabatic introduction of the lattice, half of the Bloch oscillation and a wait period for the wave function to collapse to discrete soliton.

4.2.2 Variational Approximation

The variational approximation for the NLSE was originally developed in nonlinear optics (extensive review was published in [118]). It was successfully applied to describe BEC dynamics [122–126], including evolution in the optical lattices [92, 111, 127]. We first apply the variational approximation ideas to the evolution of a BEC Gaussian wave packet in free space in D dimensions.

The Gross-Pitaevskii (GP) equation is a NLSE describing the dynamics of BEC:

$$i\hbar\frac{\partial}{\partial t}\psi(\mathbf{r},t) = \hat{H}\psi(\mathbf{r},t) = \left(-\frac{\hbar^2}{2m}\nabla^2 + V(\mathbf{r}) + Ng_D\left|\psi(\mathbf{r},t)\right|^2\right)\psi(\mathbf{r},t), \quad (4.40)$$

with a nonlinear term being due to the mean-field treatment of the interaction between the atoms. It can be both positive and negative depending on the scattering length of the atomic collisions. Most of the current experiments

deal with self-repulsive BECs (positive scattering length). Here we normalize the wave function to unity.

To apply variational approximation, we restrict the dynamics of the quantum wave packet in free space ($V(\mathbf{r}) = 0$) in D dimensions to the form

$$\Psi_D(r) = \left(\frac{\alpha}{\pi}\right)^{D/4} e^{-(\alpha+i\beta)r^2/2}, \tag{4.41}$$

where α and β are variational parameters, α being inversely proportional to the width of the wave packet squared. The semi-classical Lagrangian corresponding to the GP equation may be written as

$$L(\alpha, \dot{\alpha}, \beta, \dot{\beta}) = \langle \Psi_D | \, i\hbar \frac{\partial}{\partial t} - \hat{H} \, | \Psi_D \rangle \, . \tag{4.42}$$

The terms necessary for its calculation are

$$\langle \Psi_D | \, i\hbar \frac{\partial}{\partial t} \, | \Psi_D \rangle = \frac{\hbar D}{4} \frac{\dot{\beta}}{\alpha}, \tag{4.43}$$

$$\langle \Psi_D | - \frac{\hbar^2}{2M} \nabla^2 \, | \Psi_D \rangle = \frac{\hbar^2 D}{4m} \left(\alpha + \frac{\beta^2}{\alpha} \right), \tag{4.44}$$

$$V_{\text{int}} = \frac{N g_D}{2} \int dr \, |\Psi_D(r)|^4 = \frac{N g_D}{2} \left(\frac{\alpha}{2\pi} \right)^{D/2}. \tag{4.45}$$

The first term describes temporal evolution, the second is associated with kinetic energy, and last term describes mean field interaction between particles. After the substitution $\gamma = 1/\alpha$ (γ is proportional to the wave packet spread), the Lagrangian equation becomes

$$\gamma \ddot{\gamma} - \frac{1}{2} \dot{\gamma}^2 = \frac{2\hbar^2}{m^2} + \frac{2 N g_D}{m} \gamma \left(\frac{1}{2\pi\gamma} \right)^{D/2}. \tag{4.46}$$

In the free space case, without mean field interaction ($g_D = 0$), this equation gives an exact result for dependence of the wave packet dispersion on time

$$\gamma^2 = 2(\sigma_0^2 + At^2), \tag{4.47}$$

where $\sigma_0^2 = \gamma^2(t = 0)/2$ is initial spatial second moment of the wave packet, and

$$A = \frac{\hbar^2}{2m^2\gamma^2(t = 0)} = \frac{\hbar^2}{4m^2\sigma_0^2}. \tag{4.48}$$

Equation (4.46) is particularly simple in 2D. In this case, the right hand side becomes independent of parameters of the wave packet, and the dynamics is effectively described in the same way as for non-interacting atoms. The wave packet becomes dispersionless when the right hand side of (4.46) vanishes. This gives the criteria for critical interaction strength

$$Ng_c = \frac{2\pi\hbar^2}{m}. \tag{4.49}$$

For negative nonlinearity, when $|g| > g_c$, the wave packet collapses.

Quantum motion of a wave packet in periodic potential can be effectively described as motion in free space using the concept of effective mass, which in principle may be negative. We comment on this below.

4.2.3 Effective Mass

When the external potential $V(\mathbf{r})$ is periodic, and the size of the quantum wave packet is much larger than its unit cell, the effect of the potential for different wave vectors $\mathbf{k}_0$ may be described in terms of the effective mass.

The effective mass tensor may be inferred from the band dispersion [112, 113]

$$m_{\text{eff},\mu\nu} = \hbar^2 \left(\frac{\partial^2 E}{\partial k_\mu \partial k_\nu} \right)^{-1}, \tag{4.50}$$

When the wave packet is delocalized in real space over many lattice sites, in momentum space it is localized around a given wave vector $\mathbf{k}_0$. The effective NLSE then can be written for the envelope $f_n(\mathbf{r})$ over different Bloch bands

$$\psi(\mathbf{r}, t) = \sum_n f_n(\mathbf{r}, t) \phi_{n\mathbf{k}_0}(\mathbf{r}) e^{-iE_{n\mathbf{k}_0} t/\hbar}, \tag{4.51}$$

here $f_n(\mathbf{r}, t)$ is a slowly varying function within the unit cell, and each Bloch function $\phi_{n\mathbf{k}_0}$ is the solution of the linear eigenproblem

$$\left(-\frac{\hbar^2}{2m} \nabla^2 + V(\mathbf{r}) \right) \phi_{n\mathbf{k}}(\mathbf{r}) = E_{n\mathbf{k}} \phi(\mathbf{r}), \tag{4.52}$$

normalized to the area of the unit cell

$$\int_{\text{cell}} d\mathbf{r} \left| \phi_{n\mathbf{k}_0}(\mathbf{r}) \right|^2 = \Omega. \tag{4.53}$$

In the experiments, it is possible to prepare wave packets that populate only the lowest band [14]. The NLSE for the envelope incorporates the effects of the external potential into effective mass [112, 113]

$$i\hbar \left(\frac{\partial f_n}{\partial t} + \mathbf{v}_g \cdot \nabla f_n \right) = \left(-\frac{\hbar^2}{2m_{\text{eff},\mu\nu}} \frac{\partial^2}{\partial x_\mu \partial x_\nu} + N g_2' \left| f_n \right|^2 \right) f_n, \tag{4.54}$$

where $\mathbf{v}_g$ is drift velocity of the wave packet center given by

$$\mathbf{v}_g = \frac{1}{m} \left\langle \phi_{n\mathbf{k}_0} \right| \hat{\mathbf{p}} \left| \phi_{n\mathbf{k}_0} \right\rangle, \tag{4.55}$$

and effective interaction strength g_2' is given by

$$g_2' = \frac{g_2}{\Omega} \int\limits_{\text{cell}} d\mathbf{r} \, |\phi_{n\mathbf{k}_0}(\mathbf{r})|^4. \tag{4.56}$$

In the particular examples we will discuss below, the wave packet will be driven to the point in the Brillouin zone where $\mathbf{v}_g = 0$, and effective mass tensor is negative in all directions, hence the envelope dynamics will be governed by NLSE with negative mass. This can be viewed as a NLSE with *positive* mass with *inverted* sign of nonlinearity, which is clearly seen from the equation for complex conjugate of the envelope function

$$i\hbar \frac{\partial f_n^*}{\partial t} = \left(-\frac{\hbar^2}{2\,|m_{\text{eff},\mu\nu}|} \frac{\partial^2}{\partial x_\mu \partial x_\nu} - N g_2' \, |f_n^*|^2 \right) f_n^*. \tag{4.57}$$

This equation can be obtained by taking the complex conjugate of (4.54) and using absolute value of the mass.

Hence, in this situation, as long as the condition for the effective mass approximation holds, m in the Eq. (4.46) should be replaced by m_{eff}. In the case, when an effective mass and nonlinearity have opposite signs and $|g_2'| > g_{2,c}'$, where critical interaction strength is defined in (4.49), with mass being replaced by effective mass, the wave packet collapses. Notice that in general from (4.46) it follows that dispersion of the wave packets for any D when the effective mass is negative is described by the equation with positive mass and inverted sign of nonlinearity. When the size of the wave packet becomes comparable to the lattice spacing the effective mass approximation no longer holds. In 2D there is a nonlinearity below which discrete solitons are

not supported by the bandgap. If the nonlinearity is sufficiently larger than this delocalizing nonlinearity, part of the wave packet decays into discrete soliton and part decays into linear waves.

4.2.4 Delocalization

In contrast to 1D, where discrete soliton may correspond to arbitrary nonlinearity, in 2D and higher dimensions discrete solitons are possible only for nonlinearity above a critical value [119]. The authors of [120] considered the possibility of observing the delocalization transition with matter-wave discrete solitons in optical lattices, when an irreversible change from discrete soliton to delocalized states is produced for a slow change in the lattice parameters. This delocalizing nonlinearity may be associated with the critical nonlinearity for a Gaussian wave packet to collapse as discussed in Section 4.2.2.

The concept of the effective mass is not generally applied to the discrete soliton since in the middle of the gap the discrete soliton is localized within one lattice site. As the chemical potential of the discrete soliton comes close to a band of linear states, its space extension increases, hence one may expect that the effective mass approximation becomes applicable. The results of Section 4.2.2 imply that there is only one value of nonlinearity for which the localized modes are supported in 2D free space when the envelopes of the localized modes are approximated by Gaussians. This also can be shown in general from the scaling arguments for the 2D NLSE. Indeed, if the normalized

wave function $\psi_1(x, y)$ is the solution of

$$-\nabla^2\psi_1 + \gamma\psi_1^3 = \tilde{\mu}\psi_1, \tag{4.58}$$

then the normalized wave function $\psi_2 = B\psi_1(Ax, Ay)$ is the solution of

$$-\nabla^2\psi_2 + \gamma\psi_2^3 = A^2\tilde{\mu}\psi_1. \tag{4.59}$$

This means that in 2D free space there is only one possible value of γ for which localized modes can be found for any value of $\tilde{\mu}$, the shape of the soliton for different μ can be obtained only by scaling.

Localized wave packets with very large extension correspond to the critical nonlinearity. As their size is reduced, other corrections due to the lattice also start to play a role. The variational approximation gives a clear picture of what happens to initially localized states of the NLSE in 2D. It predicts the critical value of nonlinearity above which evolution of the wave packet width changes character. One may expect that Ng_c given in (4.49) is close to the exact value. We confirmed this expectation by performing direct self-consistent numerical simulations based on the effective potential approach suggested in [121]. Similar to the self-consistent Hartree-Fock approximation, one may consider a discrete soliton to be a localized state in the effective potential created by itself

$$V_{\text{eff}}(\mathbf{r}) = -Ng'_D \left|\psi(\mathbf{r})\right|^2. \tag{4.60}$$

In the numerical simulation, we started with an *arbitrary* nodeless initial wave function, and with the imaginary time evolution found the ground state of the

potential (4.60) for the Hamiltonian given by

$$\hat{H}_{\text{eff}} = -\frac{\hbar^2}{2\,|m_{\text{eff}}|}\nabla^2 + V_{\text{eff}}(\mathbf{r}), \tag{4.61}$$

and used it in the next step of iteration. We found that independent of the initial guess state above the critical value

$$Ng'_{\text{num}} = \frac{5.850\ \hbar^2}{|m_{\text{eff}}|}, \tag{4.62}$$

the self-consistent procedure resulted in collapsing states with infinite negative energy, while for smaller nonlinearities the states expanded, with energy going to zero. This value differs from the one for an extended Gaussian wave packet to collapse (4.49) by approximately 10 percent.

As an alternative method we also reduced the 2D equation to a 1D ordinary differential equation and solved two point boundary value problem ($\psi'(0) = 0$, $\psi(\infty) = 0$) with the shooting method [128]. We found that for arbitrary energy, nodeless solitons in free space with arbitrary size are supported only for one value of nonlinearity given by the same value as in (4.62).

The direct dynamical simulations discussed in the next section confirm the existence of the critical nonlinearity above which a wave packet with a finite size collapses. Also, using the imaginary time evolution for different values of chemical potential in the gap, we find corresponding nonlinearity for discrete soliton in the lattice to exist. The minimum nonlinearity found as a result of this calculation is also in a good agreement with (4.49) and (4.62).

4.2.5 Numerical Simulations

First, we give general remark about the numerical simulations, and then consider two specific numerical examples in continuous potentials: square and honeycomb lattices.

By choosing appropriate units of length, L_u, and mass, $M_u = M_{\text{atom}}$, the GP equation (4.40) is reduced to a dimensionless form

$$i\frac{\partial\psi}{\partial t} = \left[-\frac{1}{2}\nabla^2 + V_L(\mathbf{r}) + Ng_2\left|\psi\right|^2 + \mathbf{F}\cdot\mathbf{r}\right]\psi. \tag{4.63}$$

We also add an external force $\mathbf{F}$. This, in the case of optical lattices, may be created by accelerating the lattice, for example, by sweeping the relative frequency of the beams creating the lattice. In this case, unit of energy of the problem is $E_u = \hbar^2/M_u L_u^2$ and the unit of time is given by $t_u = \hbar/E_u$. When the unit of length is chosen to be equal to the inverse wave vector of the light creating the optical lattice $L_u = 1/k_L$, typical maximum depths of the optical potentials achievable in the dissipationless regime are of order 20. The forces created by accelerating the lattice are limited due to the finite lifetime of the excited states, in case of alkali atoms to about $1000t_u$, in the experiments [14] forces on the order of ~ 1 to 10 were used. The dynamics of the BEC is described by a 2D equation in the case when the strong confinement in the transverse direction "freezes" the wave function in that direction to the harmonic oscillator ground state. This happens when oscillator length in that direction $l_z = \sqrt{\hbar/M_{\text{atom}}\omega_z}$ becomes smaller than the condensate healing length $\xi = (4\pi na)^{-1/2}$, where n is atom density and a is scattering length.

When, at the same time, l_z is still larger than 3D scattering length, $|a|$,

$$|a| < l_z < \xi \tag{4.64}$$

the collisions between the atoms preserve their 3D character, yet the dynamics of the BEC in the two other directions are effectively described by 2D GP equation [12]. Such a regime was recently demonstrated experimentally [13]. The nonlinear coefficient in this case is given by

$$g_2 = \left(\frac{8\pi\omega_z\hbar^3}{M_{\rm atom}}\right)^{1/2} a. \tag{4.65}$$

The experimental system, therefore, provides great flexibility with which the nonlinear coefficient in corresponding NLSE can be controlled. The parameters variable in experiments are number of atoms, N, the frequency of transverse confinement ω_z, and the scattering length, a. In principle, a may be tuned by a magnetic field with Feshbach resonances [65]. For the experimental parameters of [13] we estimate the nonlinear coefficient in present units to be $Ng_2 \sim 6000$. For the ansatz chosen above to be valid, kinetic energy (4.44) should be larger than interaction energy (4.45). It means that the nonlinearity should be smaller than $\sim 2\pi$. Below we consider only the cases when this holds. For BEC the effective nonlinearity can be always reduced either by changing number of atoms or trapping frequency in transverse direction.

The stationary states of Eq.(4.63) are described by solutions of the form: $\psi(\mathbf{r},t) = \phi(\mathbf{r})\exp(-i\mu t)$, where μ is the chemical potential. Localized states can be found for μ in the gaps of linear problem.

Below, we consider two examples. The first one is based on parameters for which existence and stability of the solitons were studied in [110]. Our consideration extends the treatment to suggest a specific approach for discrete soliton generation based on the ideas outlined above. The second example deals with the asymmetric honeycomb lattice that we considered to observe effects of the Berry curvature in section 4.1 in the context of observing self-rotation and Berry curvature effects for quantum wave packets in asymmetric periodic potentials [86]. As we have included the effects of interaction to the continuous simulations performed for that study, we have observed robust spontaneous generation of the discrete soliton above a critical interaction strength for wave packets left at the corner of the Brillouin zone. Here, we discuss how this effect could be naturally explained in terms of the effective mass concept.

In both cases, we have performed simulations in a form that mimics possible experiments. We start with a Gaussian wave packet in free space with a size that is much larger than the unit cell of the potential. The process may be divided into three stages: (1) adiabatic introduction of the lattice potential, (2) acceleration of the lattice for half of the Bloch oscillation, and (3) a wait period for the wave packet to collapse. In the first two stages, adiabaticity is crucial. The same conditions as discussed in Section 4.1 must be valid.

As a first example, we discuss the model potential considered in [110] for

existence and stability of 2D discrete soliton in continuous potentials, namely

$$V_L(x, y) = V_0(\sin^2 x + \sin^2 y). \tag{4.66}$$

Such a potential may be experimentally obtained by overlapping two pairs of counter-propagating beams, far detuned from atomic resonance to reduce effects of spontaneous emission. These beams also have to be detuned from each other to avoid a cross term. As in [110], we use amplitude $V_0 = 5$.

In Fig. 4.7(a), we show the dispersion of the linear problem (4.52) for the potential (4.66) along the high symmetry directions. The first band has a minimum at zero momentum (Γ point), and a maximum at the corner of the Brillouin zone (M point). There exist directions on the plane for which the maximum value of the potential is smaller than V_0. These are orthogonal (x,y) directions, while the absolute maximum of the potential is $2V_0$. For the chemical potential of the localized states above V_0 (shown as a green dashed line in Fig. 4.7(a)), the BEC states are quasi-unbound. For values of μ close to this boundary an adequate description of discrete soliton is not possible within one-band tight-binding model. This is because situations when nodes of the solitonic wave functions are located at the potential minima are possible [110].

The xx-component of the effective mass tensor (4.50) is shown in Fig. 4.7(b). Since the potential is separable and symmetric, the yy-component has the same dependence on k_y, and the tensor is diagonal. At the points of global maximum and minimum of the dispersion, the effective mass in both directions is the same. At the Γ point, the effective mass has the smallest positive value

($m_{\mathrm{eff},\Gamma} = 5.53$), while at the point M it is negative and has the smallest absolute value ($m_{\mathrm{eff,M}} = -5.03$). Hence the smallest nonlinearity is necessary for the wave packet to self-collapse at the M point. The fact that in 1D, for a sinusoidal potential for wave vectors, k, larger than half of the largest vector in the Brillouin zone, $k > k_{\mathrm{crit}} = \pi/(2a)$, where a is lattice spacing, allows to give a physical explanation of the origin of the Landau instability studied in [129] in terms of tight-binding approximation. For any interaction strength, wave packets composed of Bloch waves for $k < k_{\mathrm{crit}}$ remain wave packets composed of Bloch waves, while for $k > k_{\mathrm{crit}}$, when interaction is large enough, they partially collapse to localized modes.

To investigate the validity of the effective mass description, we checked in numerical simulations the predictions that may be based on the formulas discussed in previous sections. From (4.48), we introduce the quantity characterizing dispersion of the wave packet

$$\chi = \frac{A\sigma^2}{A\,\sigma^2|_{g_2=0}} = 1 + \frac{N g_2' m_{\mathrm{eff}}}{2\pi}, \tag{4.67}$$

which changes linearly with interaction. As it becomes negative, the wave packet collapses. Notice that in this expression, the effective interaction strength is related to continuous interaction strength with (4.56), which for the case of separable sinusoidal potential at least partially may be computed analytically. For the separable potential (4.66) the solution of the stationary eigenproblem (4.52) is separable: $\phi(x,y) = \phi_x(x)\phi_y(y)$, where each wave function is

given by the solution of the corresponding equation

$$\left[\frac{1}{2}\frac{\partial^2}{\partial x^2} + \left(E - \frac{V_0}{2}\right) + \frac{V_0}{2}\cos 2x\right]\phi_x(x) = 0. \tag{4.68}$$

Due to Bloch-Floquet theorem, the solution is a product of a periodic Bloch function $u_k(x)$ and a plane wave

$$\psi_{x,k_x}(x) = e^{ik_x x}u_k(x). \tag{4.69}$$

After the following substitutions

$$\begin{array}{c} b = 2\left(E - \frac{V_0}{2}\right), \\ z = x, \\ q = -\frac{V_0}{2}, \\ \psi_x(x) = y(z), \end{array} \tag{4.70}$$

Eq. (4.68) becomes the Mathieu equation [130]

$$\frac{\partial^2 y}{\partial z^2} + (b - 2q\cos 2z)y = 0. \tag{4.71}$$

As a result the general solution of (4.68) are given by combination of symmetric and asymmetric Mathieu functions with characteristic exponent $r = k_x$, characteristic values a_r and b_r correspondingly and parameter $q = -V_0/2$

$$\psi_{x,k_x}(x) = \mathrm{Ce}_r(a_r, q, z) + i\mathrm{Se}_r(b_r, q, z). \tag{4.72}$$

At the top and bottom of the Brillouin zone this is just a symmetric Mathieu function

$$\psi_{x,k_x}(x) = \mathrm{Ce}_r(a_r, q, z) = \mathrm{Ce}_{k_x}\left(2\left(E - \frac{V_0}{2}\right), -\frac{V_0}{2}, x\right). \tag{4.73}$$

Introducing the numerical factor

$$I = \frac{\left(\int\limits_{-\pi/2}^{\pi/2} Ce_r^4(a,q,z)dz \right)^2}{\left(\int\limits_{-\pi/2}^{\pi/2} Ce_r^2(a,q,z)dz \right)^4}, \tag{4.74}$$

we get the following dependence of χ on interaction strength,

$$\chi = 1 + \frac{\Omega m_{\text{eff}} I}{2\pi} N g_2. \tag{4.75}$$

Therefore the critical interaction strength is given by

$$N g_{2,c} = \frac{2\pi}{\Omega \left| m_{\text{eff}} \right| I}. \tag{4.76}$$

For the considered example, area of the lattice unit cell is $\Omega = \pi^2$ and the numerical factor for the top of the band is $I_{\text{M}} = 0.398$, which makes the critical interaction strength $N g_{2,c} = 0.285$.

To test predicted behavior of the parameter ξ, we perform a numerical simulation with a continuous potential. We start with a wave packet of size $\sigma_{x,y} = 15/\sqrt{2}$, while the size of the unit cell is π in each direction. The lattice potential is ramped from $V_0 = 0$ to $V_0 = 5$ in $t_V = 450$, then the lattice is accelerated with force $F = 0.01$ in diagonal [11] direction. The acceleration is halted after the wave packet undergoes half of the Bloch oscillation, in other words, when its center is located at point M in momentum space. After this, the wave packet expands freely in the presence of the lattice potential. Ramp time and the force satisfy adiabaticity conditions so that the wave packet during evolutions stays in the first band. In addition to expanding the wave

packet at the top of the band, we have studied the expansion as soon as the lattice was introduced without an external field, **F**. In both cases the agreement with the analytic prediction (4.67) is very good (see Fig. 4.7(c) and Fig. 4.7(d)).

As the external force is removed, the wave packet contracts due to phases accumulated during the acceleration even in the linear case. But this is only when the interaction is above critical so that localized modes are formed. To find a stationary localized solution we followed the optimization procedure based on a descent technique with Sobolev preconditioning used in [110] and described in [131]. In Fig. 4.8(a), we display the dependence of the nonlinearity on chemical potential of the discrete soliton. The error bar shows the estimated uncertainty for the curve to intersect the band of extended states obtained by interpolating to infinite size and infinite relaxation time of the descent procedure. The agreement with the argument based on effective mass and free space solitons given in Section 4.2.4 is excellent. As one starts with an extended wave packet and nonlinearity supported by the gap, it shrinks and may lose some part to radiation (extended states), so that the effective interaction experienced by the localized mode is then just a fraction of the actual interaction. As shown in Fig. 4.8, the solitons are formed inside the gap. When the nonlinearity increases, their chemical potential increases but not significantly, so that they stay relatively close to the top of the first band.

Extending work of Section 4.1 to the case when interaction between particles is described by the Gross-Pitaevskii equation, we have observed

self collapse of the wave packet to localized modes above critical interaction strength [86]. The effective mass concept provides an explanation of the phenomena and relates the critical interaction strength to other parameters of the problem.

We take the same potential described by Eq. (4.32). The band structure is shown in the Fig. 4.9(a). Asymmetry splits the first band in the middle. In this case, the boundary between strongly bound and quasi-unbound states is located in the second gap. The effective mass is negative in both directions at K point (see Fig. 4.9(b)). We start with a Gaussian wave packet in free space which has spatial dispersion $\sigma_{x,y} = 10/\sqrt{2} \approx 7.071$. Since the size of the unit cell in this case is $\Omega = 3\sqrt{3}/2$, the wave packet occupies several unit cells. The lattice potential is introduced in time $t_V = 120$ and we accelerate it along y-axis with $|\mathbf{F}| = 0.05$. In this case, conditions in (4.37)-(4.39) are fulfilled. An analysis of the expansion for different values of the interaction at the bottom of the first band (Γ point) and the top of the first band (K point) is shown in the Fig.4.9(c). To compare results of the continuous simulation with the prediction of the (4.67), we calculated effective mass, M_{eff}, from the band structure and the numerical factor I, that involves integrals of the Bloch wave functions, by integrating over one unit cell wave functions obtained by adiabatic evolution. Their values are $M_{\text{eff},\Gamma} = 1.7986$, $I_\Gamma = 0.9396$ at the point Γ and $M_{\text{eff,K}} \approx -0.8918$, $I_K \approx 1.9567$ at the point K. Probability density plots after expansion for $\Delta t_{\text{exp}} = 200$ at the K point are shown in the Fig. 4.10. As interaction increased past the critical value, the lattice solitons are dynamically

formed. The figure illustrates that the phenomena is also observed for a square lattice: the fraction of the wave function transferred to the localized modes decreases as the interaction strength is increased. The effective interaction experienced by each mode is such that the corresponding chemical potential is close to the first band.

As we have seen in the numerical examples discussed above, if the nonlinearity is small enough, the wave packet collapses into a single discrete soliton. Clouds of ultracold atoms can be imaged non-destructively [132]. Observation of a persistent atomic cloud localized to dimensions comparable to the wavelength of the light forming the lattice will be a clear signature of the discrete soliton formation. Observations of the predicted delocalizing transitions with a single discrete soliton prepared in a controlled fashion for a varying lattice depth is also an exciting possibility.

4.3 Effective spin-orbit coupling

As we discussed in Section 4.1, geometric phase appears in crystal momentum space whenever time-reversal and/or spatial inversion symmetries are broken in the lattice [77, 78]. The Berry phase may also appear in systems with spin-orbit coupling due to broken chiral symmetry. In solid state systems, such as ferromagnetic crystals for example, the geometric phase due to broken time-reversal symmetry is responsible for the anomalous Hall effect (AHE) [81], that is the generation of a transverse current by an electric field even in the absence of a magnetic field. A closely related phenomenon, recently proposed

for spintronics applications [133], is the spin Hall effect (SHE) [134–136]: the production of a transverse spin current by an electric field in the presence of a significant spin-orbit coupling. The observation of the spin Hall effect was recently reported in solid state systems [137, 138].

We showed how spin-orbit coupling and geometric phase may be produced for atoms in 2D optical lattices and proposed experiments to explore their consequences. Optical lattices provide great flexibility with which potentials can be created and atomic quantum states prepared. By choosing the polarization of the beams appropriately, the internal degrees of freedom of the atom can be coupled to their momenta as in the (relativistic) spin-orbit effect for electrons in solids. In particular, we show how a Hamiltonian similar to the Rashba Hamiltonian for electrons in 2D semiconductor systems [139] can arise in the description of atoms propagating in an optical lattice produced by the interference of suitably polarized laser beams. As we mentioned before, a constant force field, analogous to an electric field for electrons can be produced by accelerating the lattice [14]. By studying the transport of the atoms in these spin-dependent lattices, one can observe effects similar to AHE and SHE.

Atoms in different internal (spin) states can interact with laser light in different ways depending on its polarization. This effect has recently been applied to the experimental study of quantum transport of atoms in one-dimensional optical lattices in the *localized* regime [140, 141], for which a wide range of phenomena has been theoretically proposed (see references at [141],

and also, for instance [142], and references there in). Here, we consider ultracold atom dynamics in 2D optical lattices in the *itinerant* regime where motion through the lattice is of concern.

4.3.1 Fictitious magnetic field

Let us consider the Hamiltonian for an atom interacting with a configuration of laser beams producing an electric field $\mathbf{E}(\mathbf{r})$. In general, if the detuning of the light frequency ω from the resonance frequency is large with respect to the radiative width of the excited states, spontaneous emission is suppressed and we can adiabatically eliminate the excited states by writing an effective Hamiltonian which involves only the ground state sublevels [7, 143, 144]:

$$\begin{aligned} H_{\text{eff}} &= \sum_{\alpha\beta\gamma} \frac{\left(\mathbf{E}^*(\mathbf{r}) \cdot \mathbf{D}^*_{\gamma\alpha} \left|g:\alpha\right\rangle\right) \left(\mathbf{E}(\mathbf{r}) \cdot \mathbf{D}_{\gamma\beta} \left\langle g:\beta\right|\right)}{\hbar(\omega - \omega_\gamma)} \\ &= \sum_{\alpha\beta} V_{\alpha\beta}(\mathbf{r}) |g:\alpha\rangle\langle g:\beta|. \end{aligned} \tag{4.77}$$

For a ground state of total angular momentum F, the indexes α and β run over the $2F+1$ Zeeman sublevels. $\mathbf{D}_{\gamma\beta} = \langle e:\gamma| \mathbf{d} |g:\beta\rangle$ is the dipole matrix element between the ground state sublevel β and the excited state sublevel γ (of energy $\hbar\omega_\gamma$).

Given the analogy with electrons, in the following we shall focus on the case of atoms with $F = 1/2$. This case can be effectively realized using alkali atoms, cooling and manipulation of which have come a long way. In particular, ^{6}Li atoms have a ground state hyperfine component of $F = 1/2$. Similar features are expected to occur for higher values of the atomic spin F

as well.

In the $F = 1/2$ case, the external potential $V_{\alpha\beta}(\mathbf{r})$ can be simply written in terms of a fictitious magnetic field $\mathbf{B}(\mathbf{r})$ coupled to the total atomic angular momentum operator $\hat{\mathbf{F}}$:

$$V_{\alpha\beta}(\mathbf{r}) = V(\mathbf{r})\delta_{\alpha\beta} + \mathbf{B}(\mathbf{r}) \cdot \hat{\mathbf{F}}_{\alpha\beta}. \tag{4.78}$$

The scalar potential $V(\mathbf{r})$ is proportional to the local light intensity, while the vectorial field $\mathbf{B}(\mathbf{r})$ is proportional to the local electromagnetic spin:

$$V(\mathbf{r}) = b_0 \mathbf{E}^*(\mathbf{r}) \cdot \mathbf{E}(\mathbf{r}), \tag{4.79}$$

$$\mathbf{B}(\mathbf{r}) = -ib_1 \mathbf{E}^*(\mathbf{r}) \times \mathbf{E}(\mathbf{r}). \tag{4.80}$$

The proportionality coefficients $b_{0,1}$ depend on the details of the atomic structure as well as on the light frequency. As discussed in [143], an effective coupling to the fictitious magnetic field requires the detuning from the excited state to be smaller than the fine structure of the excited state. We shall give the specific experimental parameters later. Some consequences of the fictitious magnetic field have already been investigated from many different points of view, for instance Sisyphus cooling in resonant optical lattices [145], or NMR type experiments [146, 147]. The fictitious magnetic field was crucial for the observation of mesoscopic quantum tunneling in one-dimensional spin-dependent optical lattices [140].

4.3.2 Lattice configuration

We consider a 2D optical lattice created with three laser beams propagating in a plane with equal angles between them (see Fig. 4.11), a geometry already studied in the dissipative regime [148]. We however restrict our attention on the dissipationless case, as was done experimentally, for instance in [149] with Cesium atoms in one-dimensional configuration. We choose the polarization of the electric fields in such a way that the components respectively parallel and perpendicular to the plane are the same for all three beams

$$\mathbf{E}_i = (\alpha\hat{z} + \beta\hat{z} \times \hat{\mathbf{q}}_i)e^{i\mathbf{q}_i\mathbf{r}}; \tag{4.81}$$

the $\mathbf{q}_i$ are the wave vectors of the light beams, coefficients α and β are complex and $\hat{z}$ is the unit vector perpendicular to the plane. For this configuration, the scalar potential (4.79) and the fictitious magnetic field (4.80) are

$$\begin{aligned} V(\mathbf{r}) &= \sum_i V_0 \cos \mathbf{k}_i\mathbf{r}, \qquad (4.82)\\ \mathbf{B}(\mathbf{r}) &= \sum_i (V_1\hat{z}\sin \mathbf{k}_i\mathbf{r} + V_2\mathbf{k}_i \sin \mathbf{k}_i\mathbf{r} + V_3\hat{z} \times \mathbf{k}_i \cos \mathbf{k}_i\mathbf{r}), \end{aligned}$$

where $\mathbf{k}_1 = \mathbf{q}_2 - \mathbf{q}_3$, *etc.* and the amplitudes V_i are

$$V_0 = b_0\left(|\alpha|^2 + |\beta|^2\cos(2\pi/3)\right), \tag{4.83}$$

$$V_1 = 2b_1|\beta|^2\sin(2\pi/3), \tag{4.84}$$

$$V_2 = -4b_1\sin(\pi/3)\mathrm{Re}\left(\alpha^*\beta\right), \tag{4.85}$$

$$V_3 = 2b_1\mathrm{Im}\left(\alpha^*\beta\right). \tag{4.86}$$

In this subsection, we will use M, $(q\sqrt{3})^{-1}$ and $6E_r$ as the basic units of mass, length and energy respectively, where M is the mass of the atom, q_i is the light wave vector, and $E_r = \hbar^2 q^2/2M$ is the recoil energy. Experimentally, potentials with depths up to $20E_r$ are achievable in the dissipationless regime.

4.3.3 Effective Hamiltonian and Berry curvature

In what follows we are interested in the dynamics of an atomic distribution prepared in the lowest band of the potential. The different terms in the Hamiltonian proportional to the V_i are shown in Fig. 4.11. We consider the case in which $|V_0| \gg |V_1|, |V_2|, |V_3|$. Together with a direct numerical calculation of the band structure and Berry curvature (see Fig. 4.12), we consider a tight-binding model that allows us to obtain an effective Hamiltonian close to the Γ point. The scalar part of the potential creates a honeycomb lattice which is perturbed by the vector part. Introduction of the term with V_1 makes the lattice asymmetric for each spin component, similar to the one described in Section 4.1. V_2 and V_3 lead to hopping processes with simultaneous spin flipping. The tight-binding approach results in the effective Hamiltonian

$$\begin{pmatrix} \epsilon_A^{\uparrow} + h_0 & v & 0 & v_1 \\ v^* & \epsilon_B^{\uparrow} + h_0 & v_2 & 0 \\ 0 & v_2^* & \epsilon_A^{\downarrow} - h_0 & v \\ v_1^* & 0 & v^* & \epsilon_B^{\downarrow} - h_0 \end{pmatrix} \begin{matrix} |A,\uparrow\rangle \\ |B,\uparrow\rangle \\ |A,\downarrow\rangle \\ |B,\downarrow\rangle \end{matrix} . \tag{4.87}$$

Since lattices for different spins are mirror images of each other, the on-site energies for different spins are such that $\epsilon_A^{\uparrow} = -\epsilon_B^{\uparrow} = -\epsilon_A^{\downarrow} = \epsilon_B^{\downarrow}$. The off-

diagonal matrix elements are

$$\begin{aligned} v(\mathbf{k}) &= -t\left(1 + e^{i\mathbf{k}\mathbf{R}_1} + e^{i\mathbf{k}\mathbf{R}_2}\right), \\ v_1(\mathbf{k}) &= \tilde{t}\left(e^{-i\pi/3} + e^{i\pi/3}e^{i\mathbf{k}\mathbf{R}_1} - e^{i\mathbf{k}\mathbf{R}_2}\right), \\ v_2(\mathbf{k}) &= \tilde{t}\left(e^{-i\pi/3} + e^{i\pi/3}e^{-i\mathbf{k}\mathbf{R}_1} - e^{-i\mathbf{k}\mathbf{R}_2}\right), \end{aligned} \tag{4.88}$$

where t is proportional to the overlap of the wave functions in different sites with the same spin, $\tilde{t}$ is proportional to the overlap of wave functions at different sites with different spin, and $\mathbf{R}_i$ are the lattice primitive vectors (see Fig. 4.11). The coefficient t is determined by the scalar potential, while $\tilde{t}$ is governed mostly by V_3 terms (to the lowest order, terms with V_2 do not affect the dynamics, since the corresponding $\mathbf{B}$ field vanishes at the place where the overlap between on-site wave functions is the largest, see Fig. 4.11). The parameter h_0 describes an additional external field.

For vanishing fictitious magnetic field $\mathbf{B}$ and external field h_0, the bands have a two-fold spin degeneracy at all points of the Brillouin zone; at points K and K′, where bands cross, the degeneracy is four-fold. As the V_1 term is added, the bands keep the two-fold spin degeneracy, but the four-fold one at K and K′ is lifted and a gap is correspondingly opened. Spin degeneracy is then lifted by the inclusion of the V_3 term. The band degeneracies at the high symmetry points can be understood from the tight-binding model simply by looking at the properties of the off-diagonal matrix elements in (4.87). For instance, at the Γ point one has $v_{1,2} = 0$ and only $v \neq 0$, therefore the upper and lower bands are two-fold degenerate there. An effective Hamiltonian close to the Γ point can therefore be obtained simply by treating v_1 and v_2 as a perturbation.

The spectrum of the unperturbed Hamiltonian in the absence of the external field consists of two doubly degenerate states of energies

$$\epsilon_{\pm} = \pm\frac{1}{2}\sqrt{\left(\epsilon_B^{\uparrow} - \epsilon_A^{\uparrow}\right)^2 + 4|v(\mathbf{k})|^2}. \tag{4.89}$$

For small k around the Γ point, the dispersion is quadratic in k. The corresponding two lowest eigenvectors are of the form:

$$\begin{array}{l} |\uparrow,-\rangle = a\,|A,\uparrow\rangle + b\,|B,\uparrow\rangle\,, \\ |\downarrow,-\rangle = b\,|A,\downarrow\rangle + a\,|B,\downarrow\rangle\,. \end{array} \tag{4.90}$$

In the subspace spanned by these two eigenvectors, the effective Hamiltonian has the form:

$$H_{\Gamma}(\mathbf{k}) = \epsilon_{-}I + h_0\sigma_z - \gamma(k_y\sigma_x + k_x\sigma_y), \tag{4.91}$$

with v_1 and v_2 taken into account, σ_i are Pauli matrices and I is the unit matrix. This reduces to the standard form of the Rashba Hamiltonian if one makes a global spin-rotation about the σ_y axis to flip the signs of σ_x and σ_z. For the model discussed here, the value of the spin-orbit coupling parameter $\gamma = 0.08$ can be extracted from the relative slope of the two lowest eigenstates. A Hamiltonian of such a form has been recently predicted to give both AHE [81] and SHE [134–136] in solid state systems.

The simple analytic form of the Hamiltonian in (4.91) gives a simple expression for the Berry curvature which is responsible for AHE [77, 78, 81]

$$\Omega_z^{\uparrow/\downarrow} = \mp\frac{1}{2}\frac{\gamma^2 h_0}{\left(h_0^2 + \gamma^2 k^2\right)^{3/2}}. \tag{4.92}$$

The results of the Berry curvature calculation for the *continuous* potential in Eq. (4.82) are shown in Fig. 4.12. For $h_0 = 0$, the Berry curvature is zero

everywhere and singular at the points where the bands touch. Any finite value of the external field h_0 completely removes the degeneracy of the bands and makes the Berry curvature peaked around the Γ and K$'$ points with a finite maximum and width.

4.3.4 Observation of anomalous and spin Hall effects

An effect similar to AHE can therefore be observed with cold atoms: a wave packet initially prepared in the *lowest band* with a small quasimomentum spread $\Delta k \ll 1$ around the Γ point and accelerated in the ΓK direction performs Bloch oscillations in the direction of the drive and at the same time it drifts along the perpendicular direction because of the geometrical phase accumulated [1]. The spread in momentum mentioned above corresponds to a sub-recoil velocity distribution. Sub-recoil cooling techniques are reviewed in [150]. In Fig. 4.13 (a), we show the trajectory of the wave packet center calculated with semiclassical equations including the Berry curvature effects [77, 78]. The external force has been taken to be $f = 0.001$. In order to maximize the drift in a given time, the largest force that preserves adiabatic evolution in the first band has to be chosen in an actual experiment. The magnitude of the acceleration creating the force $\mathbf{f}$ is ~ 500 m/s^2, a value already demonstrated in the framework of optical lattices [14]. The chosen value of external field h_0 corresponds to ~ 1 mG. To observe a wave packet drift of

[1] For this direction, symmetry arguments guarantee that no transverse drift coming from the band asymmetry can occur.

$\sim 10\lambda$, the acceleration needs to be applied for ~ 50 ms.

To observe an effect similar to SHE with cold atoms, a *spin-sensitive* measurement of the wave packet momentum distribution after it was exposed to an external force has to be performed. The quasimomentum spread has to be small enough and the force applied for a short enough time, so that the wave packet stays within the region where (4.91) is valid. This region has a radius of the order of 0.2 around the Γ point. As discussed in [134–136] off-diagonal terms in Eq. (4.91) may be thought of as a momentum dependent magnetic field $\Delta_{\mathbf{k}} = -\gamma(k_y\hat{x} + k_x\hat{y})$. For $h_0 = 0$, the spins are initially parallel to the plane. As the external force is applied the center of the wave packet moves in momentum space and the spins are affected by changing momentum dependent magnetic field, $\Delta_{\mathbf{k}}(t)$. Their dynamics can be described by the Landau-Lifshitz equation [135]

$$\frac{\hbar d\hat{n}}{dt} = \hat{n} \times \Delta(t), \tag{4.93}$$

where $\hat{n}$ is the direction of the spin. As the center of the wave packet moves $\Delta_{\mathbf{k}}$ rotates in the plane, but in the opposite directions on opposite sides of the wave packet (left and right sides with respect to the motion). As a result, a non-vanishing z-component appear, i.e. spins "tilt vertically". For an atom with quasimomentum (k_x, k_y) and a force along the $\hat{x}$ direction $\mathbf{f} = f_x\hat{x}$, the z-component of the spin is:

$$n_{z,\mathbf{k}} = \frac{f_x k_y}{\gamma k^3}. \tag{4.94}$$

It is opposite on the opposite sides. This corresponds to spin current in the transverse direction.

For the momentum spread, we have taken $\Delta k_y = 0.1$, which corresponds to the minimum of the first band when $h_0 = 0$, and for the force $f = 10^{-4}$ ($\approx 50\text{m/s}^2$). For these values, we predict $n_{z,\mathbf{k}} = 0.125$. To measure the spin tilting in the vertical direction one should measure the momentum distribution of the different vertical spin components after the force has been applied. Spin dynamics can be frozen by suddenly switching on an external magnetic field $h_0 \gg \gamma\Delta k$. The lattice potential is then adiabatically removed: this transforms the quasimomentum distribution into a true momentum distribution so that SHE can be observed as the motion of the different spin z-components in opposite directions along the y axis.

4.3.5 Estimation of experimental parameters

Finally, we estimate the required experimental parameters. If we write the vertical and horizontal components of the polarization as

$$\alpha = |\alpha|\, e^{i\phi_\alpha}, \tag{4.95}$$

$$\beta = |\beta|\, e^{i\phi_\beta}, \tag{4.96}$$

then the Eq. (4.85) requires that

$$\phi = \phi_\alpha - \phi_\beta = \frac{\pi}{2}. \tag{4.97}$$

From the ratio of Eq. (4.84) and Eq. (4.86) we obtain

$$\frac{|\alpha|}{|\beta|} = \sin\frac{2\pi}{3}\frac{V_3}{V_1} = 0.866 \tag{4.98}$$

and from the ratio of Eq. (4.83) and Eq. (4.84) we obtain the required ratio of the coefficients b_0 and b_1

$$\frac{V_0}{V_1} = \frac{b_0}{2b_1 \sin\frac{2\pi}{3}} \left(\frac{|\alpha|^2}{|\beta|^2} + \cos\frac{2\pi}{3} \right), \tag{4.99}$$

$$\frac{b_0}{b_1} = \frac{V_0}{V_1} 2\sin\frac{2\pi}{3} \left(\left(\frac{V_3}{V_1} \sin\frac{2\pi}{3} \right)^2 + \cos\frac{2\pi}{3} \right)^{-1} = 69.3, \tag{4.100}$$

the values here are for the amplitudes $V_0 = 1, V_1 = V_3 = 0.1, V_2 = 0$.

Coupling of orbital angular momentum of an atom's electron to its spin is responsible for fine structure in the spectra of the element. For a fictitious magnetic field to be substantial, detuning should be not too large in comparison to the fine splitting. The radiation couples to orbital momentum of the electron and only through spin-orbit interaction to its spin. When the detuning is too large in comparison to the splitting it is not relevant and light does not effect the spin.

In alkalies, the orbital electron's spin-orbit coupling produces two lines D_1 and D_2. The ground state in alkalies has total angular momentum of the electron $J = L+S = 1/2$, since the spin is $S = 1/2$ and orbital momentum $L = 0$. The two correspond to transition which is in the central field approximation corresponds to $L = 1$. The D_1 line corresponds to transition from the excited state with $J = 1/2$ and the D_2 line to the transition from $J = 3/2$. The polarizability tensor of the D_1 line is (see Appendix C)

$$\hat{\alpha}_{ij,1} = \alpha \left(\frac{2}{3}\delta_{ij}\hat{I} - \frac{i}{3}\varepsilon_{ijk}\hat{\sigma}_k \right), \tag{4.101}$$

and polarizability of the D_2 line is

$$\hat{\alpha}_{ij,2} = \alpha \left(\frac{1}{3}\delta_{ij}\hat{I} + \frac{i}{3}\varepsilon_{ijk}\hat{\sigma}_k \right), \tag{4.102}$$

here characteristic polarizability $\tilde{\alpha}$ can be defined in terms of the dipole operator reduced matrix element $\langle J \,\|d\|\, J' \rangle$ [149], since we are interested in ratio of the coefficients b_0 and b_1 its explicit form is not relevant. From the expression for the polarizabilities we obtain expressions for the coefficients with dependence on detuning given by

$$b_{0,\mathrm{tot}} = -\frac{U_1}{3}\left(\frac{2}{\Delta_2} + \frac{1}{\Delta_1} \right), \tag{4.103}$$

$$b_{1,\mathrm{tot}} = -\frac{2U_1}{3}\left(\frac{1}{\Delta_2} - \frac{1}{\Delta_1} \right), \tag{4.104}$$

here Δ_1 and Δ_2 are detunings from the D_1 and D_2 lines respectively. The ratio b_1/b_0 vanishes for detunings much larger than the fine splitting, i.e. the fictitious magnetic field becomes small in comparison to the scalar potential.

Taking parameters of ^{6}Li [151], we obtain the detuning from the D_2 line resonance

$$\Delta_2 = \frac{2}{3}\Delta\left(\frac{b_0}{b_1} - 1 \right) = 458 \text{ GHz}, \tag{4.105}$$

where $\Delta = 10.056$ GHz is the fine splitting. To estimate necessary intensity, we may use the expression for depth of the optical potential given in [4]:

$$U_{\mathrm{dip}} = \frac{\pi c^2 \Gamma}{2\omega_0^3}\left(\frac{2 + P g_F m_F}{\Delta_{2,F}} + \frac{1 - P g_F m_F}{\Delta_{1,F}} \right) I(\mathbf{r}). \tag{4.106}$$

For the sake of estimation we take linear polarization ($P = 0$) and obtain

$$I = 77.4 \ \frac{\mathrm{mW}}{\mathrm{cm}^2}. \tag{4.107}$$

The maximum scattering rate is estimated based on another equation from [4]

$$\Gamma_{sc} = \frac{\pi c^2 \Gamma^2}{2\hbar\omega_0^3}\left(\frac{2}{\Delta_2^2} + \frac{1}{\Delta_1^2}\right) I = 223 \text{ s}^{-1} \tag{4.108}$$

Even with this number the number of scattered photons would less than 10 during 50 ms – the estimated duration of the drift experiment. Since the lattice is blue detuned, the atoms are located in the regions of space where the intensity is smaller than maximum. The scattering rate at the distances from the center of the wells equal to Harmonic oscillator length given by the strength of potential ($\approx 6E_{\text{rec}}$) approximately order of magnitude smaller.

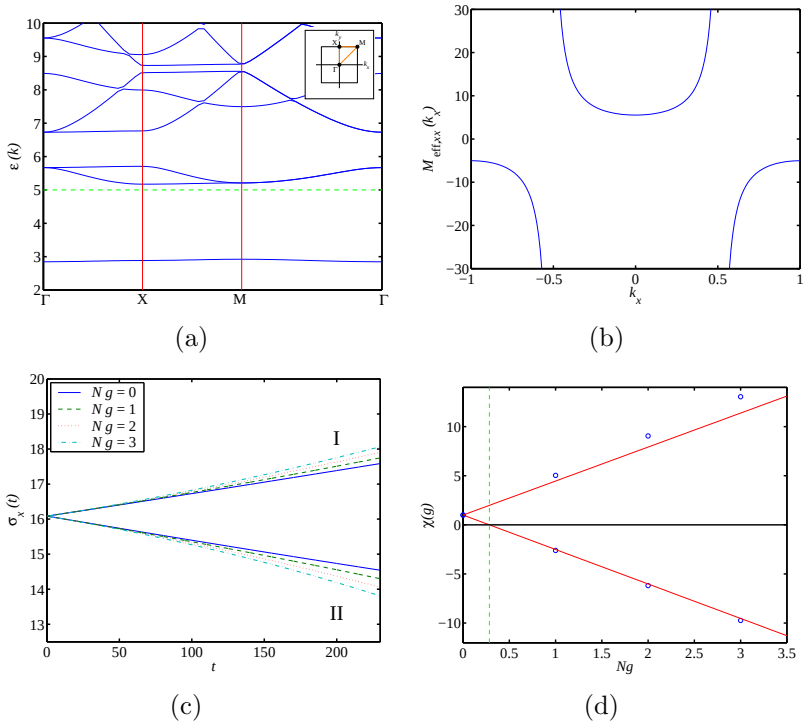

Figure 4.7: (a) Dispersion for square lattice potential (4.66) along the high symmetry path. The green dashed line shows the boundary between strongly bound and quasi-unbound states [110]. (b) xx component of the effective mass tensor along k_x-axis. (c) Dependence of wave packet dispersion on time after the lattice potential is introduced. The two sets of curves are for different points in Brillouin zone: (I) - point Γ, (II) - point M. (d) Dispersive characteristic χ from (4.75). The blue dots are obtained from fitting quadratic dispersion (4.47) to continuous simulation data from panel (c), red line is expected behavior of χ.

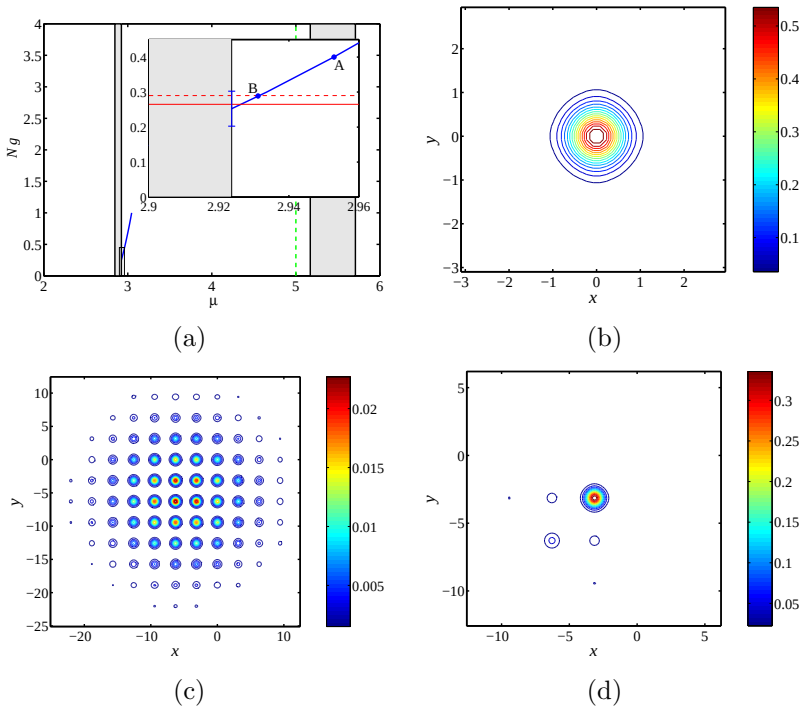

Figure 4.8: (a) - Dependence of nonlinearity on corresponding chemical potential. The first and second bands are shown with solid rectangles. The inset shows a region denoted by a rectangle in the lower left corner. The horizontal solid line shows numerical value for delocalizing nonlinearity, $g_{\rm num}$, the dashed line is the critical nonlinearity for extended Gaussian wave packet to collapse $g_{2,c}$. (b) - Spatial distribution of discrete soliton corresponding to $\mu = 0.7$ obtained with the descent method. (c) - Probability distribution for BEC wave function evolved with $Ng_2 = 0.2$ for $\Delta t \sim 1500$ after it was driven to M point. (d) - The same for $Ng = 0.4$ (point A in (a)), approximately 0.72 of the wave function probability is transferred to the soliton, which corresponds to an effective nonlinearity of $Ng_{2,\rm eff} \approx 0.288$ - at the top of the first band (point B in (a)).

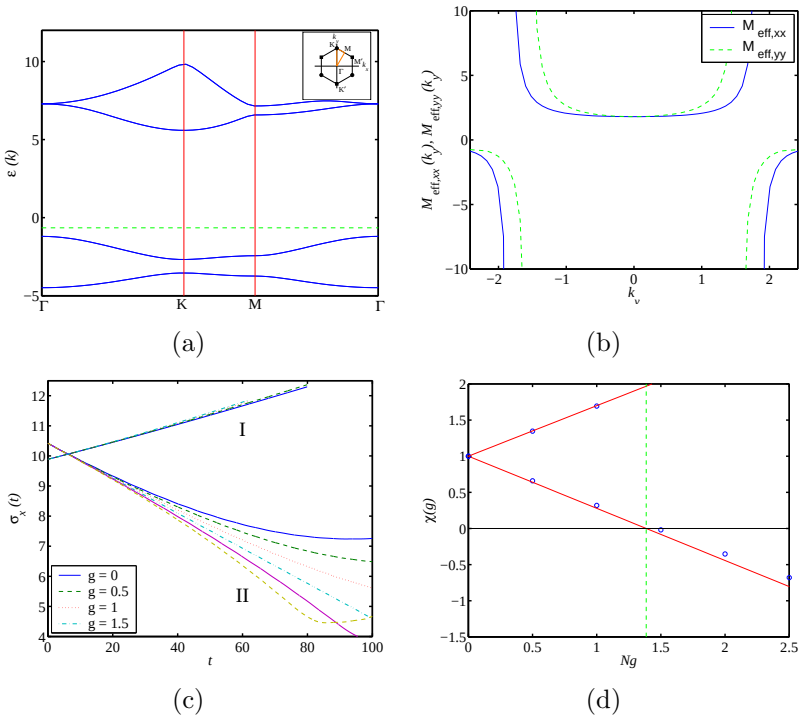

Figure 4.9: (a) Dispersion for asymmetric honeycomb potential (4.32) along high symmetry path. The green dashed line shows boundary between strongly bound and quasi-unbound states [110]. (b) - xx, and yy components of effective mass tensor along k_y-axis. (c) - Dependence of wave packets dispersion on time after the lattice potential is introduced. The two sets of curves are for different points in Brillouin zone: (I) - point Γ, (II) - point K. (d) - Dispersive characteristic χ from (4.75). The blue dots are obtained from fitting quadratic dispersion (4.47) to continuous simulation data from panel (c), red line is expected behavior of χ.

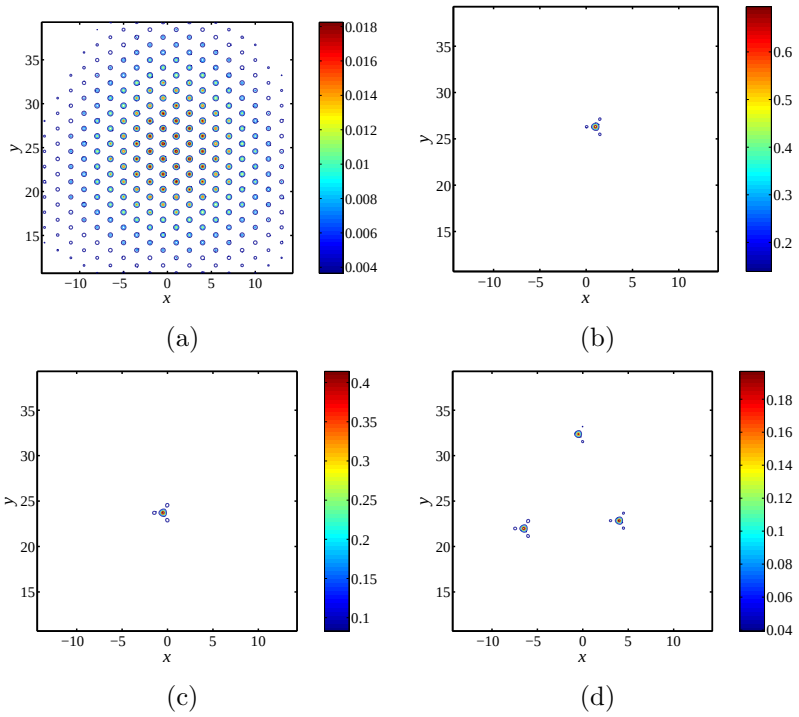

Figure 4.10: Probability density of the wave packet that has been driven to K point of square lattice after expansion for $\Delta t_{\text{exp}} = 200$ with different interactions: (a) - $Ng_2 = 0.5$, (b) - $Ng_2 = 2.5$ (c) - $Ng_2 = 5$ (d) - $Ng_2 = 10$. As the interaction increases fraction of the wave function transferred to solitons decreases.

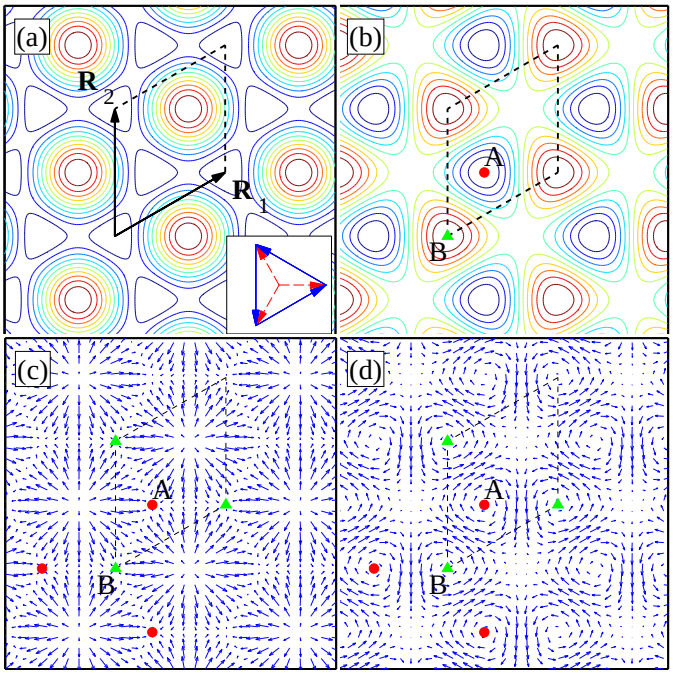

Figure 4.11: Spatial profile of the different terms of the potential (4.82): (a) V_0 term, (b) V_1 term, (c) V_2 term, (d) V_3 term. The amplitude of a vector component is proportional to the length of the arrow. The inset in panel (a) shows the configuration of the laser wave vectors $\mathbf{q}_i$ (dashed arrows) and the lattice vectors $\mathbf{k}_i$ (solid arrows). Dots indicate wells A, triangles indicate wells B. Dashed lines show a unit cell.

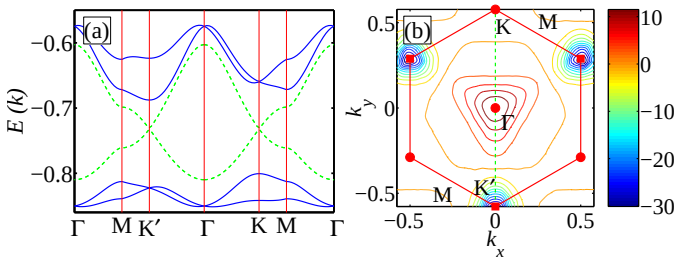

Figure 4.12: (a) Dispersion of the lowest four bands in the potential (4.82). The dashed line corresponds to the case in which only a scalar potential is present, $V_0 = 1$. The solid line is for the case $V_0 = 1$, $V_1 = V_3 = 0.1$ and $V_2 = 0$ (b) Berry curvature for the lowest band in the presence of an external field $h_0 = 0.005$. The band structure in the presence of h_0 is essentially the same as shown in (a), except for a splitting by ≈ 0.01 at the degeneracy points Γ, K and K′.

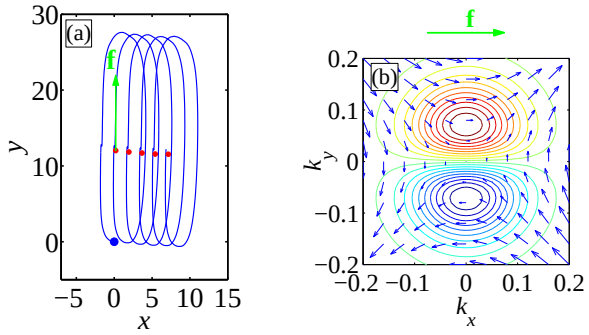

Figure 4.13: (a) AHE. Trajectory of the wave packet center for a force $\mathbf{f}$ in the positive y direction. Small dots are period-averaged positions. The initial position is indicated by the large dot in the origin. (b) SHE. Distribution of the spin vertical component as a function of momentum when finite force $\mathbf{f} = f_x\hat{x}$ is applied. Spin is positive for $k_y > 0$, and negative for $k_y < 0$. The arrows show an effective momentum dependent field $\Delta_{\mathbf{k}}$ close to the Γ point.

Appendices

Appendix A

Expressions for compression and rate of compression

Here we show how analytic expression for phase space compression in case of stationary wall Eq. (2.2) and Eq. (2.5) for captured fraction are obtained.

A.1 Compression

The definition of the phase space compression we used in the text is

$$C = \frac{l_1 + l_2}{l_2} \frac{\sigma_v}{\sigma_{v,\text{final}}}. \tag{A.1}$$

Final distribution in velocity is given by originally trapped atoms and those that are trapped after a single recoil kick

$$g_{\text{final}}(v) = \frac{l_1}{l_1 + l_2} g_{\text{init}}(v) + \frac{l_2}{l_1 + l_2} g_{\text{kick}}(v). \tag{A.2}$$

Initial velocity distribution is

$$g_{\text{init}}(v) = \frac{1}{\sqrt{2\pi}\sigma_v} e^{-\frac{v^2}{2\sigma_v^2}}. \tag{A.3}$$

Velocity distribution for the fraction that experiences the recoil kick is

$$g_{\text{kick}}(v) = \int g_{\text{init}}(v')\Delta(v, v')dv', \tag{A.4}$$

with redistribution function of the kick

$$\Delta_{\text{kick}}(v) = \frac{1}{\sqrt{2\pi}\sigma_v}\frac{1}{2}\left[\delta\left((v-v') - v_r\right) + \delta\left((v-v') + v_r\right)\right]. \tag{A.5}$$

In the model we have neglected 3D nature of the photon recoil, this should only overestimate limiting values of phase space compression. Thus after the kick velocity distribution is

$$g_{\text{kick}}(v) = \frac{1}{\sqrt{2\pi}\sigma_v}\frac{1}{2}\left[e^{-\frac{(v-v_r)^2}{2\sigma_v^2}} + e^{-\frac{(v+v_r)^2}{2\sigma_v^2}}\right]. \tag{A.6}$$

Calculating the distribution's dispersions

$$\begin{array}{l} \bar{v}_{\text{final}} = 0, \\ \sigma_v^2 = \overline{v^2} - \bar{v}^2, \\ \overline{v_1^2} = \sigma_v^2, \overline{v_2^2} = \overline{v_3^2} = \sigma_v^2 + v_r^2, \\ \sigma_{v,\text{final}}^2 = \overline{v^2} = \frac{l_2}{l_1+l_2}\sigma_v^2 + \frac{l_1}{l_1+l_2}\left(\sigma_v^2 + v_r^2\right) = \sigma_v^2 + \frac{l_1}{l_1+l_2}v_r^2, \end{array} \tag{A.7}$$

and substituting them to Eq. A.1, we obtain the expression for C given in the text.

A.2 Rate of Compression

First we obtain the Eq. 2.5 for fraction of atoms trapped after certain time t This fraction is given by

$$f(t) = f_0 + \int_0^\infty f(v,t)g\left(|v|\right)dv, \tag{A.8}$$

where $f(v,t)$ is the fraction of particles that have crossed the wall and have magnitude of the velocity in the range

$$|v| - |v| + dv, \tag{A.9}$$

$$f(v,t) = \frac{\min(vt, 2l_1)}{2l_1}. \tag{A.10}$$

Initial distribution in magnitude is

$$g(|v|) = \frac{2}{\sqrt{2\pi}\sigma_v} e^{-\frac{v^2}{2\sigma_v^2}}. \tag{A.11}$$

Explicit expression for fraction transfered for all velocities is

$$f(t) = f_0 + \int_0^{v_0(t)} \frac{tv}{2l_1} \frac{2}{\sqrt{2\pi}\sigma_v} e^{-\frac{v^2}{2\sigma_v^2}} dv + \int_{v_0(t)}^{\infty} \frac{2}{\sqrt{2\pi}\sigma_v} e^{-\frac{v^2}{2\sigma_v^2}} dv, \tag{A.12}$$

here $v_0 = 2l_1/t$ and when we define $\tilde{v}_0 = \frac{v_0}{\sigma_v}$ the equation becomes

$$f_0 - f + \tilde{v}_0 \sqrt{\frac{2}{\pi}} \int_0^{\tilde{v}_0} v e^{-\frac{v^2}{2}} dv + \sqrt{\frac{2}{\pi}} \int_{\tilde{v}_0}^{\infty} e^{-\frac{v^2}{2}} dv = 0. \tag{A.13}$$

With error function and complimentary error functions defined as

$$\begin{aligned} \mathrm{erf}(x) &= \tfrac{2}{\sqrt{\pi}} \int_0^x e^{-t^2} dt \\ \mathrm{erfc}(x) &= 1 - \mathrm{erf}(x) \end{aligned} \tag{A.14}$$

we obtain Eq. 2.5. Using the series expansion for error function

$$\mathrm{erf}(x) = \frac{2}{\sqrt{\pi}} \left(x - \frac{x^3}{3} + \ldots \right) \tag{A.15}$$

we obtain the linearized equation the solution of which gives Eq. 2.6.

Appendix B

Expressions for compression in a trap

We obtain ratio of phase space volumes of two classical systems of N atoms in the same trap for different average energies per particle $\bar{e}_1$ and $\bar{e}_2$ that are proportional to corresponding temperatures. The strategy is as following: we obtain entropy S from the free energy F and relate it to total energy E [36].

Starting with general expression for free energy

$$F = -NT \ln \frac{e}{N} \int e^{-\varepsilon(p,q)/k_B T} d\tau. \tag{B.1}$$

For a specific case of 1D potential

$$V(q) = Aq^n. \tag{B.2}$$

Using some intermediate formulas

$$\varepsilon(p,q) = \frac{p^2}{2m} + V(q), \tag{B.3}$$

$$\int_{-\infty}^{\infty} \frac{p^2}{2m} e^{-\frac{p^2}{2m}\frac{1}{k_B T}} dp = k_B T \sqrt{2mk_B T} \int x^2 e^{-x^2} dx, \tag{B.4}$$

$$\int_{-\infty}^{\infty} Aq^n e^{-Aq^n \frac{1}{k_B T}} dp = k_B T \left(\frac{k_B T}{A}\right)^{1/n} \int x^n e^{-x^n} dx. \tag{B.5}$$

Free energy is

$$\begin{array}{c} F = -Nk_B T \ln \frac{e}{N} \sqrt{2mk_B T \pi} C \left(\frac{k_B T}{A}\right)^{1/n} = \\ -Nk_B T \ln B T^{1/2+1/n} = \\ -Nk_B T \ln B - Nf(T). \end{array} \tag{B.6}$$

Where $f(T)$ is the function defined as

$$f(T) = T \ln T^{1/2+1/n}. \tag{B.7}$$

Here and later A, B, C are some numerical constant that will be irrelevant in the answer. Entropy is

$$S = -\frac{\partial F}{\partial T} = Nk_B \ln B - Nf'(T). \tag{B.8}$$

Energy

$$\begin{gathered} E = F + TS = k_B \left(Nf(T) - NTf'(T)\right), \\ f'(T) = Nk_B T \left(1/2 + 1/n\right), \\ E = Nk_B T(1/2 + 1/n). \end{gathered} \tag{B.9}$$

Difference in entropy

$$S_1 - S_2 = -Nk_B \left(f'(T_1) - f'(T_2)\right) = Nk_B \ln \left(\frac{T_1}{T_2}\right)^{1/n+1/2}. \tag{B.10}$$

Compression in phase space

$$\frac{\Gamma_2}{\Gamma_1} = e^{\frac{S_2 - S_1}{k_B N}} = \left(\frac{T_1}{T_2}\right)^{1/n+1/2} = \left(\frac{E_1}{E_2}\right)^{1/n+1/2}. \tag{B.11}$$

Appendix C

Polarization tensor for D_1 line

We illustrate how the polarizability tensor can be obtained for D_1 line following steps similar to [149] where it is shown how to obtain it for D_2 line.

Since the operator must act on two-dimensional Hilbert state the general form of the tensor is

$$\bar{\alpha}_{ij} = \frac{1}{3}\delta_{ij}\mathrm{Tr}\left(\hat{\mathbf{D}}^{\dagger}\hat{\mathbf{D}}\right)\frac{\hat{I}}{2} + \frac{1}{2}\varepsilon_{ijk}\left(\hat{\mathbf{D}}^{\dagger}\times\hat{\mathbf{D}}\right). \tag{C.1}$$

To obtain explicit form of the coefficient the same symmetry arguments as in [149]. To calculate the trace of the scalar product only trace of one component needs to be calculated

$$\mathrm{Tr}\left(\hat{\mathbf{D}}^{\dagger}\hat{\mathbf{D}}\right) = 3\mathrm{Tr}\left(\hat{D}_z^{\dagger}\hat{D}_z\right). \tag{C.2}$$

The vector product is anti-Hermitian as a result it must have the form

$$\left(\hat{\mathbf{D}}^{\dagger}\times\hat{\mathbf{D}}\right)_k = iC\hat{\sigma}_k, \tag{C.3}$$

where the coefficient C may be evaluated by decomposing one of the components explicitly

$$\left(\hat{\mathbf{D}}^{\dagger}\times\hat{\mathbf{D}}\right)_z = -i\left(\hat{D}_+^{\dagger}\hat{D}_+ - \hat{D}_-^{\dagger}\hat{D}_-\right). \tag{C.4}$$

$m \downarrow \mid q \rightarrow$	-1	0	1
$-\frac{1}{2}$	0	$-\frac{1}{\sqrt{3}}$	$-\sqrt{\frac{2}{3}}$
$\frac{1}{2}$	$\sqrt{\frac{2}{3}}$	$\frac{1}{\sqrt{3}}$	0

Table C.1: Values of the Clebsch-Gordan coefficients

To proceed with the steps outlined above we use the definition of the operator $\hat{\mathbf{D}}$

$$\hat{D}_i = \sum_{m,q} \mathbf{e}_i \cdot \varepsilon_q^* c_m^{m+q} \left| J', m+q \right\rangle \left\langle J, m \right|, \tag{C.5}$$

where the coefficients c_m^{m+q} are Clebsch-Gordan coefficients of the angular momentum sum of the ground state angular momentum and the angular momentum of a photon

$$\mathbf{J} + \mathbf{1} = \mathbf{J}', \tag{C.6}$$

$$c_m^{m+q} = \left\langle J, 1; m, q \mid J, 1; J', m+q \right\rangle. \tag{C.7}$$

Their explicit values for the transition of interest are given in the Table C.1. Thus the dipole moment components are

$$D_z = -\frac{1}{\sqrt{3}} \left| -\frac{1}{2} \right\rangle \left\langle -\frac{1}{2} \right| + \frac{1}{\sqrt{3}} \left| +\frac{1}{2} \right\rangle \left\langle +\frac{1}{2} \right|, \tag{C.8}$$

$$D_+ = -\sqrt{\frac{2}{3}} \varepsilon_+ \left| +\frac{1}{2} \right\rangle \left\langle -\frac{1}{2} \right|, \tag{C.9}$$

$$D_- = \sqrt{\frac{2}{3}} \varepsilon_- \left| -\frac{1}{2} \right\rangle \left\langle +\frac{1}{2} \right|, \tag{C.10}$$

where all the states are in the form

$$\left| J' = 1/2, m+q \right\rangle \left\langle J = 1/2, m \right|. \tag{C.11}$$

As a result

$$\mathrm{Tr}\left(\hat{\mathbf{D}}^{\dagger}\hat{\mathbf{D}}\right) = 2, \tag{C.12}$$

$$\left(\hat{\mathbf{D}}^{\dagger} \times \hat{\mathbf{D}}\right)_z = -i\left(\hat{D}_+^{\dagger}\hat{D}_+ - \hat{D}_-^{\dagger}\hat{D}_-\right) = \frac{2}{3}i\sigma_k, \tag{C.13}$$

$$\alpha_{ij}\left(J = 1/2 \rightarrow J' = 1/2\right) = \tilde{\tilde{\alpha}}\left(\frac{1}{3}\delta_{ij}\hat{I} + \frac{i}{3}\varepsilon_{ijk}\hat{\sigma}_k\right), \tag{C.14}$$

note that in these expressions the labels are only for m of the ground state.

Bibliography

[1] C. Cohen-Tannoudji, J. Dupont-Roc, and G. Grynberg. *Atom-Photon Interaction: Basic Processes and Applications*. Wiley, New York, 1992.

[2] R. Loudon. *The Quantum Theory of Light*. Oxford University Press, Oxford, 3rd edition, 2000.

[3] H. J. Metcalf and P. van de Straten. *Laser Cooling and Trapping*. Springer-Verlag, New York, 1999.

[4] R. Grimm, M. Weidemuller, and Yu.B. Ovchinnikov. *Adv. At. Mol. Opt. Phys.*, 42:95, 2000.

[5] P. Meystre. *Atom Optics*. Springer-Verlag, New York, 2001.

[6] J.D. Jackson. *Classical Electrodynamics*. John Wiley & Sons, 3rd edition, 1998.

[7] C. Cohen-Tannoudji and J. Dupont-Roc. *Phys. Rev. A*, 5:968, 1972.

[8] M.H. Anderson, J.R. Ensher, M.R. Matthews, C.E. Wieman, and E.A. Cornell. *Science*, 269:198, 1995.

[9] K.B. Davis, M.-O. Mewes, M.A. Joffe, M.R. Andrews, and W. Ketterle. *Phys. Rev. Lett.*, 74:5202, 1995.

[10] C.C. Bradley, C.A. Sackett J.J. Tollett, and R.G. Hulet. *Phys. Rev. Lett.*, 75:1687, 1995.

[11] C.J. Pethick and H. Smith. *Bose-Einstein Condensation in Dilute Gases*. Cambridge University Press, Cambridge, 2001.

[12] D.S. Petrov, M. Holzmann, and G.V. Shlyapnikov. *Phys. Rev. Lett.*, 84:255, 2000.

[13] A. Görlitz, J.M. Vogels, A.E. Leanhardt, C. Raman, T.L. Gustavson, J.R. Abo-Shaeer, A.P. Chikkatur, S. Gupta, S. Inouye, T. Rosenband, and W. Ketterle. *Phys. Rev. Lett.*, 87:130402, 2001.

[14] M. Raizen, C. Salomon C, and Q. Niu. *Physics Today*, 50 (7):30, 1997.

[15] R.B. Diener, B. Wu, M.G. Raizen, and Q. Niu. *Phys. Rev. Lett.*, 89:070401, 2002.

[16] A.M. Dudarev, R.B. Diener, B. Wu, and Q. Niu. *Phys. Rev. Lett.*, 91:010405, 2003.

[17] C. Lovelace C., C. Mehanian, T.J. Tommila, and D.M. Lee. *Nature*, 318:30, 1985.

[18] H.F. Hess. *Phys. Rev. B*, 34:3476, 1986.

[19] T. Tomilla. *Europhys. Lett.*, 2:789, 1986.

[20] M.G. Raizen, A.M. Dudarev, Q. Niu, and N.J. Fisch. *Phys. Rev. Lett.*, 94:053003, 2005.

[21] A.M. Dudarev, M. Marder, Q. Niu, and N.J. Fisch. physics/0502056, submitted to Europhys. Lett.

[22] R. Kaiser N. Vansteenkiste C. Cohen-Tannoudji A. Aspect, E. Arimondo. *Phys. Rev. Lett.*, 61:826, 1988.

[23] M. Kasevich and S. Chu. *Phys. Rev. Lett.*, 69:1740, 1992.

[24] W. Ketterle, K. B. Davis, M. A. Joffe, A. Martin, and D. E. Pritchard. *Phys. Rev. Lett.*, 70:2253, 1993.

[25] G. Morigi, J. I. Cirac, K. Ellinger, and P. Zoller. *Phys. Rev. A*, 57:2909, 1998.

[26] A. T. Black H. W. Chan and V. Vuletić. *Phys. Rev. Lett.*, 90:063003, 2003.

[27] W. Petrich, M.H. Anderson, J.R. Ensher, and E.A. Cornell. *Phys. Rev. Lett.*, 74:3352, 1995.

[28] C.J. Myatt, E.A. Burt, R.W. Ghrist E.A. Cornell, and C.E. Wieman. *Phys. Rev. Lett.*, 78:586, 1997.

[29] B. DeMarco and D.S. Jin. *Science*, 285:1703, 1999.

[30] A. Ruschhaupt and J.G. Muga. *Phys. Rev. A*, 70:0601604, 2004.

[31] J. M. Doyle, B. Friedrich, J. Kim, and D. Patterson. *Phys. Rev. A*, 52:R2515, 1995.

[32] J. D. Weinstein, R. deCarvalho, T. Guillet, B. Friedrich, and J. Doyle. *Nature*, 395:148, 1998.

[33] G. Berden H. L. Bethlem and G. Meijer. *Phys. Rev. Lett.*, 83:1558, 1999.

[34] M. Gupta and D. R. Herschbach. *J. Phys. Chem. A*, 105:1626, 2001.

[35] L.D. Landau and E.M. Lifshitz. *Mechanics*. Nauka, Moscow, 1988.

[36] L.D. Landau and E.M. Lifshitz. *Statistical Mechanics*. Fizmatlit, Moscow, 2002.

[37] W. Ketterle and D.E. Pritchard. *Phys. Rev. A*, 46:4051, 1992.

[38] M. Abramowitz and I.A. Stegun, editors. *Handbook of Mathematical Functions*. Dover, New York, 1970.

[39] N.J. Fisch, J.M. Rax, and I.Y. Dodin. *Phys. Rev. Lett.*, 91:205004, 2003.

[40] N.J. Fisch. *Rev. Mod. Phys.*, 59:175, 1987.

[41] J.L. Hanssen. PhD thesis, University of Texas at Austin, 2004.

[42] T.P. Meyrath. PhD thesis, University of Texas at Austin, 2005.

[43] D. Frese, B. Ueberholz, S. Kuhr, W. Alt, D. Schrader, V. Gomer, and D. Meschede. *Phys. Rev. Lett.*, 85:3777, 2000.

[44] R.B. Diener. PhD thesis, University of Texas at Austin, 2003.

[45] T.P. Meyrath, F. Schreck, J.L. Hanssen, C.-S. Chuu, and M.G. Raizen. cond-mat/0503349.

[46] M.L. Chiofalo, S. Succi, and M.P. Tosi. *Phys. Rev. E*, 62:7438, 2000.

[47] L.D. Landau. *Phys. Z. Sowejetunion*, 2:46, 1932.

[48] G. Zener. *Proc. R. Soc. A*, 137:696, 1932.

[49] J.S. Bell. *Physics*, 1:195, 1964.

[50] J. Clauser and S. Freedman. *Phys. Rev. Lett.*, 28:938, 1972.

[51] A. Aspect, J. Dallibard, and G. Roger. *Phys. Rev. Lett.*, 49:1804, 1982.

[52] J.G. Rarity and P.R. Tapster. *Phys. Rev. Lett.*, 64:2495, 1990.

[53] J.-W. Pan, D. Bouwmeester, M. Daniell, H. Weinfurter, and A. Zeilinger. *Nature*, 403:515, 2000.

[54] D.M. Greenberger, M.A. Horne, and A. Zeilinger. *Physics Today*, 46, 8.

[55] R. Ghosh and L. Mandel. *Phys. Rev. Lett.*, 59:1903, 1987.

[56] C.A. Sackett, D. Kielpinski, B.E. King, C. Langer, V. Meyer, C. J. Myatt, M. Rowe, Q. A. Turchette, W. M. Itano, D. J. Wineland, and C. Monroe. *Nature*, 404:256, 2000.

[57] R. Laflamme, E. Knill, W.H. Zurek, P. Catasti, and S.V.S Mariappan. *Phil. Trans. R. Soc. Lond. A*, 356:1941, 1998.

[58] J. I. Cirac C. W. Gardiner D. Jaksch, H.-J. Briegel and P. Zoller. *Phys. Rev. Lett.*, 82:1975, 1999.

[59] E. Andersson and S. M. Barnett. *Phys. Rev. A*, 62:052311, 2000.

[60] T. Calarco, E.A. Hinds, D. Jaksch, J. Schmiedmayer, J.I. Cirac, and P. Zoller. *Phys. Rev. A*, 61:022304, 2000.

[61] H. Pu and P. Meystre. *Phys. Rev. Lett.*, 85:3987, 2000.

[62] L.-M. Duan, A. Sørensen, J.I. Cirac, and P. Zoller. *Phys. Rev. Lett.*, 85:3991, 2000.

[63] J.I. Cirac A. Sø rensen, L.-M. Duan and P. Zoller. *Nature*, 409:63, 2001.

[64] N. Schlosser, G. Reymond, I. Protsenko, and P. Grangier. *Nature*, 411:1024, 2001.

[65] A.J. Moerdijk, B.J. Verhaar, and A. Axelsson. *Phys. Rev. A*, 51:4852, 1995.

[66] S. Inouye, M. R. Andrews, J. Stenger, H.-J. Miesner, D. M. Stamper-Kurn, and W. Ketterle. *Nature*, 392:151, 1998.

[67] Ph. Courteille, R.S. Freeland, D. J. Heinzen, F. A. van Abeelen, and B. J. Verhaar. *Phys. Rev. Lett.*, 81:69, 1998.

[68] E. Andersson, M.T. Fontenelle, and S. Stenholm. *Phys. Rev. A*, 59:3841, 1999.

[69] J. Schmiedmayer. *Phys. Rev. A*, 52:R13, 1995.

[70] J. Reichel, W. Hänsel, and T. W. Hänsch. *Phys. Rev. Lett.*, 83:3398, 1999.

[71] M.A. Ol'Shanii, Y.B. Ovchinnikov, and V.S. Letokhov. *Opt. Commun.*, 98:77, 1993.

[72] S. Marksteiner, C. M. Savage, P. Zoller, and S. L. Rolston. *Phys. Rev. A*, 50:2680, 1994.

[73] M.J. Renn, D. Montgomery, O. Vdovin, C.E. Wieman D.Z. Anderson, and E. A. Cornell. *Phys. Rev. Lett.*, 75:3253, 1995.

[74] G. Birkl, F.B.J. Buchkremer, R. Dumke, and W. Ertmer. *Opt. Commun.*, 191:67, 2001.

[75] F.A. van Abeelen and B.J. Verhaar. *Phys. Rev. A*, 59:578, 1999.

[76] N. W. Ashcroft and N. D. Mermin. *Solid State Physics*. Saunders, Philadelphia, 1976.

[77] Ming-Che Chang and Qian Niu. *Phys. Rev. B*, 53:7010, 1996.

[78] Ganesh Sundaram and Qian Niu. *Phys. Rev. B*, 59:14915, 1999.

[79] Ganesh Sundaram. PhD thesis, University of Texas at Austin, 2000.

[80] T. Jungwirth, Q. Niu, and A.H. MacDonald. *Phys. Rev. Lett.*, 88:207208, 2002.

[81] D. Culcer, A. H. MacDonald, and Q. Niu. *Phys. Rev. B*, 68:045327, 2003.

[82] Y. Yao, L. Kleinman, A. H. MacDonald, J. Sinova, T. Jungwirth, D. Wang, E. Wang, and Q. Niu. *Phys. Rev. Lett.*, 92:037204, 2004.

[83] A. Okamoto, T. Yoshida, S. Muramatsu, and I. Shibasaki. *J. Cryst. Growth*, 201:765, 1999.

[84] A.Y. Liu, R.M. Wentzcovitch, and M.L. Cohen. *Phys. Rev. B*, 39:1760, 1989.

[85] M.P. Marder. *Condensed Matter Physics*. John Wiley & Sons, New York, 2000.

[86] R.B. Diener, A.M. Dudarev, G. Sundaram, and Q. Niu. cond-mat/0306184, 2003.

[87] B. Jackson and E. Zaremba. cond-mat/0205421, 2002.

[88] A.S. Davydov and N.I. Kislukha. *Phys. Status Solidi*, 59:465, 1973.

[89] D.N. Christodoulides and R.I. Joseph. *Opt. Lett.*, 13:794, 1988.

[90] W.P. Su, J.R. Schieffer, and A.J. Heeger. *Phys. Rev. Lett.*, 42:1968, 1979.

[91] A.J. Sievers and S. Takeno. *Phys. Rev. Lett.*, 61:970, 1988.

[92] A. Trombettoni and A. Smerzi. *Phys. Rev. Lett.*, 86:970, 2001.

[93] H.S. Eisenberg, Y. Silberberg, R. Morandotti, A.R. Boyd, and J.S. Aitchison. *Phys. Rev. Lett.*, 81:3383, 1998.

[94] R. Morandotti, U. Peschel, J.S. Aitchison, H.S. Eisenberg, and Y. Silberberg. *Phys. Rev. Lett.*, 83:2726, 1999.

[95] B.A. Malomed and P.G. Kevrekidis. *Phys. Rev. E*, 64:026601, 2001.

[96] J.W. Fleischer, M. Segev, N.K. Efremidis, and D.N. Christodoulides. *Nature*, 422:147, 2003.

[97] K.E. Strecker, G.B. Partridge, A.G. Truscott, and R.G. Hulet. *Nature*, 417:150, 2002.

[98] Ferrari G Bourdel T Cubizolles J Carr L D Castin Y Khaykovich L, Schreck F and Salomon C. *Science*, 296:1290, 2002.

[99] I. Carusotto, D. Embriaco, and G.C. La Rocca. *Phys. Rev. A*, 65:053611, 2002.

[100] P.J.Y. Louis, E.A. Ostrovskaya, C.M. Savage, and Yu.S. Kivshar. *Phys. Rev. A*, 67:013602, 2003.

[101] V. Ahufinger, A. Sanpera, P. Pedri, L. Santos, and M. Lewenstein. cond-mat/0310042, 2003.

[102] B.P. Anderson and M.A. Kasevich. *Science*, 282:1686, 1998.

[103] S. Burger, Cataliotti, C. Fort, F. Minardi, M. Inguscio, M.L. Chiofalo, and M.P. Tosi. *Phys. Rev. Lett.*, 86:4447, 2001.

[104] O. Morsch, J.H. Müller, M. Cristiani, D. Ciampini, and E. Arimondo. *Phys. Rev. Lett.*, 87:140402, 2001.

[105] R.G. Scott, A.M. Martin, T.M. Fromhold, S. Bujkiewicz, F.W. Sheard, and M. Leadbeater. *Phys. Rev. Lett.*, 90:110404, 2003.

[106] M. Greiner, I. Bloch, O. Mandel T.W. Hänsch, and T. Esslinger. *Phys. Rev. Lett.*, 87:160405, 2001.

[107] M. Greiner, O. Mandel, T. Esslinger T.W. Hänsch, and I. Bloch. *Phys. Rev. Lett.*, 419:51, 2002.

[108] B. Eiermann, Th. Anker, M. Albiez M. Taglieber, P. Treutlein, K.P. Marzlin, and M.K. Oberthaler. cond-mat/0402178, 2004.

[109] B.B. Baizakov, V.V. Konotop, and M. Salerno. *J. Phys. B: At. Mol. Opt. Phys.*, 35:5105, 2002.

[110] E.A. Ostrovskaya and Yu.S. Kivshar. *Phys. Rev. Lett.*, 2003:160407, 2003.

[111] B.B. Baizakov, B.A. Malomed, and M. Salerno. *Europhys. Lett.*, 63:642, 2003.

[112] M.J. Steel and W. Zhang. cond-mat/9810284, 1998.

[113] H. Pu, L.O. Baksmaty, W. Zhang, N.P. Bigelow, and P. Meystre. *Phys. Rev. A*, 67:043605, 2003.

[114] J.H. Denschlag, J.H. Simsarian, H. Häffner, C. McKenzie, A. Browaeys D. Cho, K. Helmerson, S.L. Rolson, and W.D. Phillips. *J. Phys. B: At. Mol. Opt. Phys.*, 35:309, 2002.

[115] B. Eiermann, P. Treutlein, Th. Anker, M. Albiez, M. Taglieber an K.-P. Marzlin, and M.K. Oberthaler. *Phys. Rev. Lett.*, 91:060402, 2003.

[116] A. Soffer and M.I. Weinstein. nlin.PS/0308020, 2003.

[117] M. Desaix M, D. Anderson, and M. Lisak. *J. Opt. Soc. Am. B*, 8:2082, 1991.

[118] B.A. Malomed. *Progress in Optics*, 43:71, 2002.

[119] S. Flach, K. Kladko, and R.S. MacKay. *Phys. Rev. Lett.*, 78:1207, 1997.

[120] G. Kalosakas, K.O. Rasmussen, and A.R. Bishop. *Phys. Rev. Lett.*, 89:030402, 2002.

[121] B.B. Baizakov and M. Salerno. *Phys. Rev. A*, 69:013602, 2004.

[122] L.D. Carr and Y. Castin. *Phys. Rev. A*, 66:363602, 2002.

[123] F.Kh. Abdullaev, J.G. Caputo, R.A. Kraenkel, and B.A. Malomed. *Phys. Rev. A*, 67:013605, 2003.

[124] V.M. Perez-Garcia, V.V. Konotop, and J.J. Garcia-Ripoll. *Phys. Rev. E*, 62:4300, 2000.

[125] T. Tsurumi and M. Wadati. *J. Phys. Soc. Jpn.*, 70:1512, 2001.

[126] L. Salasnich, A. Parola, and L. Reatto. *Phys. Rev. A*, 65:043614, 2002.

[127] F.Kh. Abdullaev, B.B. Baizakov, S.A. Darmanyan, V.V. Konotop, and M. Salerno M. *Phys. Rev. A*, 64:043606, 2001.

[128] W.H. Press, S.A. Teukolsky, W.T. Vetterling, and B.P. Flannery. *Numerical Receipes in C*. Cambridge University Press, Cambridge, 2nd edition, 1992.

[129] B. Wu and Q. Niu. *New J. Phys.*, 5:104, 2003.

[130] G. Blanch. *Handbook of Mathematical Functions*. U.S. Govt. Print. Off., Washington, 1964.

[131] J.J. García-Ripoll and V.M. Pérez-García. *SIAM J. Sci. Comput.*, 23:1316, 2001.

[132] M.R. Andrews, M.O. Mewes, N.J. van Druten, D.S. Durfee D.M. Kurn, and W. Ketterle. *Science*, 273:84, 1996.

[133] S. A. Wolf, D. D. Awschalom, R. A. Buhrman, J. M. Daughton, S. von Molnár, M. L. Roukes, A. Y. Chtchelkanova, , and D. M. Treger. *Science*, 294:1488, 2001.

[134] N. Nagaosa S. Murakami and S.-C. Zhang. *Science*, 301:1348, 2003.

[135] J. Sinova, D. Culcer, Q. Niu, N. A. Sinitsyn, T. Jungwirth, and A. H. MacDonald. cond-mat/0307663.

[136] D. Culcer, Jairo Sinova, N. A. Sinitsyn, T. Jungwirthand A. H. MacDonald, and Q. Niu. cond-mat/0309475.

[137] Y. K. Kato, R. C. Myers, A. C. Gossard, and D. D. Awschalom. *Science*, 306:1910, 2004.

[138] J. Sinova J. Wunderlich, B. Kaestner and T. Jungwirth. *Phys. Rev. Lett.*, 94:047204, 2005.

[139] Yu. A. Bychkov and E. I. Rashba. *J. Phys. C*, 17:6039, 1984.

[140] D. L. Haycock, P. M. Alsing, I. H. Deutsch, J. Grondalski, and P. S. Jessen. *Phys. Rev. Lett.*, 85:3365, 2000.

[141] O. Mandel, M. Greiner, A. Widera, T. Rom, T. W. Hänsch, and I. Bloch. *Phys. Rev. Lett.*, 91:010407, 2003.

[142] E. Demler L.-M. Duan and M. D. Lukin. *Phys. Rev. Lett.*, 91:090402, 2003.

[143] I. Carusotto and E. J. Mueller. cond-mat/0310687.

[144] W. Harper and B. S. Mathur. *Phys. Rev.*, 163:163, 1967.

[145] J. Dalibard and C. Cohen-Tannoudji. *J. Opt. Soc. Am. B*, 6:2023, 1989.

[146] M. Zielonkowski, I. Manek, U. Moslener, P. Rosenbusch, and R. Grimm. *Europhys. Lett.*, 44:700, 1998.

[147] M. Zielonkowski, J. Steiger, U. Schünemann, M. DeKieviet, and R. Grimm. *Phys. Rev. A*, 58:3993, 1998.

[148] G. Grynberg, B. Lounis, P. Verkerk, J. Y. Courtois, and C. Salomon. *Phys. Rev. Lett.*, 70:2249, 1993.

[149] I. H. Deutsch and P. S. Jessen. *Phys. Rev. A*, 57:1972, 1998.

[150] N. Friedman, A. Kaplan, and N. Davidson. *Adv. At. Mol. Opt. Phys.*, 48:99, 2002.

[151] M. Gehm. PhD thesis, Duke University, 2003.

Vita

Artem Dudarev was born on August 7, 1978 to Mikhail Dudarev and Valentina Dudareva in Donetsk, Ukraine. After graduating from High School №35 in Donetsk, Artem earned his Bachelor's degree in Applied Physics and Mathematics at Moscow Institute of Physics and Technology in 1999. In the fall of 1999, he entered the Graduate School of The University of Texas at Austin.

Permanent address: ul. M. Kozyrya d. 11 kv. 77
Donetsk, 83064
Ukraine

This dissertation was typeset with LaTeX[†] by the author.

[†]LaTeX is a document preparation system developed by Leslie Lamport as a special version of Donald Knuth's TeX Program.